The Pennsylvania State University

The Graduate School

PRELIMINARY DESIGN OF A HOT HYDROGEN TEST LOOP FOR NUCLEAR THERMAL PROPULSION APPLICATIONS

A Thesis in

Nuclear Engineering

by

William T. Searight

Submitted in Partial Fulfillment

of the Requirements

for the Degree of

Master of Science

August 2020

The thesis of William T. Searight was reviewed and approved by the following:

Leigh Winfrey
Associate Professor of Nuclear Engineering
Thesis Adviser

Elia Merzari
Associate Professor of Nuclear Engineering

Jean Paul Allain
Professor of Nuclear Engineering
Department Head of Nuclear Engineering

ABSTRACT

Nuclear Thermal Rockets (NTRs) are one of the leading propulsion system candidates in deep space exploration due to their high thrust to weight ratio and specific impulse, reducing both the cost of deep space missions and the exposure of payloads to space radiation. To aid in NTR system design being done by Ultra Safe Nuclear Corporation, this work presents a preliminary design of a hot hydrogen test loop facility that can subject NTR tie tubes to NTR hydrogen flow conditions. Tie tubes are channel elements through which hot hydrogen coolant/propellant flows in the reactor core; these hydrogen facing components will be subject to plasma embrittlement as hydrogen gas begins exhibiting bulk plasma behavior. It is critical to characterize these effects for NTR longevity in deep space missions, and this test loop design will provide initial data at 1200 °C, moving to 2700 °C in a later design.

Preliminary design work was conducted using ANSYS 2020 R1 Student Edition, using both Steady-State Thermal and Fluent models to obtain temperature and velocity distributions in the loop pipes, hydrogen, and tie tubes. The Fluent model was simplified to a linear pipe flow design to improve test section flow results. The heating section was assumed to have a heat load evenly distributed over the pipe surface. In practice, heating will need to provide an equivalent power over the smaller contact area. The selection of a FeCrAl alloy as the test loop pipe material was validated for loop operating conditions, and the loop provided sufficient heating to the hydrogen and tie tube for a variety of pipe cross-sectional areas and thicknesses. The flow was found to be largely laminar for the operating mass flow rate and pressure. The loop produced suitable operating temperatures even under high vacuum conditions, although further study of the cooling system is needed to verify forced convection can be obtained.

TABLE OF CONTENTS

LIST OF FIGURES

LIST OF TABLES

LIST OF ACRONYMS/ABBREVIATIONS

LEO – Low Earth Orbit

T/W – Thrust to Weight ratio

RTG – Radioisotope Thermoelectric Generator

NTR – Nuclear Thermal Rocket

DRA – Design Reference Architecture

BEARS – $\vec{B} \times \vec{E}$ Applied Research & Science laboratory

USNC – Ultra Safe Nuclear Corporation

SST – Steady-State Thermal

CFD – Computational Fluid Dynamics

LANL – Los Alamos National Laboratory

NERVA – Nuclear Engine for Rocket Vehicle Application

SPNO – Space Nuclear Propulsion Office

AEC – Atomic Energy Commission

DOE – Department of Energy

NRC – Nuclear Regulatory Commission

SNRE – Small Nuclear Rocket Engine

ORNL – Oak Ridge National Laboratory

HEU – Highly Enriched Uranium

LEU – Low Enriched Uranium

NTREES – Nuclear Thermal Rocket Element Environmental Simulator

LIST OF ACRONYMS/ABBREVIATIONS (CONTINUED)

CERMET – Ceramic-Metallic alloy

MSFC – Marshall Space Flight Center

CFEET – Compact Fuel Element Environmental Test

RF – Radio Frequency

SiC/SiC – Silicon Carbide-Silicon Carbide matrix composite alloy

TZM – Titanium Zirconium Molybdenum alloy

FeCrAl – Iron Chromium Aluminum alloy

MFR – Mass Flow Rate

ID – Inner Diameter

OD – Outer Diameter

NIST – National Institute of Standards & Technology

ACKNOWLEDGEMENTS

Just like any academic work's author, I am indebted to the many wonderful people surrounding me and helping me along the way towards this and other milestones. First off, I want to sincerely thank my parents for raising me in an environment steeped in science and curiosity and providing me unwavering love and support to develop my passions. Secondly, I want to thank Dr. Gregory Maxwell, an invaluable friend and mentor who helped me discover nuclear engineering through his insight and unfailing humor. Next, I want to thank my advisor, Dr. Leigh Winfrey, who has graciously supported my journey from student novice to research novice. I want to thank the friendly and brilliant people at Ultra Safe, particularly Mr. Aaron Selby and Dr. Michael Eades, for their guidance in NTRs and modeling. I also want to extend my gratitude to Dr. Elia Merzari, who through video calls and email patiently helped explain the nuances of fluid dynamics and thermal modeling and guided me towards success.

This thesis has also been made possible by the amazing and passionate people in the recently formed Ken & Mary Alice Lindquist Department of Nuclear Engineering, who continue to impress and inspire me to further and give back to the nuclear engineering and greater scientific community. While by no means a comprehensive list, I want to acknowledge Alex Somers, Victoria Hagopian, Matt Flanders, Dr. Marc Wonders, Matt Durbin, Beth Huber, Missy Price and Dr. Jean Paul Allain, our caring and steadfast department head, to name just a few. Finally, I want to sincerely thank Corrine, who patiently and thoughtfully gave me support and understanding while I sequestered myself away at my desk, taxing my processors in order to bring about the work presented here.

Chapter 1: INTRODUCTION

Space is vast and inhospitable, and exploring beyond our home planet means travelling great distances and mitigating exposure to space radiation. The term deep space exploration encompasses all manned and unmanned missions which venture beyond Low Earth Orbit (LEO), where the International Space Station orbits. One of the greatest limiting factors in exploration missions' feasibility is distance to locations of interest. A spacecraft's range is determined by its propulsion system; chemical rocket propulsion has dominated the research space as the conventional technology of choice throughout the history of space travel. Two more important constraints to space exploration missions are a spacecraft's weight and cost to manufacture. Since chemical rockets require substantial amounts of fuel relative to the spacecraft's payload, recent missions have mostly featured unmanned satellites that are lighter and cost less to launch into space. In order to improve the feasibility of missions to Mars and beyond, propulsion systems with greater thrust to weight ratios (T/W's) are needed to simultaneously reduce mission travel times and maximize the amount of cargo and crew on said missions.

Recent unmanned satellites have primarily relied on both solar arrays and Radioisotope Thermoelectric Generators (RTGs) for power, and both supply amounts of power too small for larger, manned deep space missions. An alternative is ion-based propulsion, which is very efficient in space but needs a while to build up substantial amounts of thrust to accelerate the spacecraft, which extends total mission duration and prolongs the exposure of instruments and crew to the space radiation environment. With these current technologies lacking in a combination of desired features, nuclear-based propulsion is especially attractive for deep space exploration.

Specifically, Nuclear Thermal Rockets (NTRs) are seen as the leading propulsion system candidate for deep space exploration due to their high T/W compared to chemical rockets and their high energy density, allowing them to be used for longer missions. NASA has indicated that NTRs are the chosen propulsion system in their Design Reference Architecture (DRA) 5.0, a detailed study and framework for human exploration of Mars [1]. NTRs like the one proposed by S. Nam et al. [2] are also promising because they could be operated bimodally, providing both thrust to propel the spacecraft and generate electrical power for the payload. With NASA recently providing funding to develop an NTR in earnest [3], the NTR must pass several important development hurdles to make it to the launchpad.

The NTR is currently being developed only for deep space propulsion because the scaling up of a nuclear-based propulsion system into a launch system would face more barriers to development than existing systems. Because of this, the most effective NTR must be as lightweight and compact as possible, while still supplying useful propulsion for an entire mission. Because of this small size, the main challenge of the reactor is neutron loss. Neutrons born from fission in the fuel have a lot of energy and can travel fast and far before colliding with anything. NTR designs make use of Beryllium reflectors in order to reflect as many neutrons back inside as possible. The heat transfer from the fuel to the propellant (which also serves as coolant, see Figure 1.1) is most efficient when the propellant atoms are smaller, making hydrogen the best candidate. Also, the NTR produces more thrust the higher the exit temperature of the hydrogen is. With current designs aiming for exit temperatures around 3000 K (Kelvin), the materials in the reactor must be very heat-resistant to withstand such operating conditions. Ceramics comprise most of the viable candidates for NTRs since ceramics generally have high melting points and hardness.

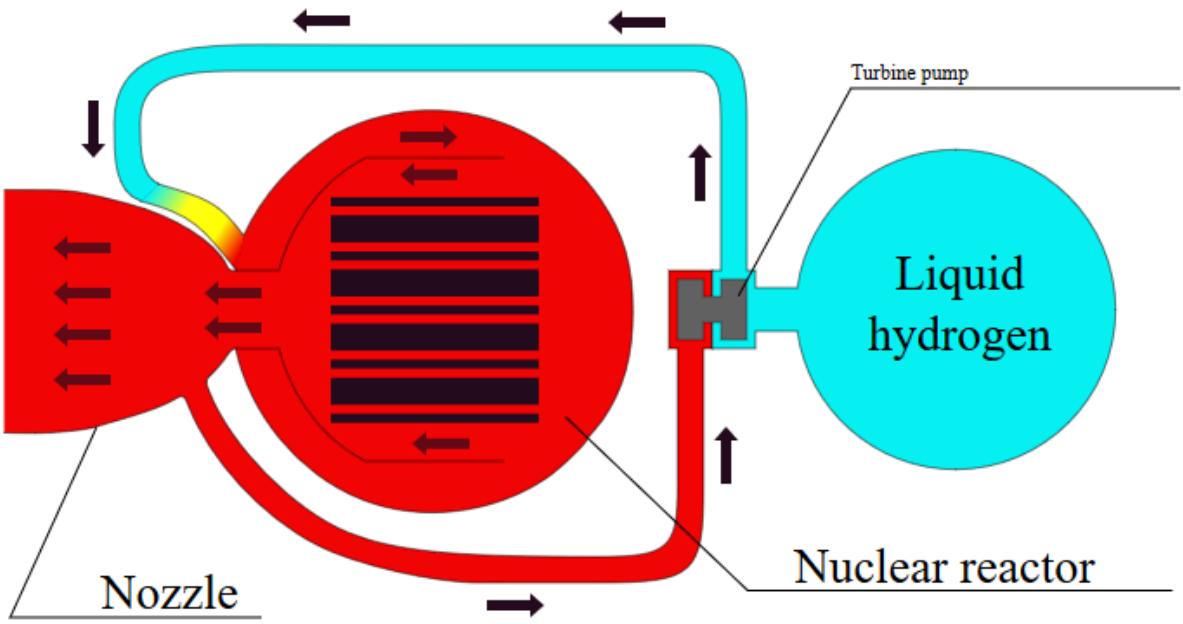

Figure 1.1: Representative diagram of a Nuclear Thermal Rocket [open source]

The operating temperature of the NTR is so high that the hydrogen propellant/coolant gains enough energy to become a plasma. A gas becomes a plasma when electrons gain enough energy to roam free of the atoms they orbited, forming a conductive fluid of ions and electrons. A central concern for hydrogen plasma-material interaction is hydrogen embrittlement, where hydrogen diffuses into the ceramic and bonds to form weaker compounds, to the detriment of the overall ceramic part and the lifetime of the rocket engine. While the mechanical properties of the reactor components are reasonably well known, the effects of hydrogen plasma interacting with these ceramics is not as well studied in aerospace applications as it is in the field of nuclear fusion. The $\vec{B} \times \vec{E}$ Applied Research & Science (BEARS) Laboratory at the Pennsylvania State University has expertise in both fusion and hydrogen plasma interactions, and will be able to utilize these strengths for NTR materials testing and research.

This project aims to study the effects of hydrogen plasma on ceramic NTR parts, specifically the tie tube, in collaboration with Ultra Safe Nuclear Corporation (USNC) and their contract with NASA to develop a Nuclear Thermal Rocket for manned missions to Mars. A tie tube is an annular part consisting of cylindrical ceramic neutron moderator pieces, surrounded by an outer shell, to serve as channels for hydrogen to flow through the reactor. A geometrical model of USNC's current tie tube design is shown in Figure 1.2. The tie tube and other parts must be tested in a suitable environment, and this thesis focuses on the preliminary design of a hot hydrogen test loop facility for circulating hydrogen plasma across a test sample. For this phase of development, the test loop needs to supply hydrogen at 1200 °C (1473 K) to the test section of the loop. The models developed in this thesis will work to validate the proposed loop design and demonstrate safe operation and accurate reproduction of hydrogen conditions the NTR tie tubes would experience.

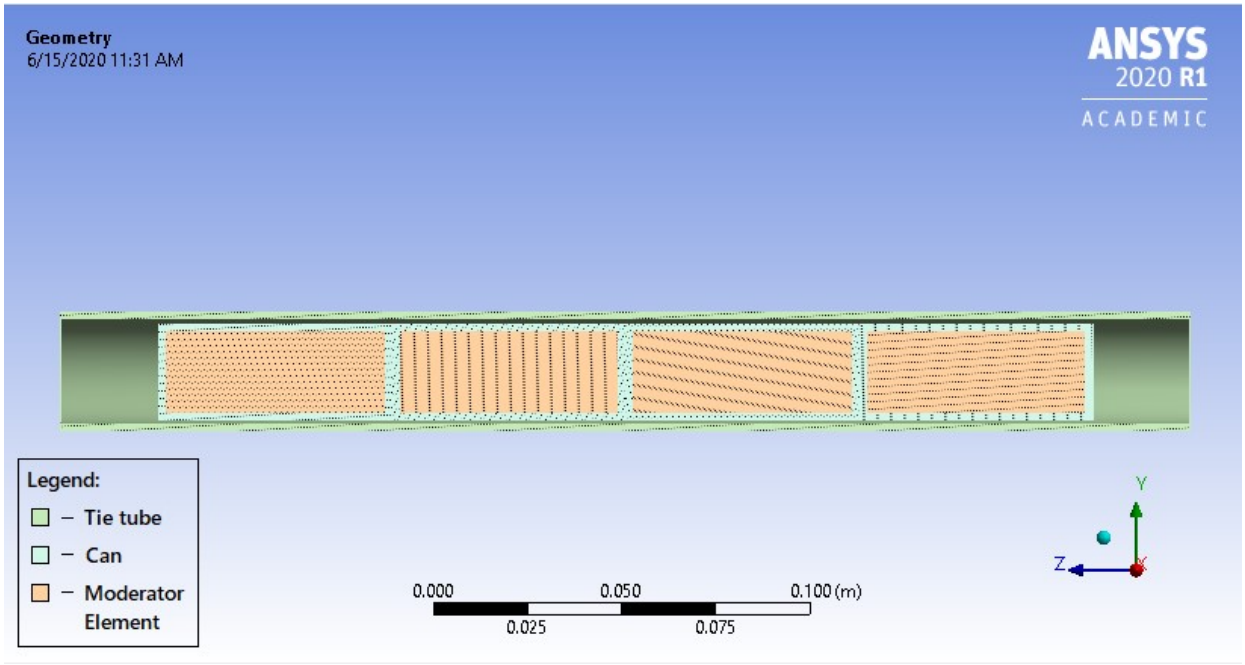

Figure 1.2: Cutaway view of USNC tie tube model

The focus of the model development in this thesis is on thermal modeling of hydrogen interacting with the loop's pipes and the tie tube. Steady-State Thermal (SST) and Computational Fluid Dynamics (CFD) simulations were conducted in ANSYS 2020 R1, making use of ANSYS's Fluent module for CFD analysis. The model development will be covered in Chapter 3, and the model will be validated against test problems simulating pipe flow in Chapter 4. Chapter 5 will summarize the results of the test loop and tie tube modelling, and the next steps in advancing the practical development of NTRs for deep space exploration.

Chapter 2: DESIGN OF NUCLEAR THERMAL ROCKET SYSTEMS

2.1 Fundamentals of rocket propulsion

Propulsion simply means the act of moving objects, propelling them in a certain direction. All current forms of rocket propulsion rely on the conservation of momentum: the rocket ejects propellant mass in one direction, pushing the slightly lighter rocket vehicle in the opposite direction. The two main ways propulsion systems vary is in the energy source and the choice of propellant. In chemical rocket propulsion, the energy comes from the propellant itself as it undergoes highly energetic chemical reactions in the engine and is directed out the rocket′s nozzle at high speeds. Chemical rocket propellant can be in either liquid or solid form, with liquid chemical rocket engines typically having either monopropellant or bipropellant. A bipropellant engine stores two liquids, a fuel and an oxidizer, and explosively combines them, whereas a monopropellant releases its energy when exposed to a catalyst. Chemical rockets can also be operated with ducts to allow air in and improve combustion, but this advantage is only for rockets within Earth′s atmosphere. For more information on rocket propulsion, Sutton & Biblarz is a useful resource [4].

Most other rocket propulsion varieties besides chemical propulsion have a separate energy source which transfers heat to the propellant. The most prevalent forms of propulsion systems are depicted in Figure 2.1 and compared in terms of two important aerospace figures of merit to be discussed in detail later on in this section.

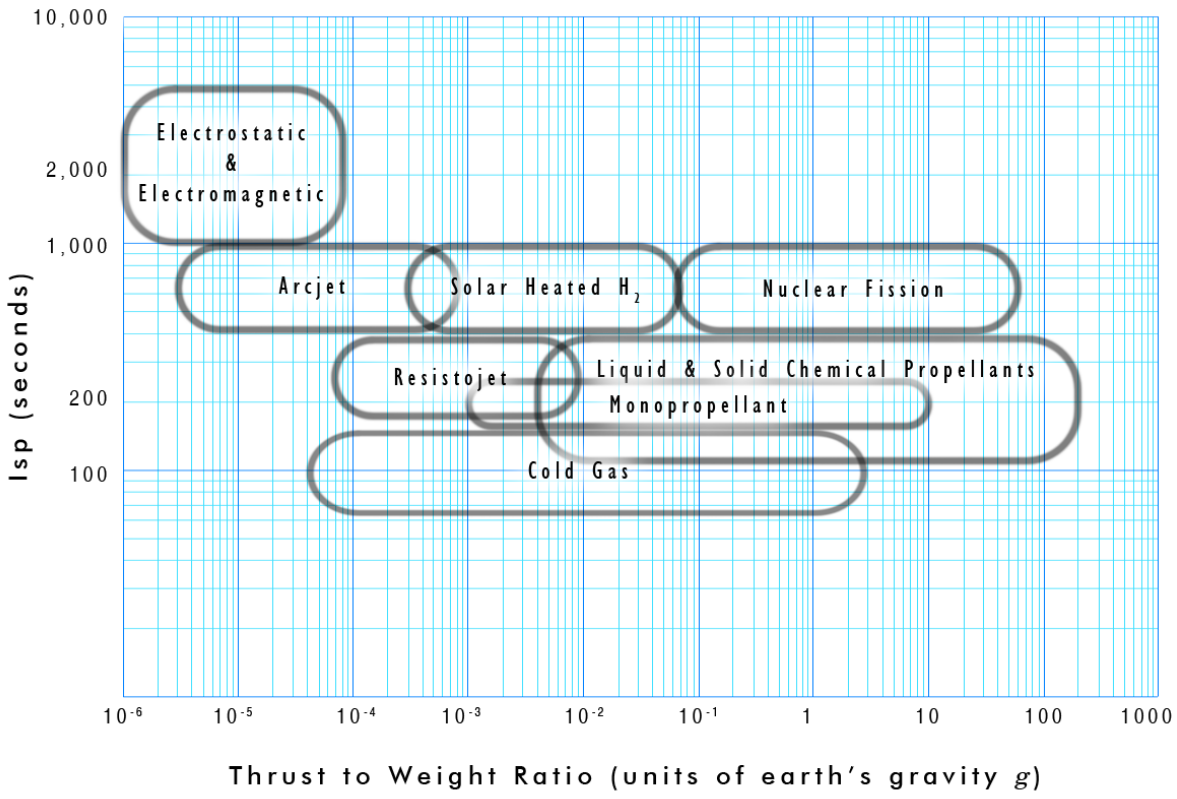

Figure 2.1: Performance of different propulsion systems [open source]

These remaining propulsion systems belong to two main families: electric and thermal propulsion. Of the electrical propulsion systems, the arcjet is most similar to chemical propulsion, creating a discharge (arc) through a monopropellant in order to give the propellant more energy for propulsion. A resistojet imparts energy to the propellant thermally, through heating up a resistor with large amounts of electricity. In electrostatic and electromagnetic propulsion systems, electric and magnetic fields are used respectively to ionize neutral (typically noble) gases and accelerate the resulting electrons and ions out the nozzle. Although these electrical propulsion systems typically use some form of energy other than nuclear power (i.e. batteries, solar panels, etc.), the two are not mutually exclusive. While not the focus of this thesis, nuclear electric propulsion is a system of great promise being studied for future deep space missions along with nuclear thermal propulsion [5] [6] [7].

Finally, nuclear thermal propulsion works in a similar fashion to the resistojet, heating up the propellant by channeling it through the reactor core, where heat from fission is generated in fuel atoms like Uranium and Plutonium. Although there is a third type of nuclear propulsion, called nuclear pulsed propulsion, it will not be discussed here due to the radiological and safety concerns of detonating nuclear warheads for propulsion.

At this point it is important to clarify two important parameters used to quantify rocket performance. First is the **specific impulse** of the engine, with the slightly nebulous units of seconds. Beginning from Newton's 2nd Law of Motion, we have:

$$F = ma = m\dot{v} \tag{2.1}$$

For convenience, Equation 2.1 uses dot notation for derivatives with respect to time. Now, since a rocket's mass is changing due to expelling propellant and the exhaust velocity at the nozzle's exit is approximately constant with respect to time:

$$F = \dot{m}v_{exhaust} \tag{2.2}$$

In deep space a rocket is typically assumed to be far away from gravitational centers, so the exhaust velocity can be re-written in terms of a gravitational acceleration constant:

$$F[N] = \dot{m}\left[\frac{kg}{s}\right]\left(g_0\left[\frac{m}{s^2}\right]I_{sp}[s]\right) \tag{2.3}$$

Square brackets are used to note the units of each term. In Equation 2.3, we can see the appearance of specific impulse, which has units on seconds in order to give the overall exhaust velocity term the correct units of distance per unit time. The meaning of specific impulse becomes clearer when Equation 2.3 is re-arranged:

$$I_{sp}[s] = \frac{F\left[N = \frac{kg * m}{s^2}\right]}{\dot{m}\left[\frac{kg}{s}\right] g_0 \left[\frac{m}{s^2}\right]} \tag{2.4}$$

As Equation 2.4 more clearly shows, the specific impulse is a ratio of a rocket's thrust force, in Newtons, over the rate of propellant consumption. The better rocket engine will be able to maximize thrust and minimize propellant consumption.

The **Thrust to Weight ratio** (T/W) is somewhat more self-explanatory. It is the ratio of the engine's thrust to the total weight of the engine, structure and propellant and all. It is an indication of how much acceleration the engine can impart on the rocket and is usually expressed in multiples of the gravitational acceleration at Earth's surface. Referencing Figure 2.1 again, this makes physical sense in that an electrostatic, or ion, thruster would output very small thrusts compared to the total engine weight since the mass of the ionized propellant is not very large. Therefore, the ion thruster would accelerate the engine in space much more slowly than a chemical rocket or even a cold gas jet with a larger molecular weight propellant.

With specific impulse and T/W in mind, it becomes clear through Figure 2.1 than nuclear-powered propulsion systems have the best of both worlds: high efficiency in thrust production, and large amounts of possible acceleration for the space vehicle. So why haven't nuclear propulsion systems become more prevalent and widespread? As is usually the case, the truth defies a single, simple explanation, so in the next section the history of Nuclear Thermal Propulsion and its designs will be presented.

2.2 A brief history of Nuclear Thermal Propulsion

The development of nuclear rocket engines for space travel has a historic legacy, one that pre-dates the establishment of NASA by several years. Development of NTRs in the United States began in 1955 at Los Alamos National Laboratory (LANL) in New Mexico, then the Los Alamos Scientific Laboratory, under the name Project Rover [8]. During these first few years, the conceptual design of the reactor core was undertaken, resulting in the Kiwi series of reactors, named for the flightless bird since they were intended only for ground tests. Upon NASA's establishment in 1958, it was given control of the non-nuclear aspects of Project Rover and rolled the program into its Nuclear Engine for Rocket Vehicle Application (NERVA) program in 1961. The NERVA program was managed by the Space Nuclear Propulsion Office (SPNO), a joint venture between the Atomic Energy Commission (AEC) and NASA. The AEC was the pre-cursor to the U.S. Department of Energy (DOE), which focuses on research and development of nuclear technologies, and the Nuclear Regulatory Commission (NRC). NASA selected Aerojet and Westinghouse as the primary contractors for the NERVA program.

During the NERVA program, which lasted until being cancelled by President Nixon in 1972, LANL developed several reactor iterations after Kiwi: the Phoebus program, building off of Kiwi to design engines for interplanetary travel, the Peewee program for developing smaller, compact designs and the Nuclear Furnace reactor, for testing of advanced high-temperature materials [9]. There were a total of 23 reactor tests, and the maximum test parameters achieved are summarized in Table 2.1. Figure 2.2 shows a cutaway and photo of a NERVA rocket, whose development was primarily based on the Kiwi B4 series reactors.

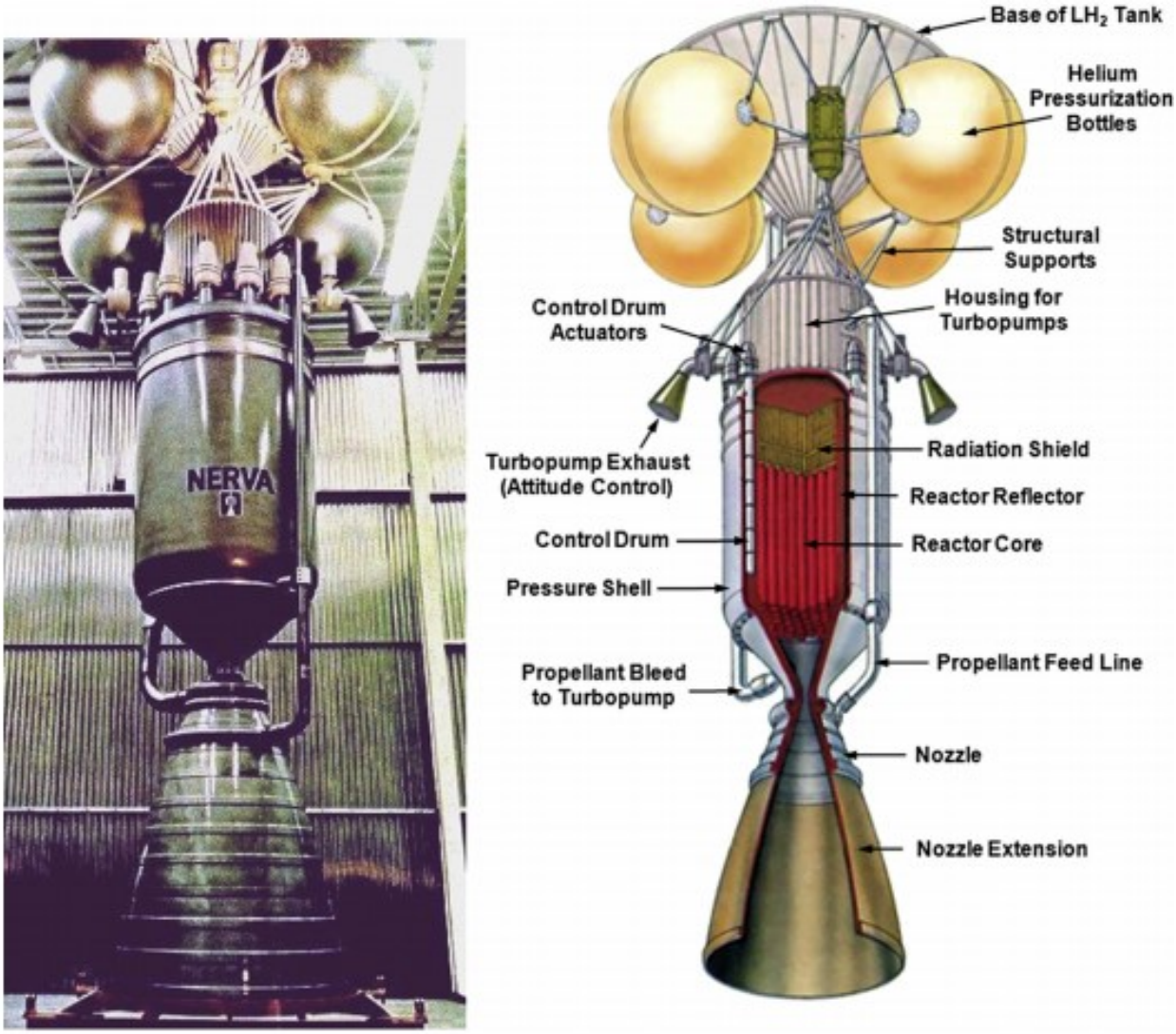

Figure 2.2: Photo and cutaway diagram of a NERVA engine [9]

NERVA test parameter	Maximum value achieved
Reactor Power (MW)	4500
Reactor Temperature (K)	2750
Thrust (lbf.)	250000 (1.1 MN)
Specific Impulse (s)	850
Burn Time (min.)	90

Table 2.1: Maximum test parameters achieved in NERVA program [8]

It is worth noting, at least briefly, that all NTRs developed under NERVA were based on a solid reactor core concept. Because the melting temperatures of the engine materials have a limiting effect on the specific impulse of the rocket, there are concepts for both liquid and gaseous cores which could mitigate this constraint, although all of these concepts are exceedingly complex and difficult and thus will not be discussed further.

The NERVA reactors were all designed with hexagonal prism-shaped fuel elements, made of uranium dioxide and later a uranium/graphite matrix, with holes drilled through them to allow hydrogen to flow through, both cooling the reactor and heating the propellant. Because the reactor is so small that fast neutrons can easily escape, beryllium reflectors are needed to conserve neutrons and reduce loss. In order to control the reactor power, rotatable control drums are embedded in the reflector, with a portion of the drum coated in a neutron absorbing material (boron carbide). Owing to the high temperatures of the hydrogen and core elements during operation, all of the reactor elements were designed to be ceramic, and the overall engine incorporated a hot-bleed engine cycle. In this cycle, a small amount of hydrogen is bled off after leaving the core, mixed with colder hydrogen from the pressure vessel and used to turn a turbine that drives a pump. This same pump is responsible for pressurizing the main hydrogen flowing in from the cryogenic storage tanks into the pressure vessel [10]. The hot-bleed cycle has the advantage over other cooling cycles of having a small penalty to specific impulse [11], which led to its adoption. In the NERVA designs, the cryogenic hydrogen is initially fed in the jacket surrounding the nozzle to cool it before being fed back to enter the reactor, but in later designs this has been changed. For example, in the design by S. Nam et al. [12] as seen in Figure 2.3, a bypass stream of hydrogen is pumped to the nozzle and reflector while the rest is pumped over the structure and moderator, then recombine and flow through the fuel and out.

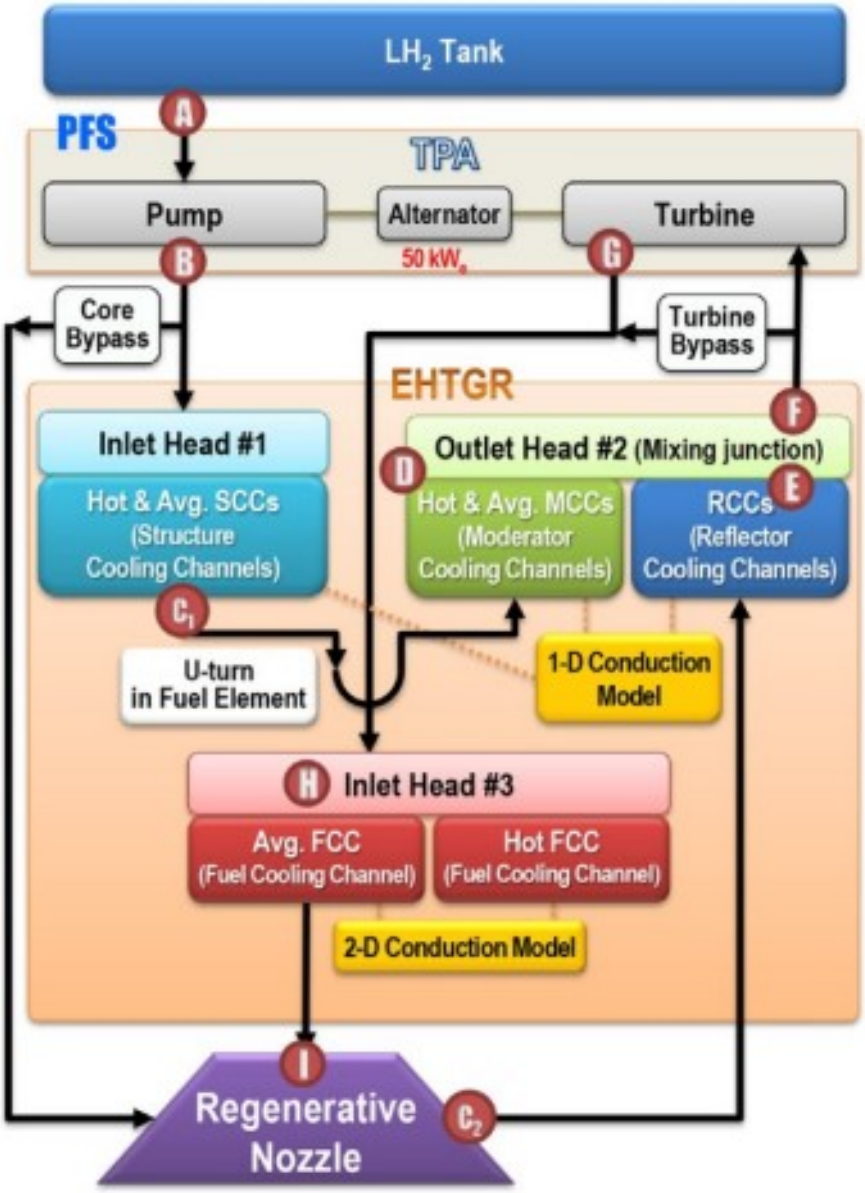

Figure 2.3: Block diagram of NTR hydrogen flow path from S. Nam et al. [12]

Despite the progress made during the NERVA program, including the consideration of a Small Nuclear Rocket Engine (SNRE) for a manned mission third stage, these engines never flew. This is despite the fact that the specific impulse achieved was almost three times larger than the Saturn V rocket and twice that of the upcoming Space Shuttle Liquid hydrogen/oxygen engines [13]. However, a changing landscape in U.S. political objectives and funding conditions led to the program's cancellation, along with the curtailing of the Apollo program in the following years.

While larger manned missions decreased in number, robotic missions became much more prevalent, with many using RTGs for power to great effect where solar and battery resources were insufficient. Their development in the SNAP program paralleled the NERVA program, its design going through several iterations before settling on using Plutonium-238 as its power source [14]. Pu-238 is overwhelmingly an alpha particle emitter, which makes it easier to shield against, and modern iterations have produced upwards of 3 Watts electric per kilogram of fuel. However, the efficiencies of thermal to electrical output are at best in the single digits of percent, and the U.S. store of Pu-238 has rapidly dwindled due to its use on missions, natural radioactive decay and the shutdown of Pu-238 production facilities as a nuclear weapons non-proliferation strategy. Oak Ridge National Laboratory (ORNL) has recently been restarting U.S. production capability, but it has been time-consuming and tricky [15].

In the years after NERVA, there was some limited interest in nuclear propulsion beyond RTGs, during the late 1980s, which was inconclusive [13] [16]. There was work done by the U.S.S.R. from 1965 into the 1980s into a nuclear thermal rocket called the RD-0410, with comparable performance parameters to the NERVA engine, but this engine was also never flown [17]. However, there are current design iterations being worked on in both Russia and the U.S., coming from renewed interest in the advantages of nuclear-based propulsion over chemical rocket propulsion for deep space missions.

2.3 Beyond NERVA: Issues facing current designs

While the benefits of NTRs have already been discussed in relation to other forms of deep space propulsion, there are some important design challenges for NTRs to become feasible for missions. The first concern with NTRs is the use of Highly Enriched Uranium (HEU) versus Low Enriched Uranium (LEU). HEU has been used in all historical NTR designs since it takes less fuel mass to create a critical system, which helps in mass minimization for deep space missions. However, HEU is a significant nuclear weapons proliferation concern as it could be more easily stolen and made into a weapon than LEU. Recently NASA has made considerable progress with the Kilopower program, an HEU propulsion system that has completed the first ground test an NTR system has seen in decades [18]. Despite this, there have been widespread design efforts in the NTR community to implement LEU core designs and mitigate proliferation concerns. It has been found that a critical LEU system can be developed with only a ~20% mass increase from HEU [19], and with comparable specific impulse and thrust capabilities [20]. The second concern is public acceptance of the technology. While not a technical constraint, it is a hurdle towards approval of the designs for fabrication, testing and eventual flight. Fortunately, the Interagency Nuclear Safety Review Panel has conducted numerous studies on the safety of space nuclear technologies and have indicated that scenarios posing significant risk to the public are highly unlikely for both RTGs and space reactor systems [21].

A third concern is in material selection and design, which are critical in handling the immense heat of the reactor and channeling the hydrogen properly to keep components cooled and useful. Since this last concern is one which can be acted on most directly by the present research team, materials testing will be the focus of this research and this project. An issue in

materials selection that relates to the first concern is with moderating materials, which are not needed in HEU systems but required in LEU systems in order to prevent neutron absorption in Uranium-238 and reduce neutron energy to increase the chance of fission in Uranium-235. Two of the main candidates for NTR moderating materials, Lithium Hydride and Zirconium Hydride, have melting temperatures much lower than other ceramic materials, which requires effective cooling of the moderator [12]. Since moderator elements are planned to be housed in tie tubes, channel elements for hydrogen to flow through, testing of these tie tubes in a hot hydrogen environment will illuminate the heat transfer properties of these elements.

Experimental data derived from this project will serve as verification of the initial design and allow for the tie tubes to be improved upon for better heat transfer to the hydrogen. Additionally, the hydrogen becoming a plasma at high temperatures will introduce additional corrosive effects on the tie tube elements, the extent of which likely have not been covered in the initial design. In order to characterize these effects and redesign the engine to minimize their detriment, a hot hydrogen test loop facility will be built in the BEARS lab, on the basis of the simulations discussed in Chapter 3. These simulations are a preliminary characterization of the conditions expected for a tie tube subjected to hot hydrogen, entering the test section at ~1200 °C (1473 K). This requirement was agreed upon with USNC in order to obtain preliminary materials data for the current phase of the project, and then a higher temperature loop will be constructed to simulate the typical NTR operating conditions of ~3000 K.

2.4 Modern testing of NTR systems

The design of the BEARS NTR test facility should draw from and take into account recent NTR testing work conducted by NASA in the past decade, work that corresponds to the renewing interest in pursuing the benefits of NTR technology for deep space exploration. The 2009 Mars DRA 5.0 lays out intents for development of both NTR propulsion and surface fission power systems in pursuit of the Moon and Mars exploration [1], and both programs have seen research and development since. NTR testing work has progressed under the Nuclear Thermal Rocket Element Environmental Simulator (NTREES) program, testing non-nuclear NTR materials in a flowing hydrogen environment [22]. The program focuses on CERMET, or ceramic-metallic materials, which along with carbon-based composites are seen as the best candidates for NTR fuel elements. A diagram for NTREES is shown in Figure 2.4 below.

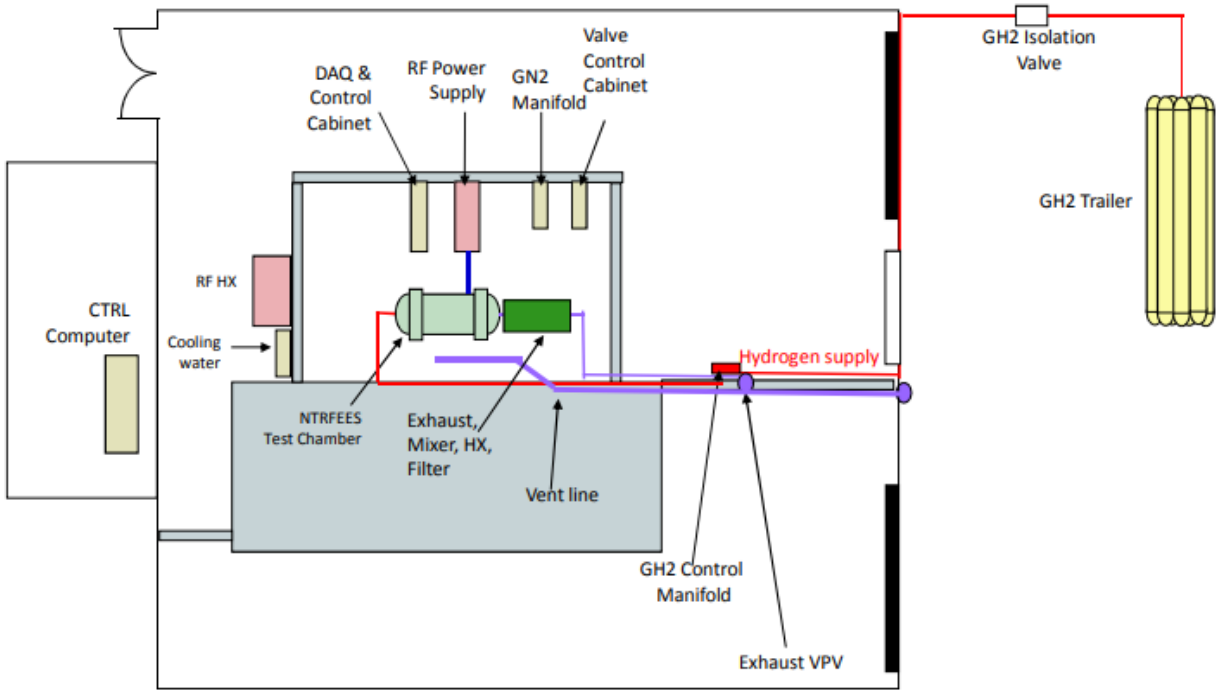

Figure 2.4: Layout of the Nuclear Thermal Rocket Element Environmental Simulator [23]

An accompanying testing program to NTREES, also conducted at NASA's Marshall Space Flight Center (MSFC), is the Compact Fuel Element Environmental Test (CFEET) facility. This experiment is a lower cost facility for exposing materials to temperatures of up to 2500 °C through Radio Frequency (RF) coil heating in a vacuum chamber. An illustration of the set-up is shown in Figure 2.5. The samples were originally loaded through the bottom, but this blind loading led to alignment issues and was modified to allow for top loading [25]. Both of these programs have yielded positive results on NTR materials, and have helped to continue building support within and outside of NASA for NTR development.

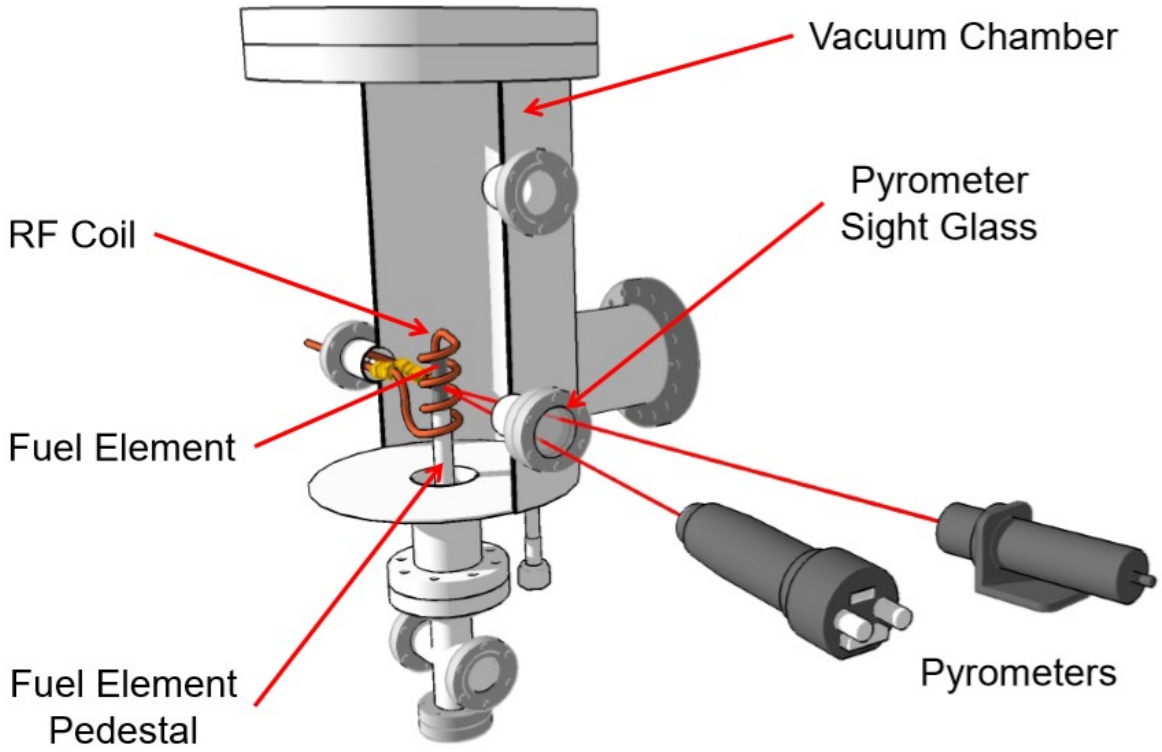

Figure 2.5: Setup of the Compact Fuel Element Environmental Testing (CFEET) chamber [24]

While Tungsten and related CERMET materials have seen extensive testing through these programs, composite alloys such as Silicon Carbide matrix composites (SiC/SiC) and Titanium Zirconium Molybdenum (TZM) have yet to be studied in a hydrogen environment in detail. These composites offer attractive corrosion resistant properties and may avoid some of the cracking structures that Tungsten develops upon exposure to high temperature hydrogen plasma [26]. These materials are both under consideration in the USNC tie tube design, and the BEARS hydrogen test loop will examine the behavior of these materials under prolonged hydrogen plasma exposure to characterize these effects. This testing is an important validation of the materials' properties and suitability for NTR use, which is crucial to the development of a working NTR for use in space exploration.

Chapter 3: SIMULATION DEVELOPMENT

3.1 Preliminary Design Constraints

Before jumping to the building phase of this experiment, the design of the BEARS hydrogen test loop needs to conform to appropriate safety standards for handling hydrogen plasma at high temperatures. Hydrogen and its handling procedures are fortunately well documented [27], and a few key safety details will be reiterated here. First and foremost is hydrogen's flammability, a big concern since it can ignite over a wide range of concentrations (4%-75% by volume in air) and with a low ignition energy (2×10^{-5} J). Since it is exceptionally light (~14 times lighter than air), it must be stored at high pressures (10,000 – 15,000 psi -> 69 – 103 MPa) to dispense practical amounts of mass, which increases the risk of ignition. Hydrogen also has well-known tendencies to attack (embrittle) materials used in storage containers and piping, and therefore tends to leak through containment systems. This tendency is enhanced by its high buoyancy (owing to its light weight), which allows it to rise quickly and escape.

To mitigate these safety concerns, the BEARS hydrogen test loop will be surrounded by a high vacuum Lexan™ box full of nitrogen, an effective gas for hydrogen to leak into with minimal chance for ignition. These gases can both safely be bled into the outside environment, although the mixture may need time to cool down during operation, when the leaking hydrogen is very hot [28]. Additionally, any materials used in external heating devices, gauges and other external equipment needed for monitoring and controlling the experiment will need to be protected from hydrogen attack. Also, the loop will have a pressure relief valve to a holding tank, which will also the high-pressure system to depressurize safely.

Perhaps most central in the discussion of materials selection is the choice of pipe for the test loop. Although it will likely be required for the higher temperature next phase of the project, active cooling with water will likely not be required for this phase if a material with a sufficient melting temperature is chosen. There are a suitable number of promising materials and alloys with a melting temperature above 1200 °C, including INCONEL 690, a high-chromium nickel alloy with promising corrosion-resistant properties. INCONEL 690′s melting range is between 1343 and 1377 °C, with a density of ~8 g/cm^3 and a thermal conductivity of 30.1 W/(m-°C) at 1000 °C [29]. However, the material selected for this study is Kanthal A-l, an iron-chromium-aluminum (FeCrAl) alloy, henceforth referred to as FeCrAl. FeCrAl has a melting temperature of 1500 °C, a density of 7.1 g/cm^3 and a thermal conductivity of 35 W/(m-°C) at 1400 °C [30]. While INCONEL 690 would have a higher thermal conductivity at 1400 °C (37.74 W/(m-°C) using linear extrapolation), FeCrAl has a superior melting point and lower density, making the fabricated pipes less heavy. As such, FeCrAl will be used as the pipe material selection for the majority of this study.

The BEARS hydrogen test loop will be circulating hydrogen at a chosen operating pressure of 12 MPa and mass flow rate (MFR) of 1 g/s. In an NTR comparable to the NERVA SNRE, the total MFR delivered to the nozzle is 40 kg/s with a pressure of 30.6 atm (3.1 MPa) [16]. To calculate the MFR in a single cooling channel, the total MFR must be multiplied by the ratio of the cross-sectional area of one cooling channel to the total cross-sectional area of the channels (circular holes with 0.098″ diameter, 22 per fuel element [23], 1100 elements in the reactor core [16]). This gives a channel MFR of 1.65 g/s, which is the basis for the BEARS loop MFR. The pressure chosen was selected based on the operating pressure of the KANUTER-LEU design, 13.9 MPa [12].

The preliminary sketch of the BEARS hydrogen test loop is depicted in Figure 3.1. Before moving on to the model itself a few practical points must be discussed. First, the pump in the system must be corrosion-resistant to handle hydrogen, and significantly cooled from the 1200 °C test section temperature, since at the time of writing this there are no commercially available pumps with a maximum inlet temperature above 460 °C. For the purpose of leaving a safety margin in case of transient temperature spikes, the model will require the pump inlet temperature to not exceed 400 °C. Heating of the hydrogen will be through either semi-circular ceramic heaters or resistive wire, heating the FeCrAl pipe through conduction. Owing to the high melting point of the FeCrAl pipe, water cooling is not expected to be necessary, and instead the cooling of the pipes will rely on forced convection through a high-temperature fan. Finally, the test section will need to be removable/accessible via port in order to insert and exchange test samples.

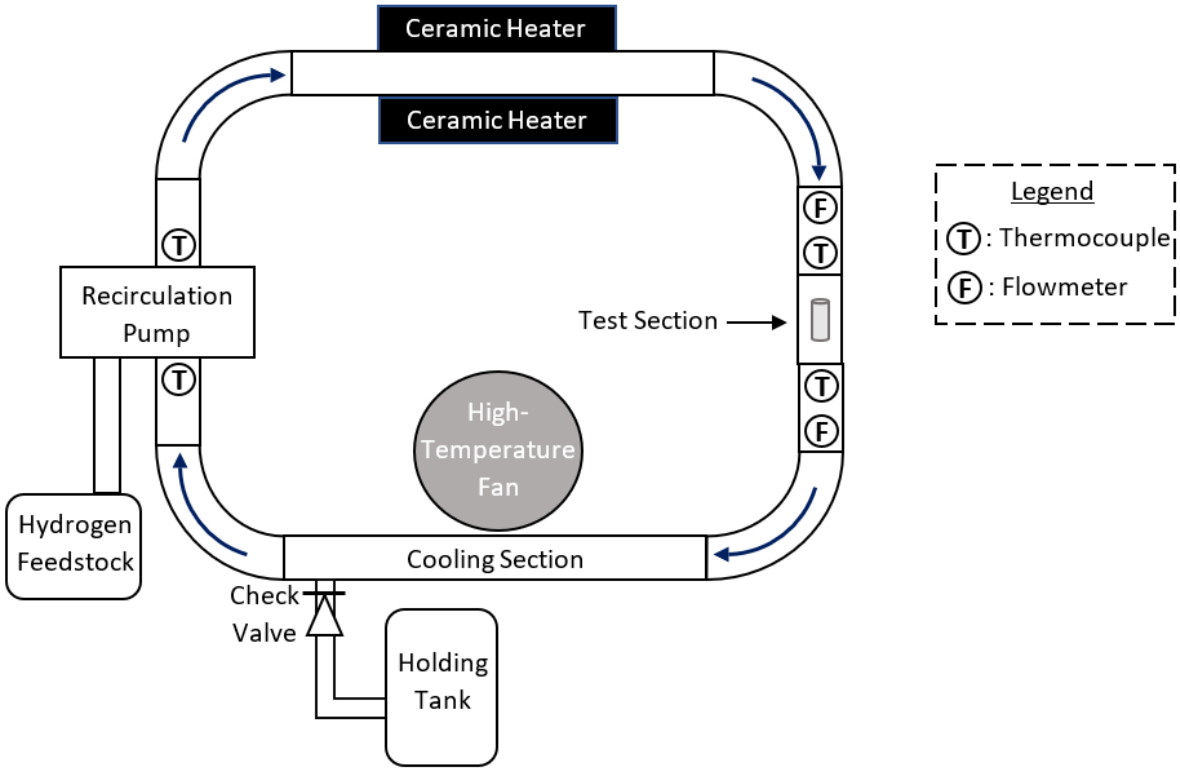

Figure 3.1: Block diagram of the BEARS hot hydrogen test loop

3.2 Model Assumptions

As is always the case with modelling, the complex nature of the real physics must be simplified and tailored in a way that allows for meaningful approximations of the solution to be made, and provide useful results for the modeler. So, in simulating the hydrogen flow through the loop and over the tie tube, the following assumptions will be made. First, the thermocouples and flowmeters necessary to monitor the hydrogen will likely have some effect on the flow locally, but for the purposes of the model they will be assumed to have no effect on the flow. Second, the hydrogen feedstock and the holding tank will be ignored, in addition to their accompanying pipes and valves, and the leak rates of hydrogen will be neglected. Third, the pump will be assumed to merely provide pressure without any other effects to the flow, and the heating elements will be idealized as a heat load directed onto the heating section pipe. For the steady-state thermal simulations, the model will be further idealized by discarding heat loads and using temperature conditions corresponding to the desired inlet and outlet temperatures. These SST models are not very robust because of this, and the CFD models from ANSYS Fluent should be taken as the representative thermal models of the loop′s flow.

The preliminary USNC tie tube model is depicted in Figure 3.2 below. The moderator elements, Zirconium Hydride pellets, are surrounded by a coating of Aluminum Oxide (Alumina) and placed touching end-to-end inside the tie tube′s shell. The tie tube shell has two candidate materials currently under consideration: SiC/SiC composite and TZM alloy. While this preliminary design does not have any structures and/or attachments that would hold up the moderator elements inside the tie tube shell, this will be addressed in a future design iteration, and the simulations here will treat the moderator elements as “floating” inside the shell.

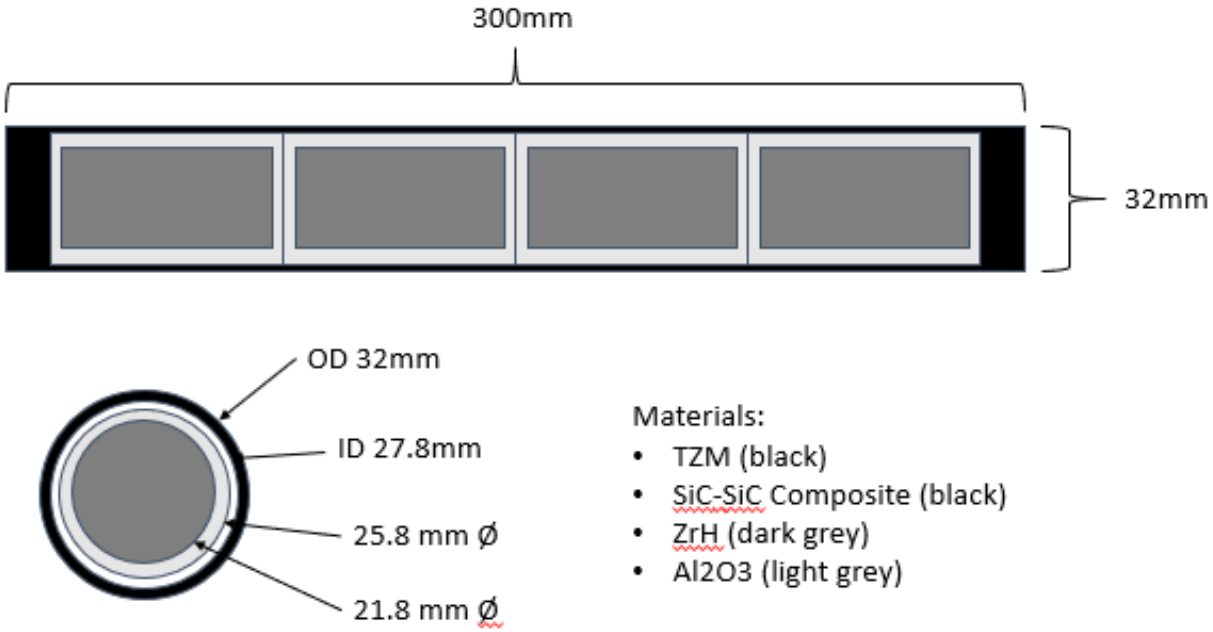

Figure 3.2: Illustration of the preliminary USNC tie tube design

The SST and CFD simulations were made using materials data from these sources: [29] [30] [31] [32] [33] [34] [35] [36]. The hydrogen fluid used in the simulations was neutral Hydrogen, taken from the native ANSYS materials database. The Alumina was assumed to be alpha phase, and the Zirconium Hydride was assumed to be delta phase ($ZrH_{1.6}$), with a molecular weight of ~93.237 g/mol. The thermal conductivity of $ZrH_{1.6}$ was approximated as a constant 18 W/(m-K) by extrapolating the source data. The SiC/SiC data used was for Chemical Vapor Infiltration non-reactive Melt Infiltration, or CVI-MI, with 18% fiber in the Y-direction. The specific heat values were taken as the highest in the range of values given, and the density value taken was for ceramic grade Nicalon (produced by Nippon Carbon). Specific heat data for Moly (TZM basically) found! The specific heat values were converted from cal/(g-°C) to J/(kg-K), assuming the unit "cal" is the thermochemical calorie.

For the SST and CFD models, values for convection were taken from F. Kreith et al. [37] for the average convection heat transfer coefficient of air, which makes a reasonable substitution for nitrogen gas. The convection heat transfer coefficient for natural (free) convection of air is given as a range from 6 to 30 W/(m^2-K), and a range of 30 to 300 W/(m^2-K) for forced convection of superheated steam/air. The minimum values of these ranges were chosen for free and forced convection conditions. For the Fluent CFD runs, the thermal conductivities of all solid materials were set as constant to accommodate handling of "thin walls", and the highest values from the sources above were selected. Additionally, the Fluent models simulate only the heating section, test section and cooling section of the BEARS loop, with the geometry modified to a straight pipe design with no bends. The presence of bends in the final loop design will likely have a measurable effect on the flow of hydrogen, which will be discussed later in the Results section.

The primary goals of these simulations is to accurately predict the temperature and velocity distributions of the flowing hydrogen, the FeCrAl pipe and the tie tube elements, in order to predict a heat load that would supply the desired 1200 °C inlet condition to the test section. The effects of FeCrAl pipe size will also be examined, with the intent of finding the design that uses the minimum feasible amount of pipe material. Additionally, the effects of a high vacuum condition outside the test loop system will be examined in order to bring the simulation closer to the realistic operating conditions of a space reactor. The progression of simulation work done will be now be presented, along with the underlying assumptions of each model and a brief discussion of the results from each iteration. A more rigorous discussion of the results from the bulk of the simulation work will be presented in Chapter 3.4.

3.3 Modelling Iterations

The following iterations of the BEARS hydrogen test loop modelling are presented in chronological order, with exceptions as noted. Steady-State Thermal models will be presented first, with the more robust Fluent CFD models presented afterwards. These simulations were all run on a laptop personal computer running the Windows 10 Basic operating system, using the ANSYS 2020 R1 Student version. As will soon become clear, some of the simulations have some error associated with this version, since it is a free version which in exchange for the cost puts size limits on the problems that can be run. This will be discussed further in Chapter 3.4, discussion of results.

3.3.1 Steady-State Thermal models

For the first SST model, the choice of FeCrAl as the BEARS loop pipe material had not yet been made, so INCONEL 690 was used as the initial pipe material. The thermal conductivity values for this and all other models were assumed to be isotropic. A pipe section with an Inner Diameter (ID) of 20 mm and an Outer Diameter (OD) of 25 mm was extruded to a length of 100mm, and meshed using the default Face Meshing map on the pipe′s inlet face. The ID of the pipe′s inlet face was set with a temperature condition of 1200 ℃, and the outside face was set to natural convection (6 W/(m^2-K)) to a 22 ℃ air environment. This simple INCONEL and air system was a test to confirm the set-up was working correctly, and the temperature distribution is shown in Figure 3.3. As expected, the temperature decreases steadily along the pipe′s axial (Z) direction, confirming the solution′s accuracy.

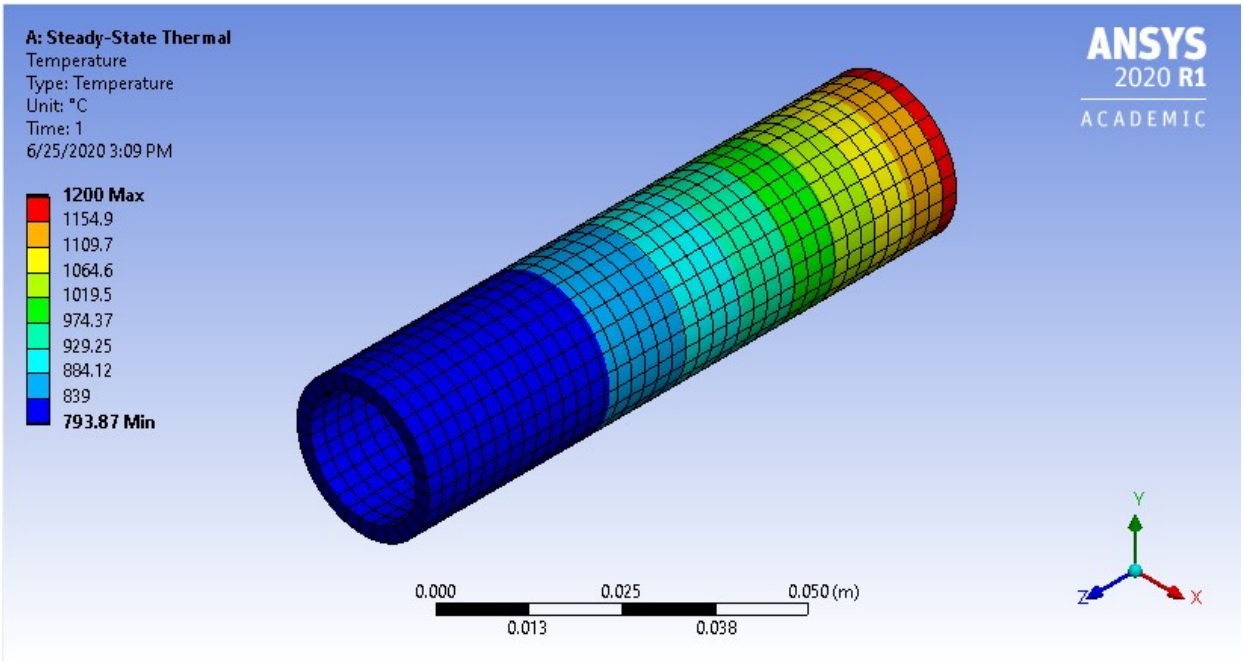

Figure 3.3: SST model of INCONEL 690 pipe, 20 mm ID & 25 mm OD

Following this simple model, a full loop geometry was constructed using the same ID, OD and 100 mm extrude length, now with 180° revolved sections to roughly mimic the heating and cooling sections. The mesh was applied this time to all four outside faces of the loop, the same temperature condition was applied to the inlet edge of the test section pipe, with natural convection on all outside faces. The resulting temperature distribution is shown in Figure 3.4 and shows the sharp increase in temperature that the bended sections would experience in such a small loop size. This large thermal gradient should be minimized in the final design in order to reduce the risk of cyclic degradation of the loop's pipes and premature failure.

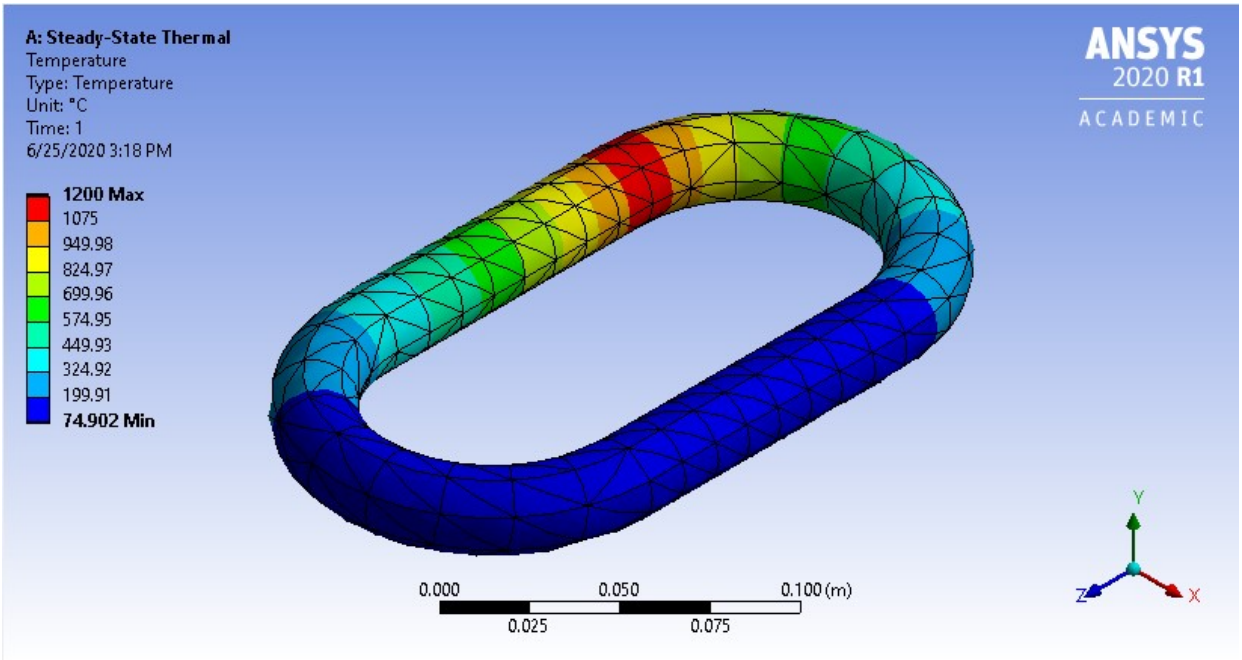

Figure 3.4: SST model of INCONEL 690 loop, 20 mm ID & 25 mm OD

After this model, FeCrAl was selected as the desired pipe material, and all future designs will use FeCrAl as the loop's pipe material. The next series of models were an attempt to incorporate hydrogen inside the loop pipes, and the geometrical model extrudes now used the 'Add Frozen' operation rather than 'Add Material', in order to incorporate extruded geometries interfacing one another. Since the tie tube model was not yet known, the test section pipe was again only 100 mm in length. The mesh was refined this time using an edge sizing method on the pipe's ID and OD, and the hydrogen's edges, with 25 hard divisions. The same inlet temperature and was applied, and all models in this series use natural convection conditions on the outside pipe faces.

A command ('outres,erase', 'outres,all,all') was inserted in order to output results usually suppressed by the solution window, to allow the pipe's temperature (thermal) gradient and thermal conductivity to be outputted. Outputting the thermal conductivity serves as a check that

the solution is producing values similar to the input thermal conductivities of the materials used. The temperature and thermal conductivity profiles of this pipe and hydrogen system are shown in Figures 3.5 and 3.6. In order to output the magnitude of the total thermal conductivity, the magnitude of the component Cartesian thermal conductivities was taken, where each component thermal conductivity was found from the 1-dimensional form of Fourier's Law of Heat Conduction:

$$k_x \left[\frac{W}{m * K}\right] = \frac{q_x \left[\frac{W}{m^2}\right]}{\nabla T_x \left[\frac{K}{m}\right]} \tag{3.1}$$

Equation 3.1 is written in the Cartesian X-direction as an example, where q_x is the local directional heat flux, ∇T_x is the temperature gradient, and k_x is the thermal conductivity. The thermal conductivity values in Figure 3.6 are within a reasonable range (FeCrAl has a thermal conductivity of 26 W/(m-K) at 1000 °C [30]), which helps confirm the validity of the results.

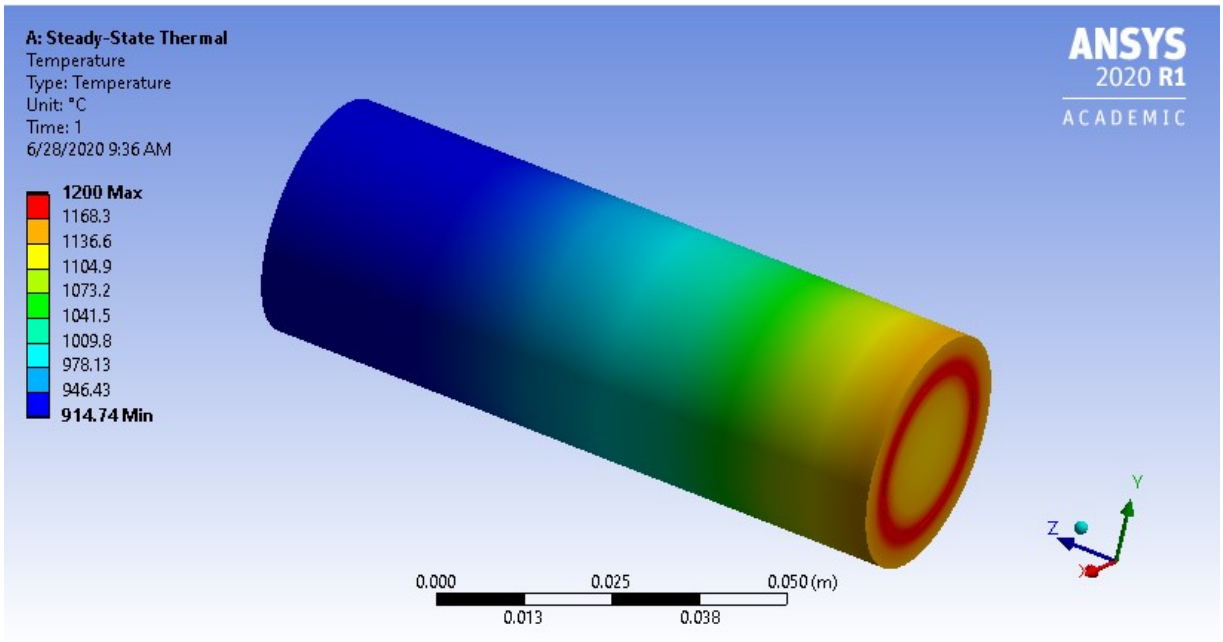

Figure 3.5: SST temperature of FeCrAl pipe, 20 mm ID & 25 mm OD

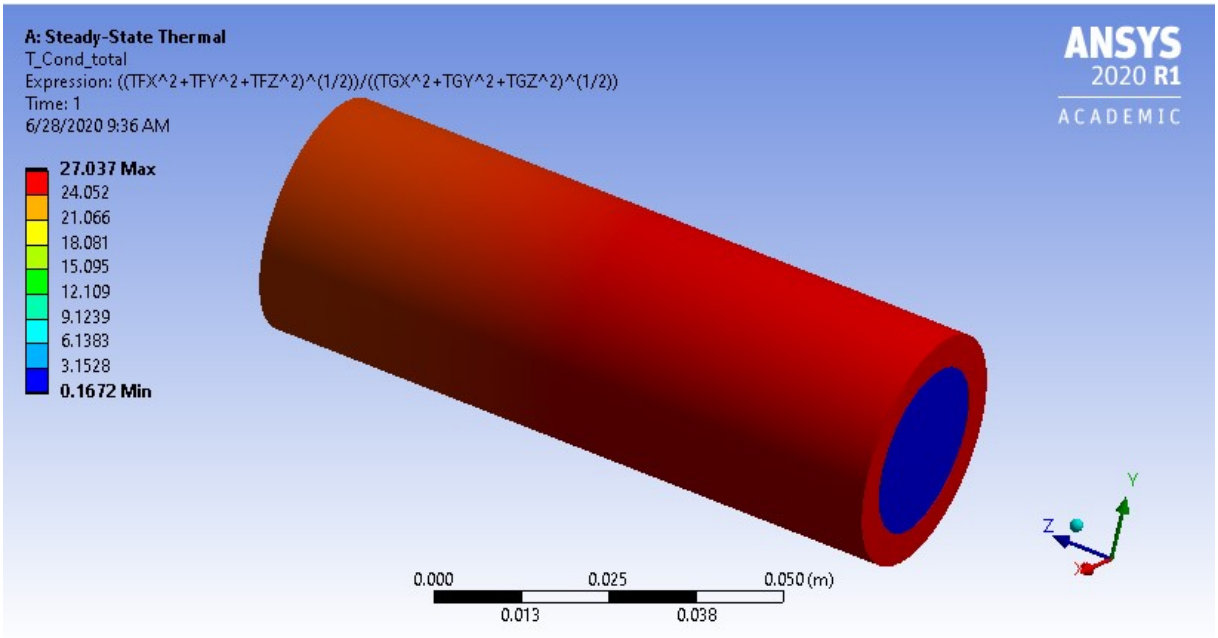

Figure 3.6: SST thermal conductivity of FeCrAl pipe, 20 mm ID & 25 mm OD

The second iteration in this series extended the geometry to a full loop design, this time with 90° sections akin to the BEARS loop diagram in Figure 3.1. The ID and OD of the FeCrAl were modified to 25.4 mm and 35.4 mm, respectively, with the test section and pump section of pipe at an extruded length of 300 mm, and the side lengths of the heating and cooling sections at 300 mm as well. Owing to the size of the problem, the mesh edge sizing refinement could only accommodate 10 hard divisions for the pipes' IDs and ODs. While the thermal loading conditions for these next few iterations are not the most realistic, the intent was to determine the magnitude of the thermal gradient to determine the proportions of a favorable design. This iteration set temperatures of 1200 °C for the hydrogen in and next to the test section, and 400 °C for the hydrogen in and around the pump section. The magnitude of the total thermal gradient for this design is shown in Figure 3.7. This gradient is unrealistic and far too sharp for a feasible system.

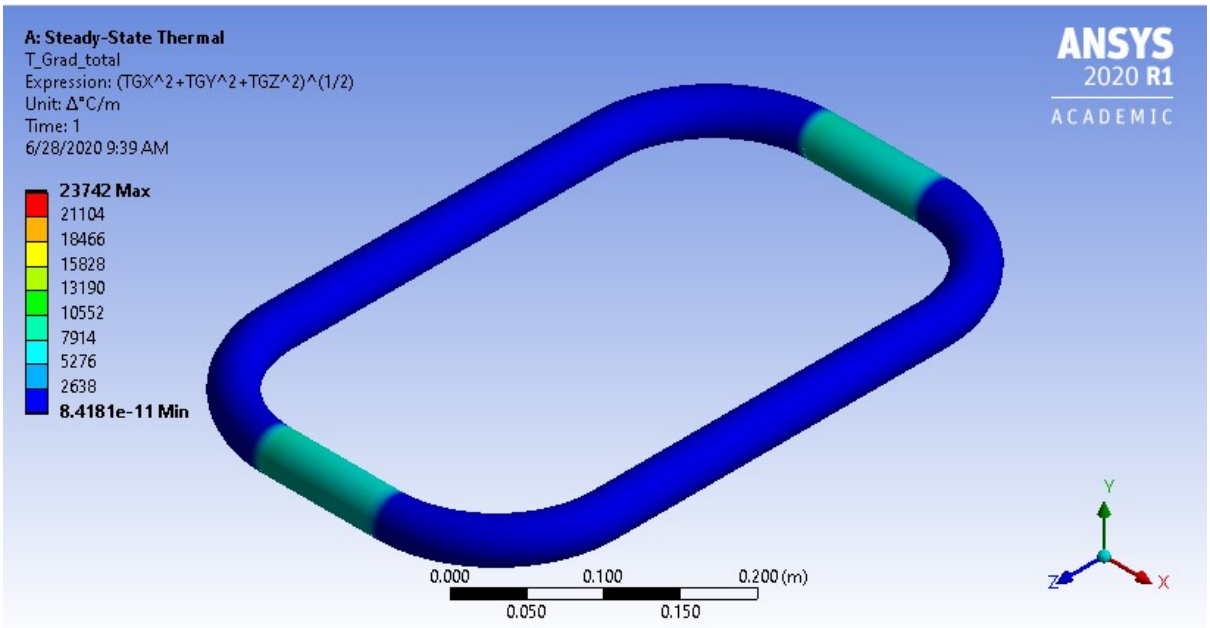

Figure 3.7: SST thermal gradient of FeCrAl loop, 25.4 mm ID & 35.4 mm OD

In the third iteration, the heating and cooling sections were modified to have a continuous 180° bend instead of including any straight pipe, with cross-sections and side lengths unchanged from the second iteration. The mesh refinement method remained the same, and the temperature conditions were changed so that the hydrogen at and immediately after the test and pump sections were set to 1200 °C and 400 °C respectively. The thermal gradient magnitude is shown in Figure 3.8. This design improves the thermal gradient slightly but is still too high.

The fourth iteration uses the same shape as the third iteration, but doubles the heating and cooling side lengths to 600 mm. The remaining input conditions are the same, except that the number of meshing edge divisions had to be reduced to 6. The thermal gradient magnitude is shown in Figure 3.9 and shows no significant reduction in thermal gradient.

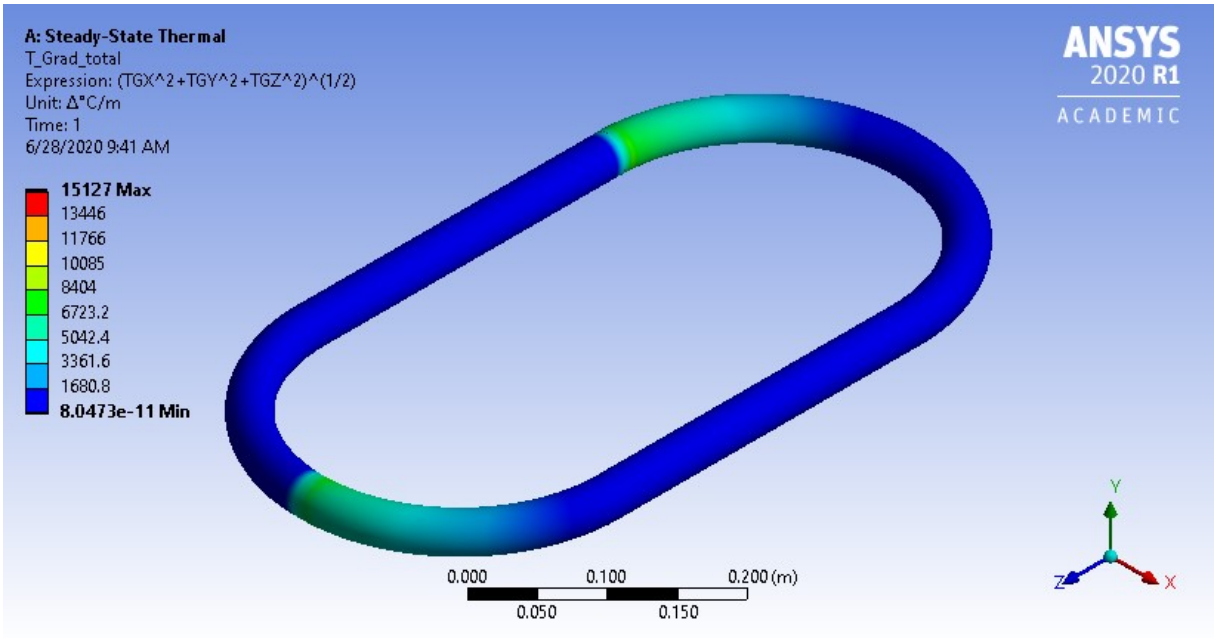

Figure 3.8: SST thermal gradient of rounded FeCrAl loop, 25.4 mm ID & 35.4 mm OD

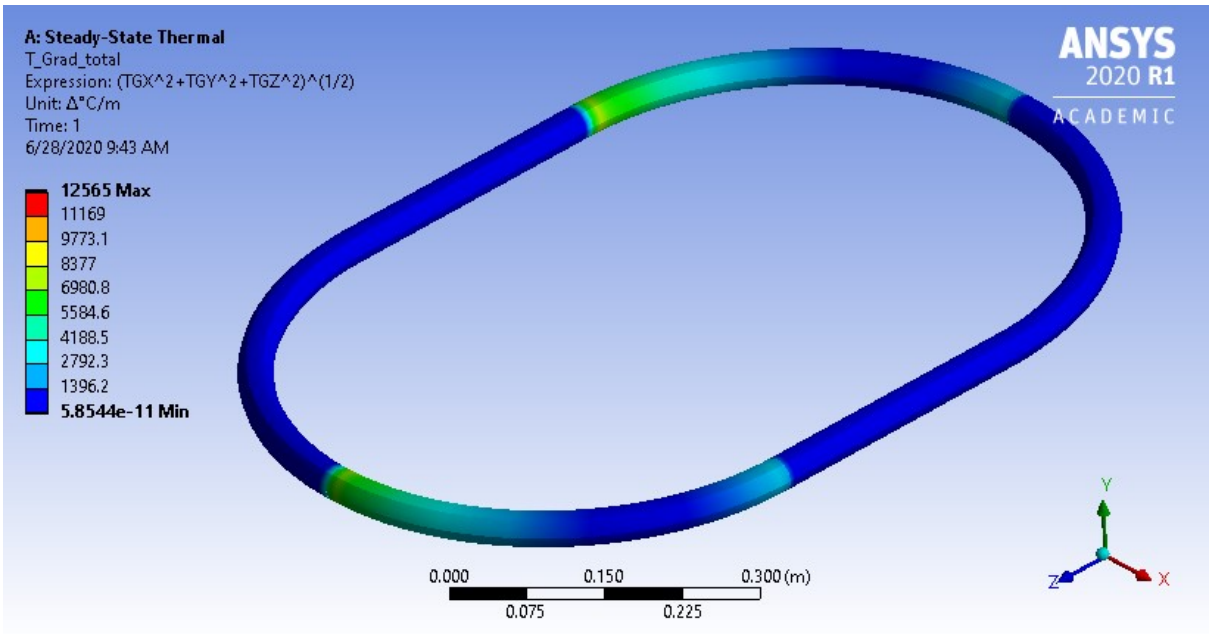

Figure 3.9: SST thermal gradient of larger rounded FeCrAl loop, 25.4 mm ID & 35.4 mm OD

The fifth and sixth iterations are simply increases in the size of the fourth iteration's geometry, and show further small decreases in thermal gradient magnitude. The proportions remained the same, with the test and pump sections extended to 500 mm and 700 mm respectively. The mesh refinement had to be suppressed due to the problem size. Since the decreases in thermal gradient were not significant, they will not be shown here. This did provide some confidence that a larger loop design was unnecessary, with a total loop arc length of ~2 m targeted for the final design.

Following this series of loop designs, a series of SST models with tie tube models incorporated were evaluated. The first in this series was a legacy model of the tie tube by itself, with a design more complicated than the current design. An isometric view of the legacy design is shown in Figure 3.10, and shows a flow path of hydrogen coming in through the smallest, central tube, turning around in a dome-shaped cavity, and returning through an annular tube back the same direction as entering.

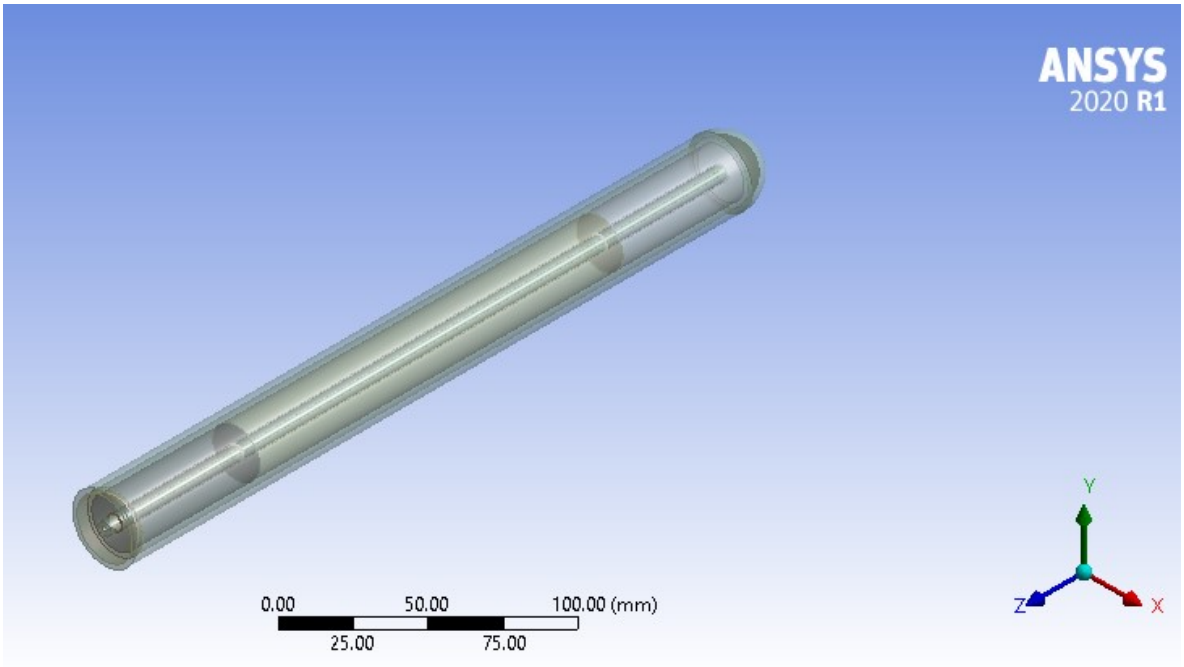

Figure 3.10: Isometric view of legacy USNC tie tube model

Because of this complexity, among other factors, the USNC tie tube model was modified to the current form as seen in Figure 3.2. Because of the irrelevance of this first iteration in the series to the bulk of simulations, and its lack of robust results, this iteration's results are not presented here.

The second iteration incorporates the current tie tube design, and includes cases for both SiC/SiC and TZM tie tube shells. The test loop is reduced to a 400 mm test section pipe, with an ID of 40 mm and an OD of 50 mm. The tie tube model is Boolean subtracted from the hydrogen zone. The mesh for this model incorporates Face Sizing refinement, selecting an element size of 8 mm for the outer faces of the moderator covers, and the interfaces of the hydrogen with the tie tube. The temperature condition of 1200 °C is on the face of hydrogen at the test section inlet, with natural air convection on the pipe. The resulting temperature and thermal gradient for the SiC/SiC tie tube are shown in Figures 3.11 and 3.12 respectively. The results are not very realistic for flowing hydrogen, but more importantly the mesh for the tie tube is coarse enough to distort the design. This can be seen in the temperature distribution of the SiC/SiC tie tube in Figure 3.13.

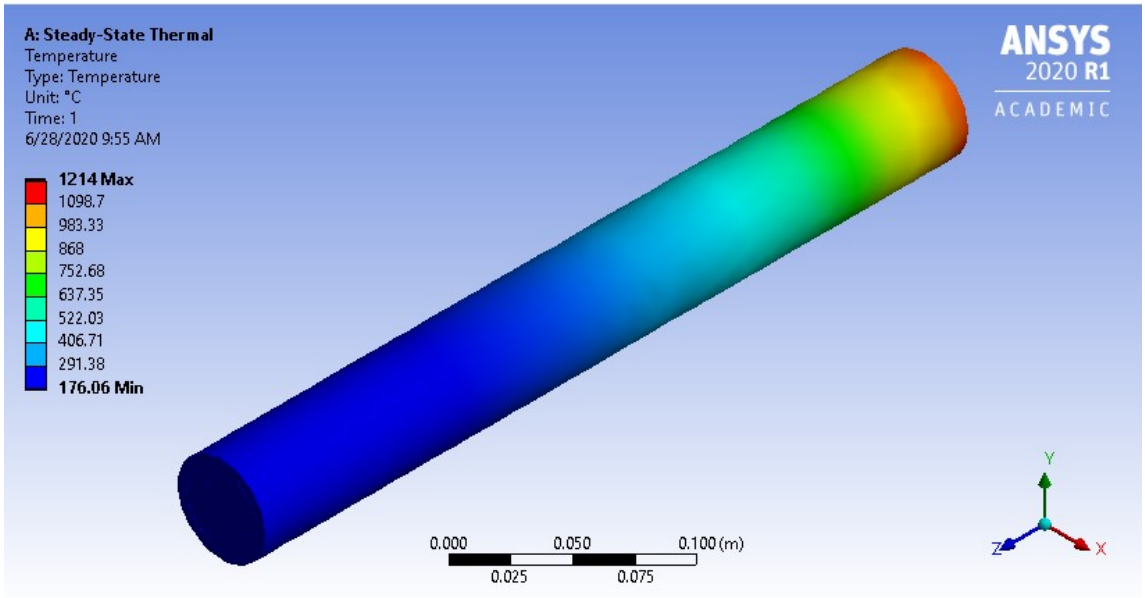

Figure 3.11: SST temperature of FeCrAl pipe, 40 mm ID & 50 mm OD

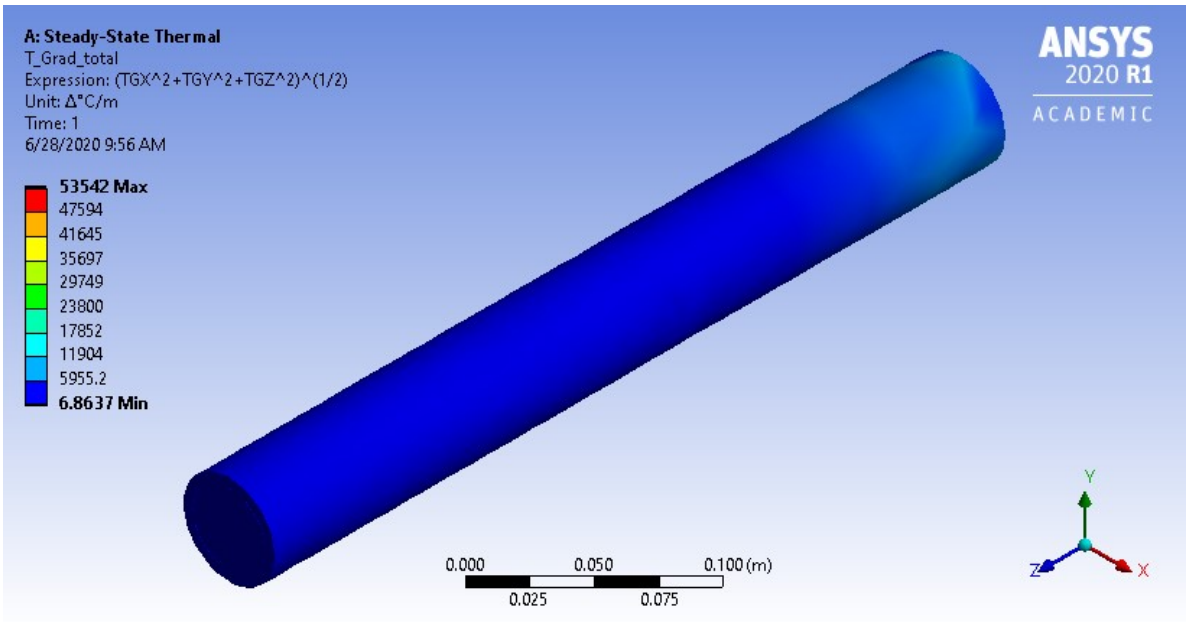

Figure 3.12: SST thermal gradient of FeCrAl pipe, 40 mm ID & 50 mm OD

The tie tube shell temperature for the TZM case of the second iteration is shown for comparison in Figure 3.14. The results show a decrease in thermal gradient for the TZM tie tube shell, suggesting better heat transfer in the TZM.

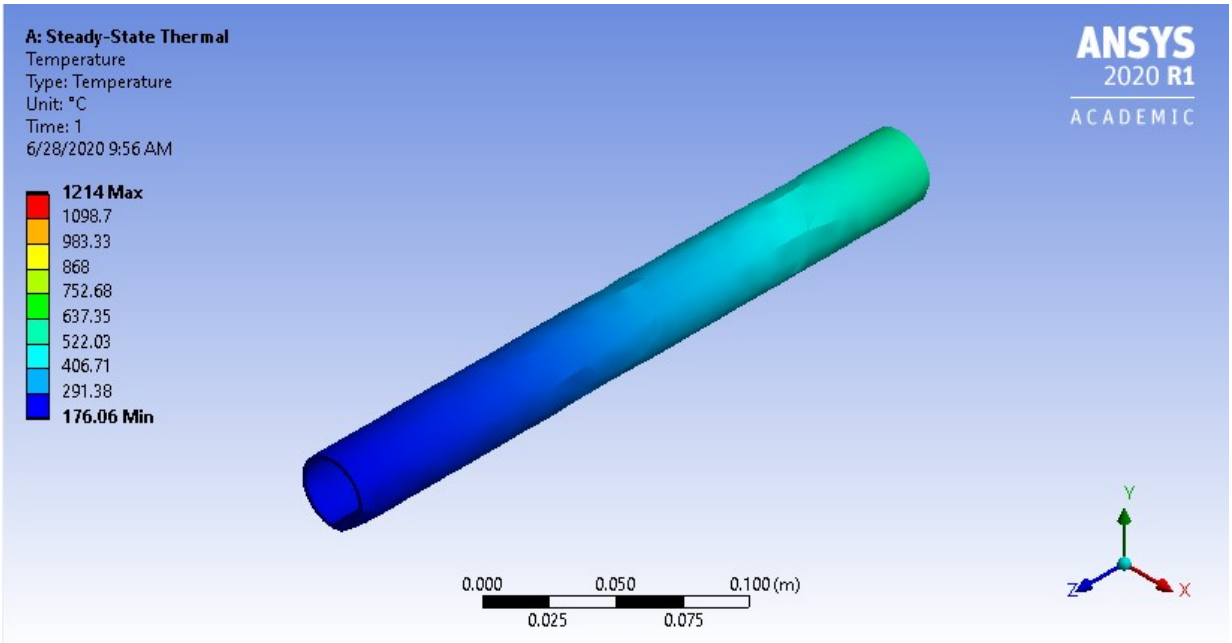

Figure 3.13: SST temperature of SiC/SiC tie tube

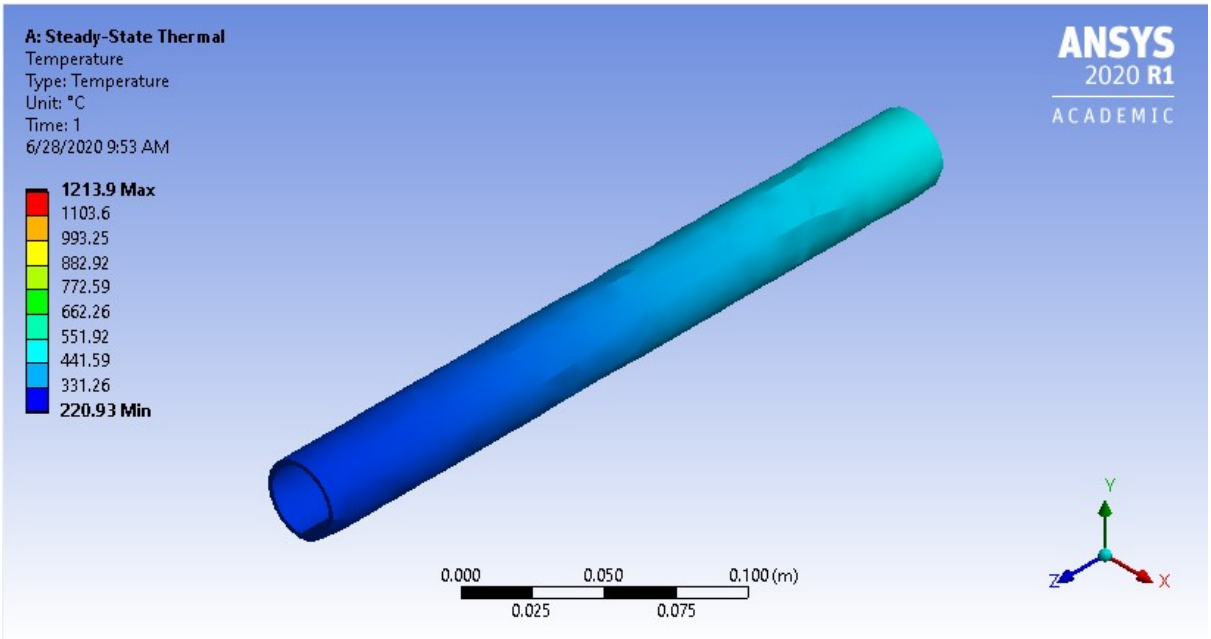

Figure 3.14: SST temperature of TZM tie tube

The third iteration in this series implements forced convection (30 W/(m^2-K)) on the outside faces of the FeCrAl pipe. The geometry and temperature condition remain unchanged from the second iteration, and the meshing refinement includes the ends of the tie tube shell, FeCrAl pipe and hydrogen. The temperature, thermal gradient and tie tube temperature profiles for the SiC/SiC case are shown in Figures 3.15, 3.16 and 3.17, respectively. The distortion in the mesh and results have improved, and the forced convection allows the test section outlet to cool back to a room temperature range. The thermal gradient has noticeably increased, but this effect would likely be lessened by flowing hydrogen.

The temperature results for the TZM mirror the relationship seen in Figures 3.13 and 3.14, and thus the temperature results for the TZM case under forced convection will be omitted.

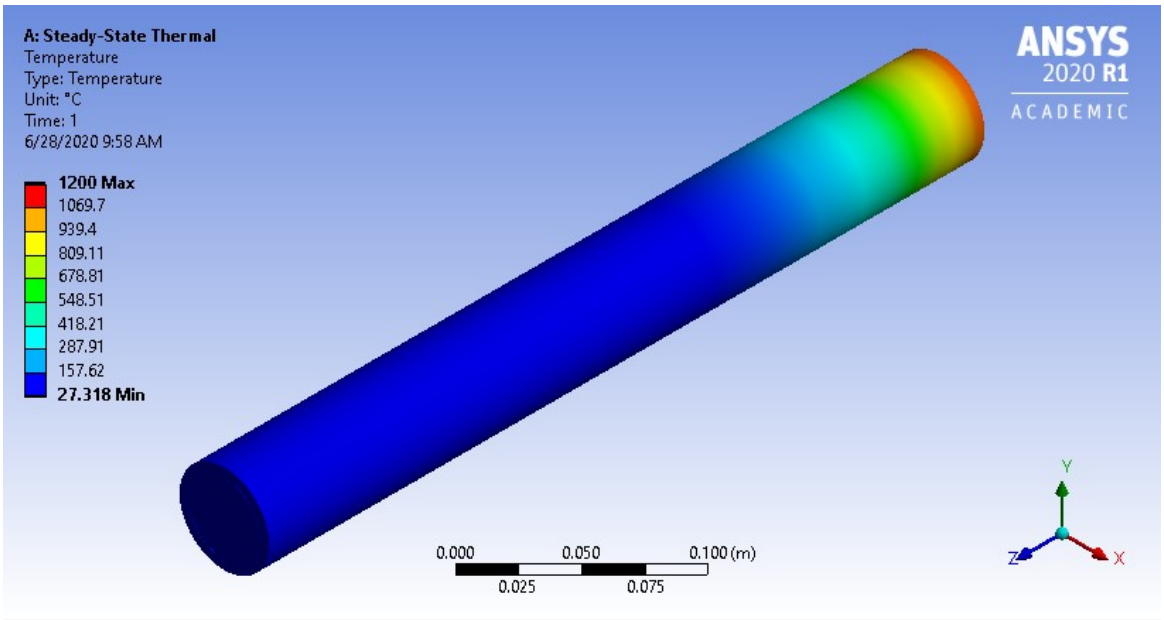

Figure 3.15: SST temperature of FeCrAl pipe, 40 mm ID & 50 mm OD, forced convection

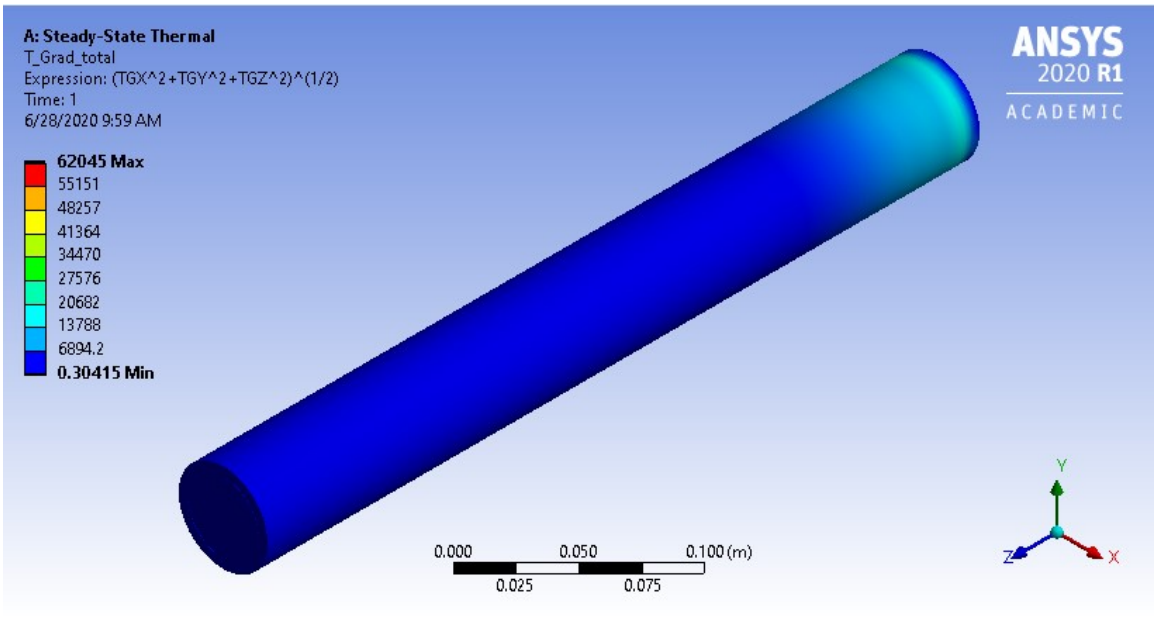

Figure 3.16: SST thermal gradient of FeCrAl pipe, 40 mm ID & 50 mm OD, forced convection

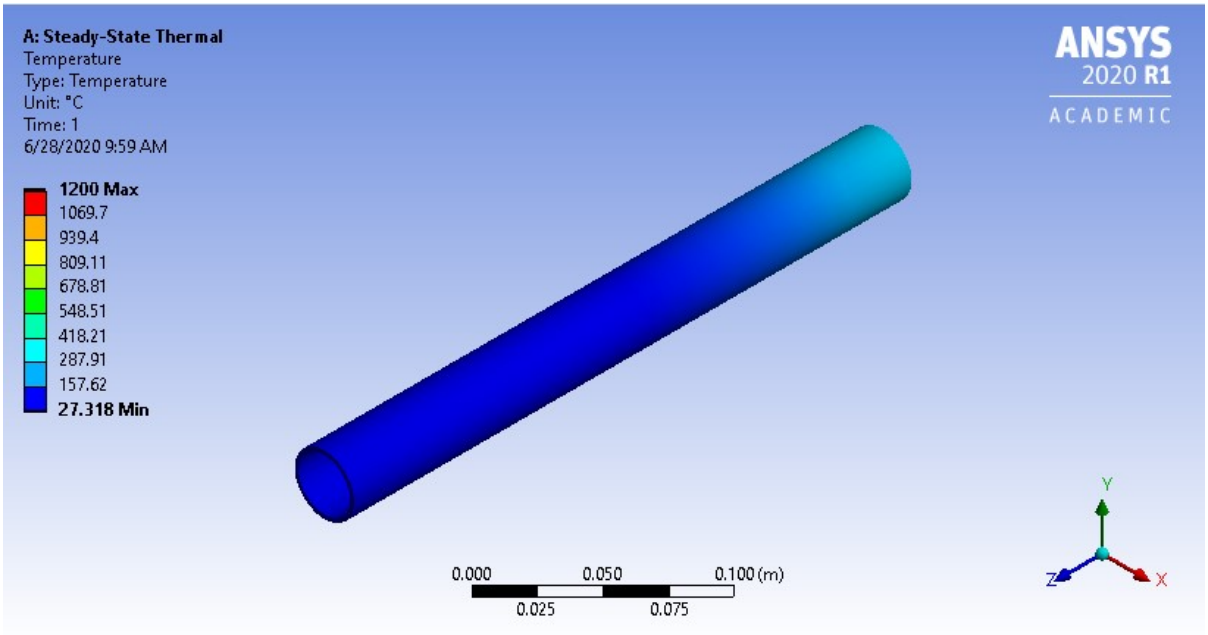

Figure 3.17: SST temperature of SiC/SiC tie tube, forced convection

The forth iteration expands the geometry of the test loop to a fully enclosed loop, with the test section, pump section, heating section and cooling section all given a 400 mm extruded straight pipe, and connected via 90° rounded pipe sections with side lengths of 200 mm. The mesh refinement of 8 mm element sizing was only applied to the moderator covers and the test section hydrogen-tie tube interfaces, due to the size of the problem approaching the limit. In order to further approach a realistic model of test loop conditions, a heat flux load was applied to the straight heating section pipe, with the magnitude manually adjusted to produce a test section inlet of 1200 °C. This was found to be ~1e5 W/m^2. The results for the test section temperature, thermal gradient and SiC/SiC tie tube temperature are shown in Figures 3.18, 3.19 and 3.20.

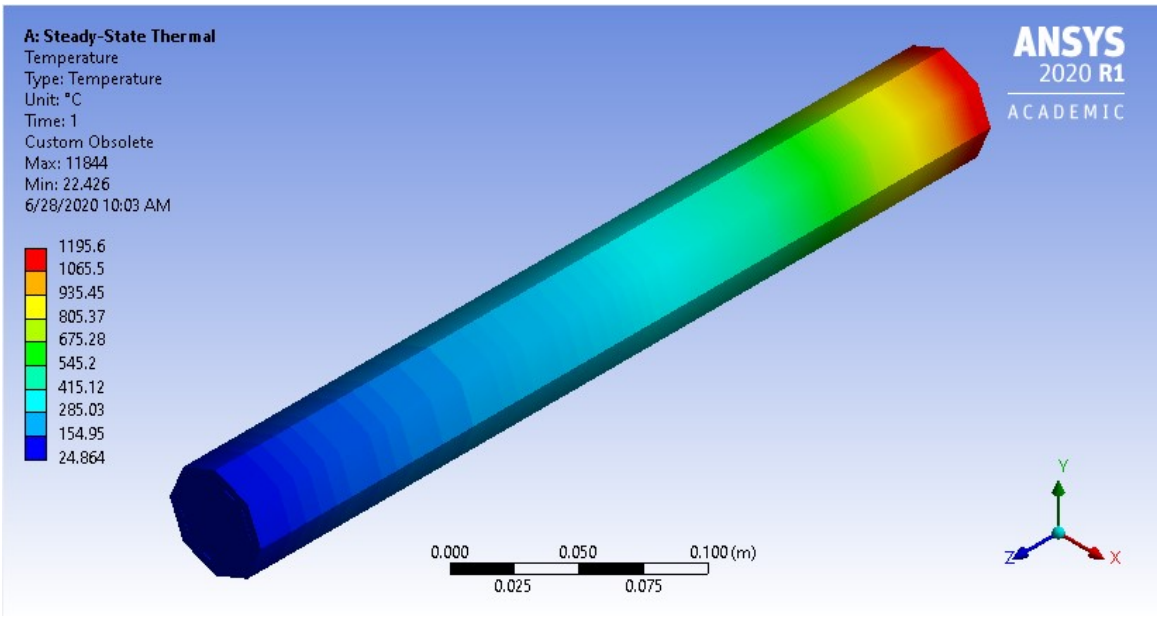

Figure 3.18: SST temperature of FeCrAl loop test section, 40 mm ID & 50 mm OD

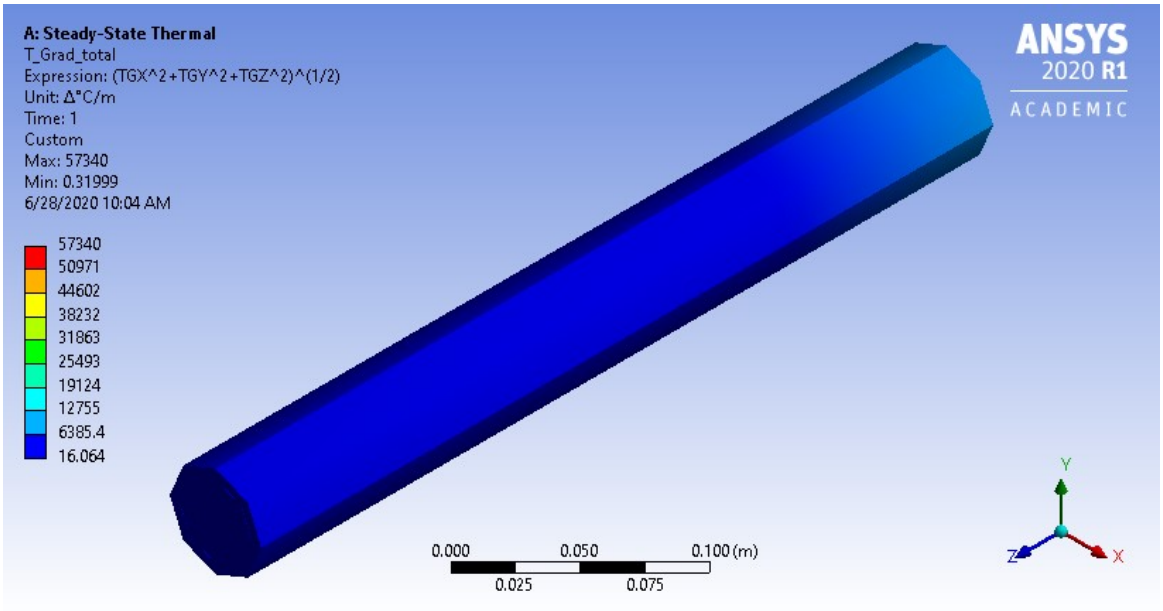

Figure 3.19: SST thermal gradient of FeCrAl loop test section, 40 mm ID & 50 mm OD

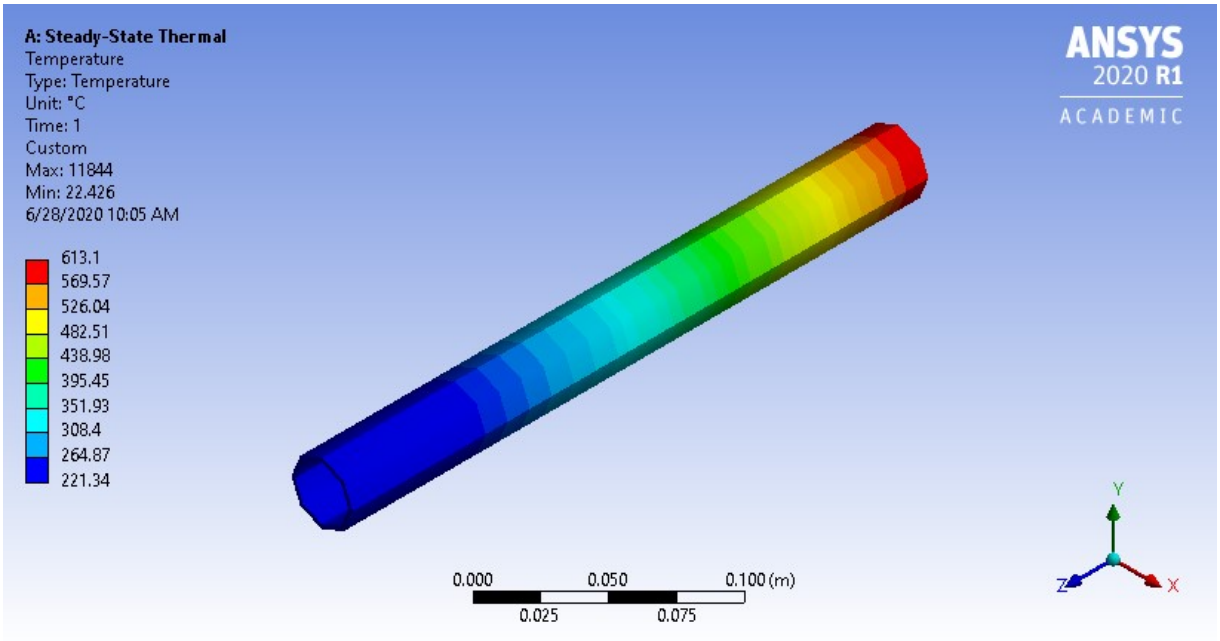

Figure 3.20: SST temperature of SiC/SiC tie tube in FeCrAl loop

This series of models, and this iteration specifically, do well to highlight the weaknesses of SST modeling for the BEARS loop's design. Without flowing hydrogen, the temperature of the test section pipe drops from ~1200 °C to room temperature from inlet to outlet. The scales for Figures 3.18 to 3.20 are restricted to the visible elements, which indicate large thermal gradients in the test section hydrogen. Also, the mesh refinement process gradually became more restricted, showing some signs of reducing accuracy of the simulations. In completing these series of runs it became clear that a model encompassing hydrogen flow behavior would be important in correctly predicting the thermal distributions of the FeCrAl loop and the tie tube.

3.3.2 Fluent CFD models

Adapting the latest SST model to encompass fluid flow proved nuanced and slow-going, for reasons that will be elaborated on with each iteration. In the first iteration, a 400 mm FeCrAl pipe, a hydrogen region inside and the current USNC tie tube model were imported from ANSYS's DesignModeler geometry handler to the most recent handler, SpaceClaim. This was done after Fluent encountered difficulties with the interfaces between different material zones, and was done in order to use SpaceClaim's ability to Share Topologies of all geometries. In the mesh, Inflation layers with default behavior were placed on the hydrogen and its interfaces with the tie tube. This iteration's mesh has a large number of elements that are significantly skewed, which can be seen in Figure 3.21, and suggest a poor quality of solution in the proximity of these elements.

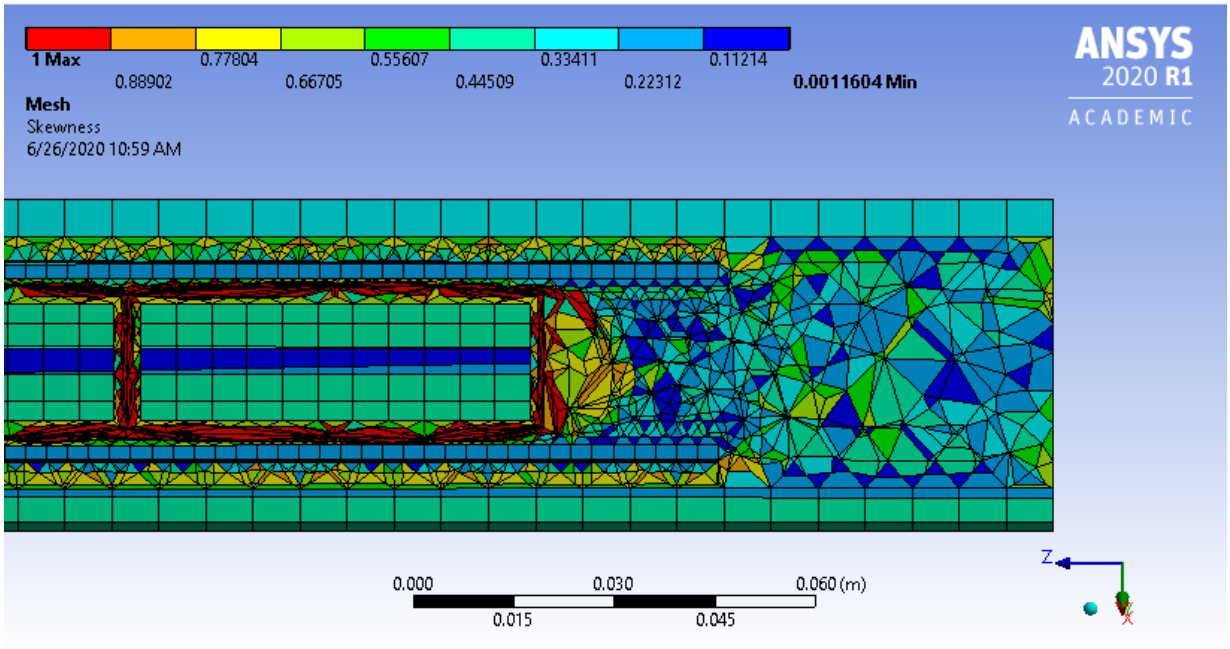

Figure 3.21: Cutaway view of Fluent test section mesh skewness, 40 mm ID & 50 mm OD

The inlet and outlet faces of the hydrogen were set as Named Selections, and Fluent was set up for a 3-dimensional problem with Double Precision, using 4 local parallel solver processes intended to speed up solution times. The materials data for a SiC/SiC tie tube case was entered in, and the k-omega SST model was set for viscous effects. Because the Reynolds number, a measure of the flow's tendency towards turbulence, was not yet known the k-omega model was used as it was the default. The energy equation was turned on, although as will be seen soon, this is not accurate when there are no energy source terms. The cell zones were set to their respective materials, and the walls were all set to coupled with 0 wall thickness except for the FeCrAl outer wall, which was set to 0 heat flux and 0 wall thickness. This will prove problematic in the solution. The inlet condition was defaulted to a velocity condition, and the magnitude of the velocity was solved for using the 1-dimensional formula for MFR:

$$\dot{m}\left[\frac{kg}{s}\right] = \rho\left[\frac{kg}{m^3}\right] u\left[\frac{m}{s}\right] A[m^2] \tag{3.2}$$

In Equation 3.2, the inlet velocity u was calculated using the 1 g/s MFR decided in Chapter 3.1, the FeCrAl pipe's cross sectional area using the ID of 40 mm, and the density of hydrogen as found using the National Institute of Standards and Technology (NIST)'s Chemistry WebBook reference [38] for a pressure of 12 MPa and the highest temperature value listed, 1000 K. This yielded an inlet velocity of ~0.07 m/s. The inlet temperature was set to 1473 K (1200 °C) and the turbulence parameters were left as their defaults. The outlet condition defaulted to a pressure outlet, and a backflow temperature of 1473 K was set, with the pressure at inlet and outlet set to 12 MPa. Before initialization of the problem was successful, the zones needed to be slit via a recommended command in order to handle adjacent interfaces of different materials. The standard initialization was used, and the calculation was run. Because of the improper boundary

conditions set for this problem, the solution remained unconverged after 200 iterations, with the scaled residuals remaining near one. The outlet condition was modified to prevent reverse flow, but the solution was still of a low quality. While the pressure in the test section remained at 12 MPa, the temperature of the tie tube achieved an astonishing and unphysical ~1950 K. The temperature and pressure contours of the system can be seen in Figures 3.22 and 3.23.

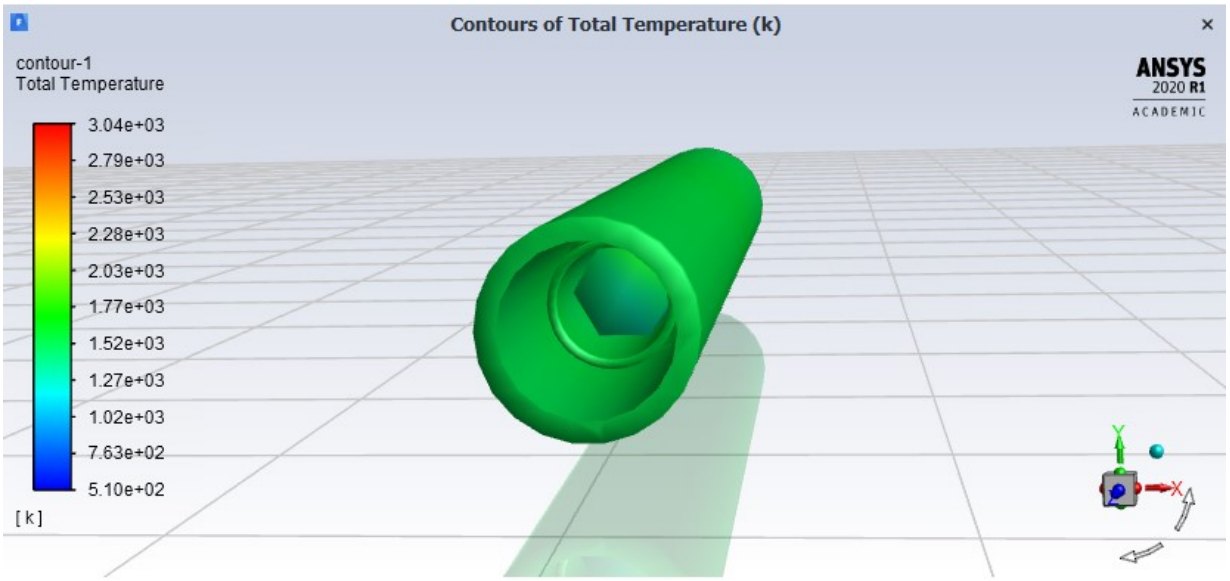

Figure 3.22: Contours of Fluent test section temperature

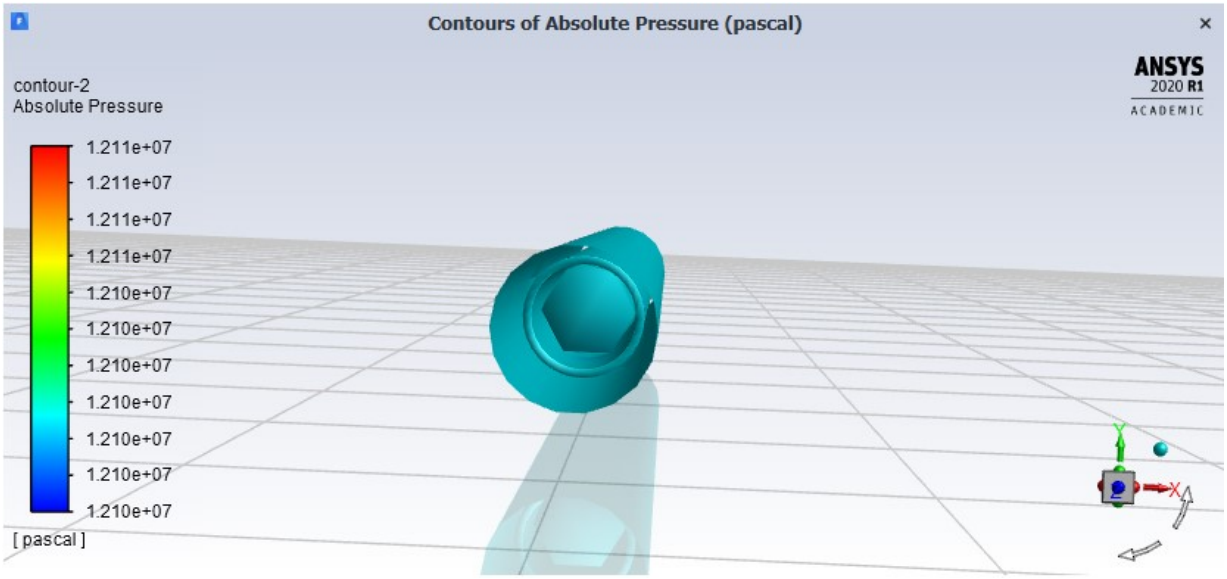

Figure 3.23: Contours of Fluent test section pressure

Following this configuration, several important changes were made to the model to improve the flow characteristics and the accuracy of the model. First, the geometry was modified to include 800 mm heating and cooling section pipes, in a linear fashion. Second, the mesh refinement was improved using the edge sizing method, with 40 hard divisions on the edges of the moderator covers and test section pipe, and 60 hard divisions on the edges of the tie tube shell. Further refinement was attempted but unsuccessful due to problem size limitations in the solution phase. The improvement in mesh skewness reduction can be seen in Figure 3.24. Third, section planes were implemented in all sections of the simulation (including the previous configuration) to improve visualization over the contour plots of Figures 3.22 and 3.23.

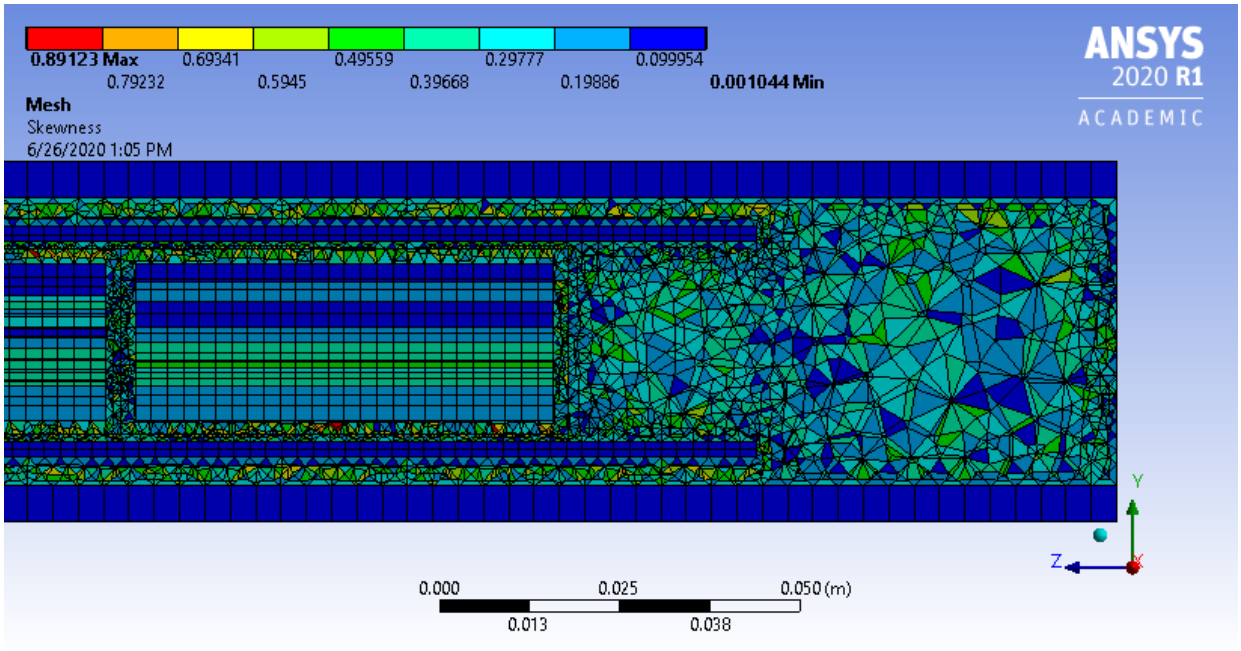

Figure 3.24: Cutaway view of test section with better mesh skewness, 40 mm ID & 50 mm OD

To check the accuracy of the flow profile alone, the energy equation was turned off. The inlet condition was changed to a mass flow inlet, in order to more directly implement the 1 g/s target operation condition. The reference frames for the inlet and outlet were changed to 'Relative to Adjacent Cell Zone', and the direction specifications were set to 'Normal to Boundary'. As with the previous configuration, the wall conditions remained at standard roughness, stationary walls and no slip shear conditions. The initialization method was changed to Hybrid Initialization, using 30 iterations and standard under-relaxation factors of 1. Upon initialization convergence, the solution was again run for 200 iterations. After some experimentation with viscous models, the k-epsilon 2 equation method with enhanced wall treatment was found to converge all residuals below 1e-04. The scaled residuals can be seen in Figure 3.25. The flow Reynolds number can also be reasonably determined, and as can be seen in Figure 3.26, the flow is essentially laminar since the maximum Reynolds number is less than 1000 [39].

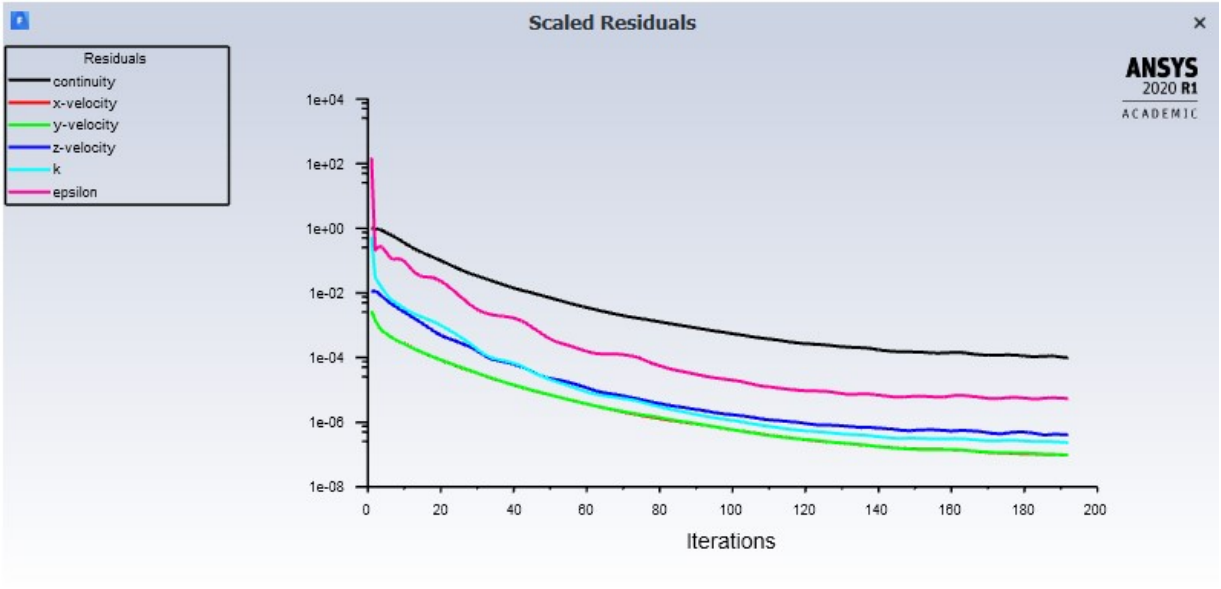

Figure 3.25: Scaled residuals of unheated linear test loop, 40 mm ID & 50 mm OD

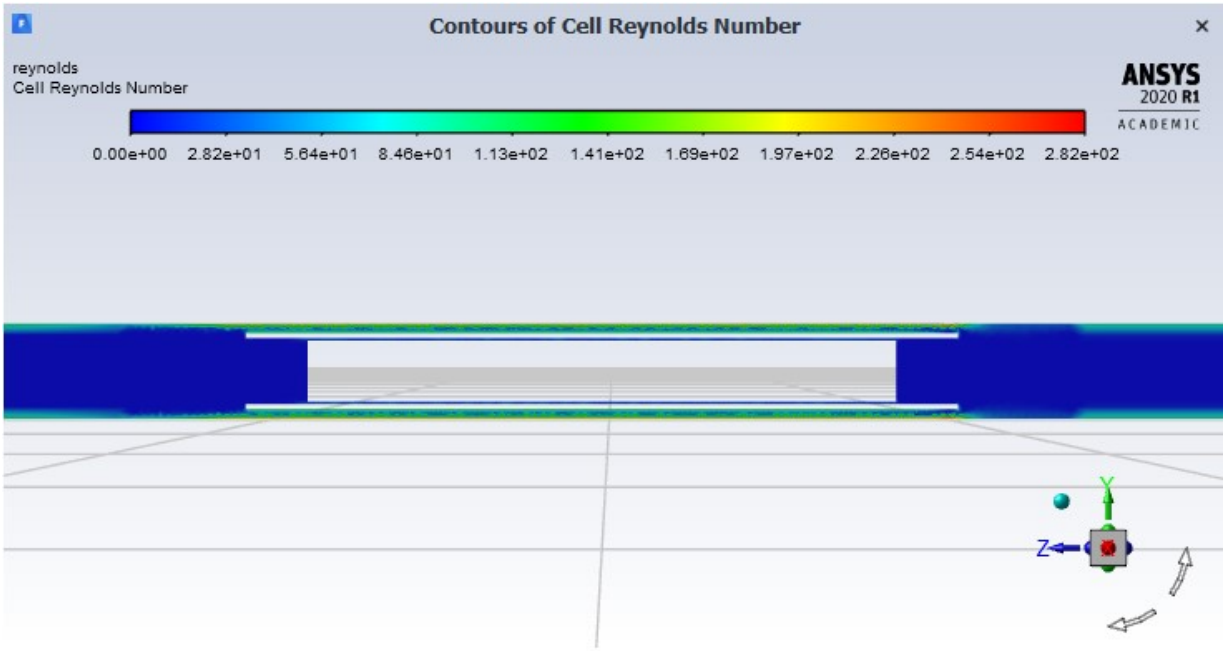

Figure 3.26: Cell Reynolds Numbers of unheated test section, 40 mm ID & 50 mm OD

Following this successful run, the simulation was modified to include the energy equation, with a heat source of 1e8 W/m^3 placed on the heating section of FeCrAl pipe. This value was manually determined to produce test section inlet temperatures near the desired 1473 K. The outer FeCrAl wall zones were set to a Mixed thermal condition, rather than System Coupled like the rest, and set for a heat transfer coefficient of 6 W/(m^2-K) (natural convection) and an External Emissivity of 1 (black body radiation, an idealization). The inlet temperature coming into the heating section was set as 673 K, and the backflow temperature was set to 300 K. The final temperature, wall temperature and velocity profiles are shown in Figures 3.27, 3.28 and 3.29. These profiles look promising, with the Reynolds numbers remaining essentially the same as the last run, as seen in Figure 3.30. The Prandtl number, a measure of diffusivity in a material, remains relatively constant throughout the profile (between 0.67 and 0.84), a result that seems reasonable considering the normal range for gases being 0.71.

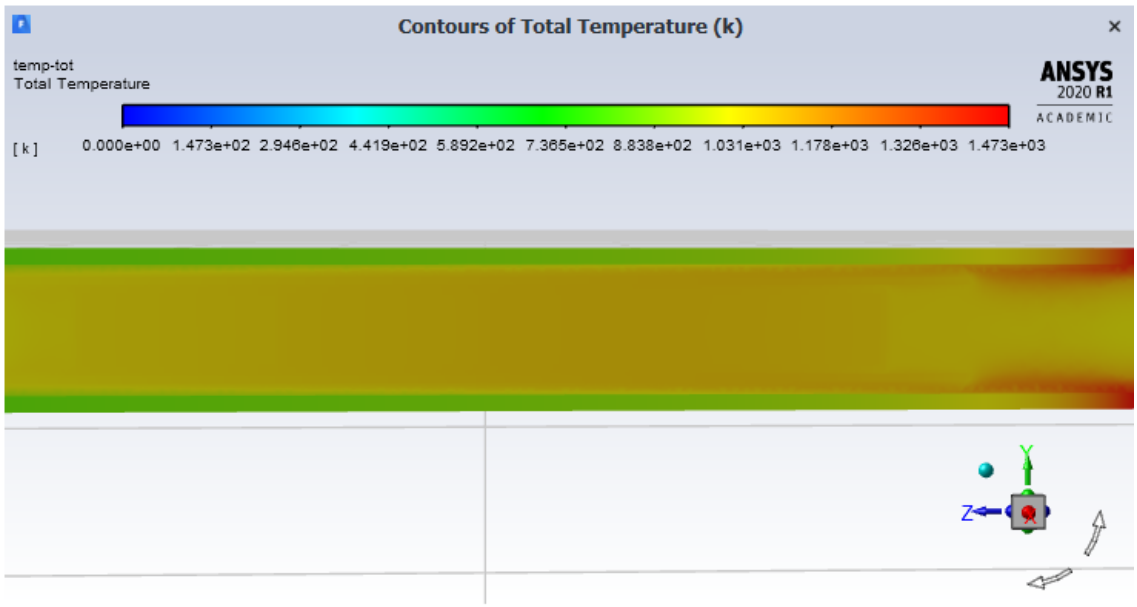

Figure 3.27: Temperature of test section, 40 mm ID & 50 mm OD, 1e8 W/m3 load

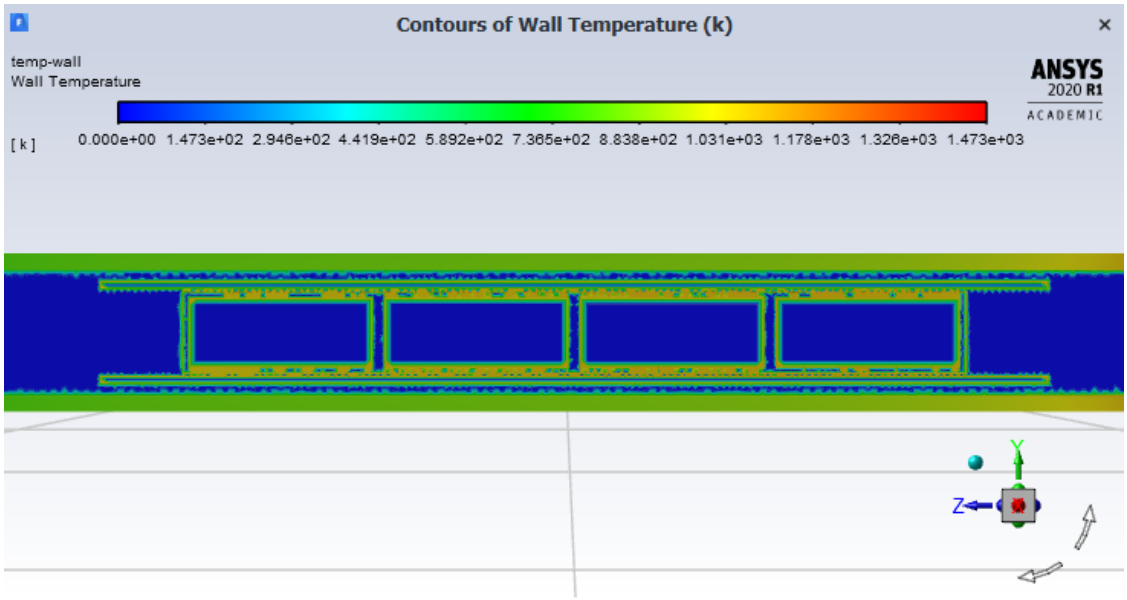

Figure 3.28: Wall temperature of test section, 40 mm ID & 50 mm OD, 1e8 W/m3 load

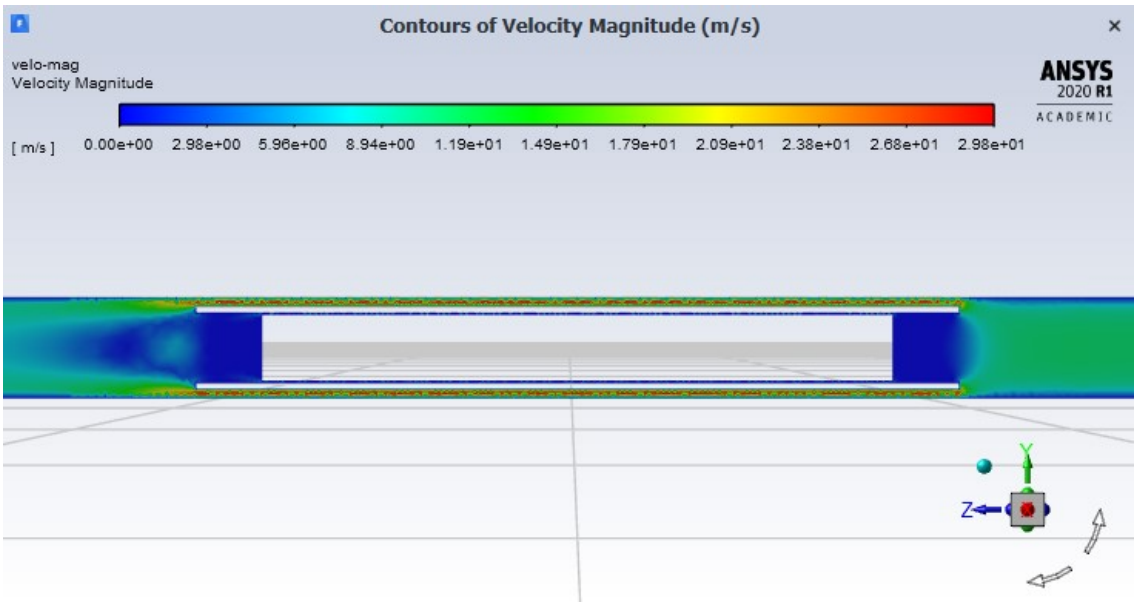

Figure 3.29: Velocity profile of test section, 40 mm ID & 50 mm OD, 1e8 W/m3 load

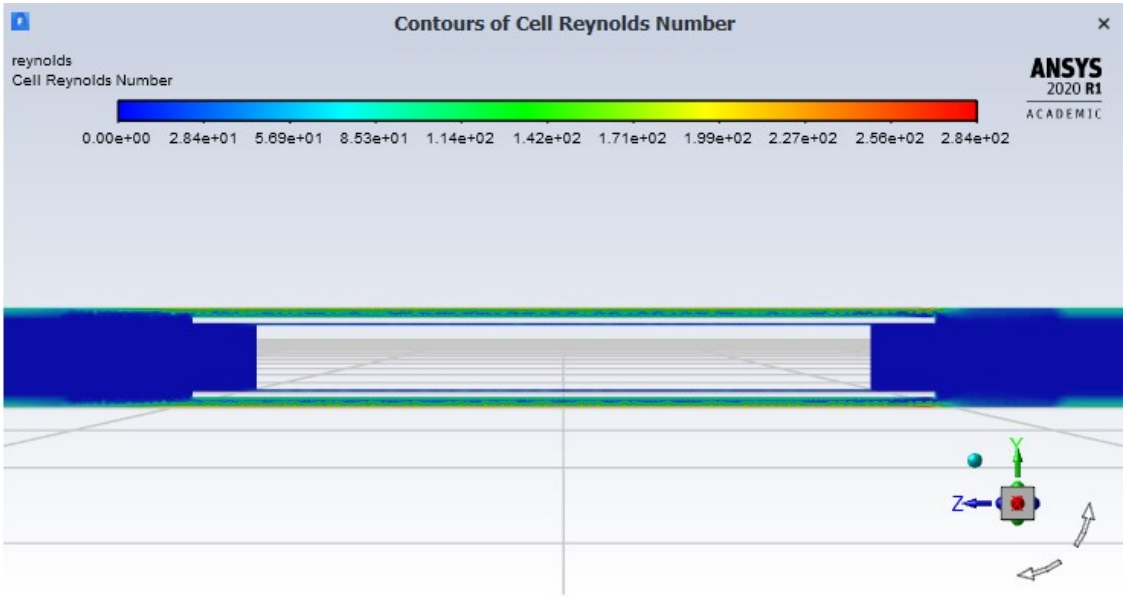

Figure 3.30: Reynolds number of test section, 40 mm ID & 50 mm OD, 1e8 W/m3 load

To try and reduce the outer wall temperature on the FeCrAl pipe, and incorporate more aspects of the physical BEARS loop design, the cooling section outer wall was given an increased heat transfer coefficient to simulate forced convection (30 W/(m^2-K)). There was not a significant change in temperature or wall temperature, so an extreme case was run where the convection on all sections was increased to 300 W/(m^2-K) to simulate a powerful fan blowing over all loop sections. The resulting temperature and wall temperature profiles are shown in Figures 3.31 and 3.32. The resulting temperature of all pipes was below 1200 °C, which is encouraging for the final loop when cooling the FeCrAl will be important for heat dissipation and extending the loop's performance.

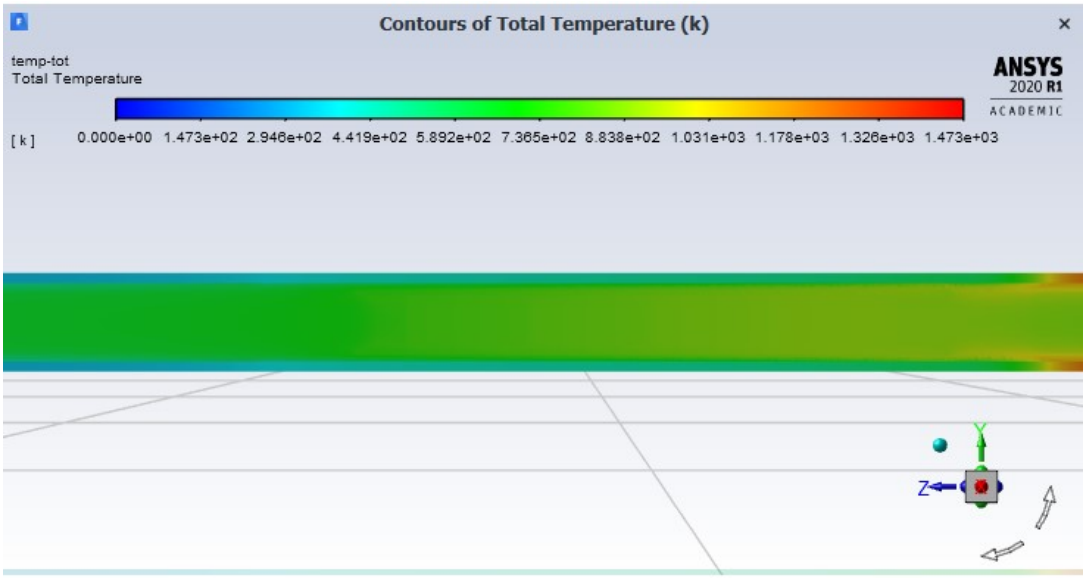

Figure 3.31: Forced convection temperature, 40 mm ID & 50 mm OD, 1e8 W/m3 load

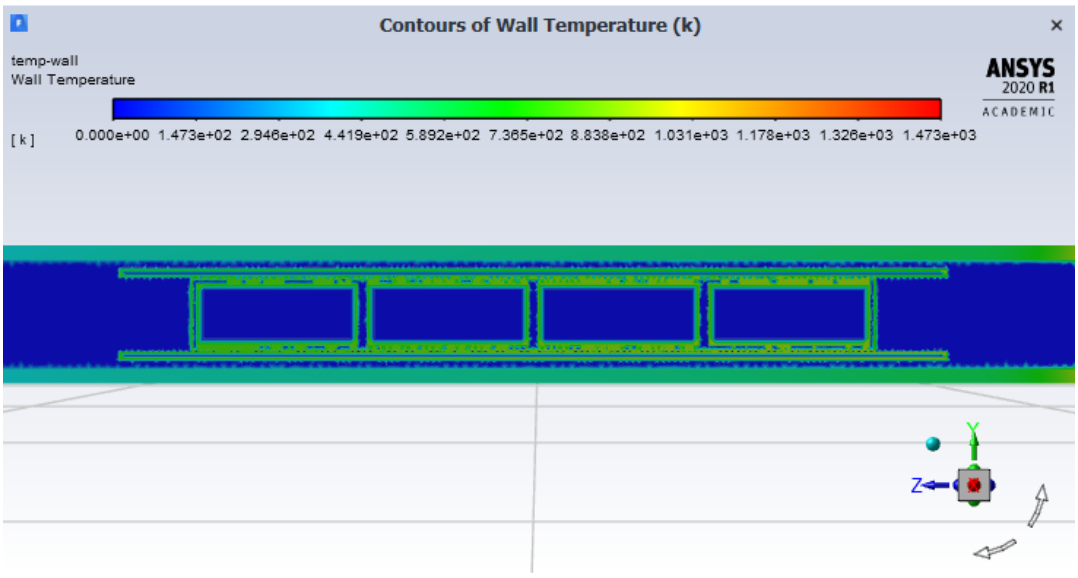

Figure 3.32: Forced convection wall temperature, 40 mm ID & 50 mm OD, 1e8 W/m3 load

Following these promising results for the 40 mm ID, 50 mm OD FeCrAl pipe, a selection of pipe cross section sizes and thicknesses were investigated, with the intent of selecting the pipe cross section with the least feasible material required. For the sake of brevity, the cases were only run for the SiC tie tube design. The smallest ID tried was 34 mm, giving a 2 mm gap between the ID and the tie tube shell. The largest pipe tried was a 70 mm ID, 80 mm OD, with larger cross section designs converging in less iterations than small designs. The wall temperature distribution of the test section gradually decreased as the pipe size increased, as can be seen in Figures 3.33 – 3.36. Because the Reynolds number profiles for the smaller sections still peaked below the threshold for transitioning to turbulent flow regimes, a 34 mm ID pipe size can be used with some confidence to decrease the amount of pipe material while maintaining general flow characteristics of larger designs. The Reynolds number profiles can be seen in Figures 3.37 – 3.40.

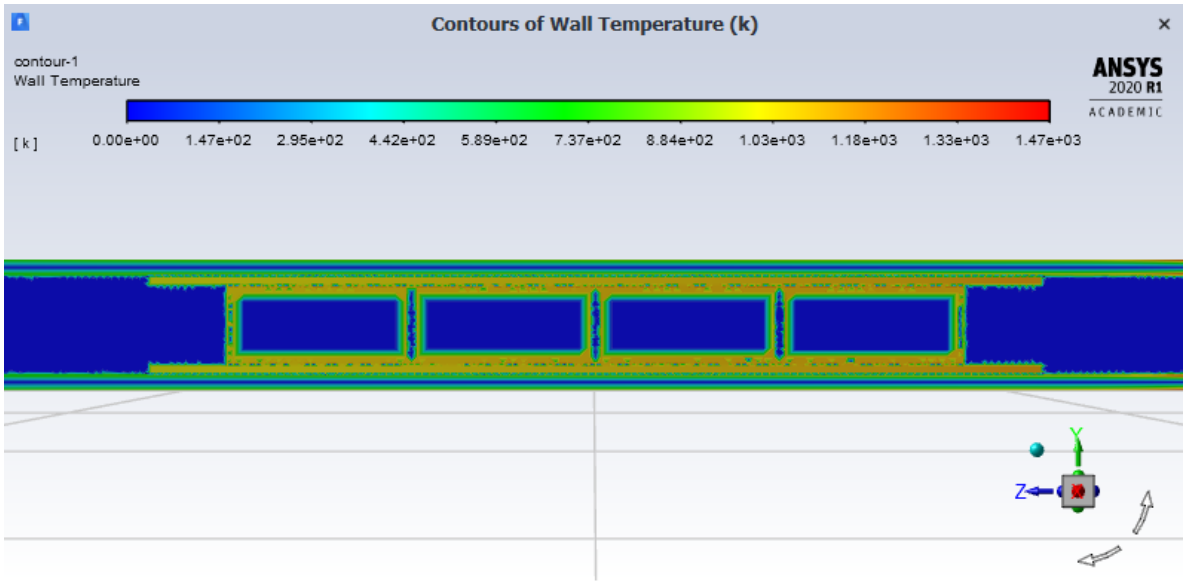

Figure 3.33: Wall temperature of test section, 34 mm ID & 44 mm OD, 1e8 W/m3 load

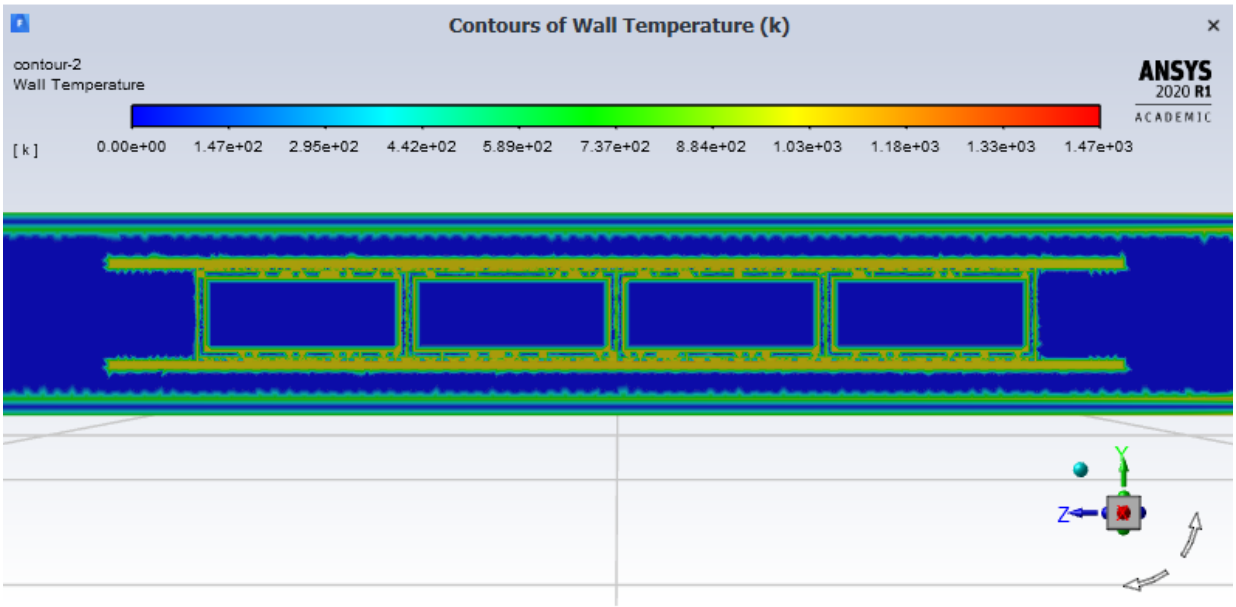

Figure 3.34: Wall temperature of test section, 50 mm ID & 60 mm OD, 1e8 W/m3 load

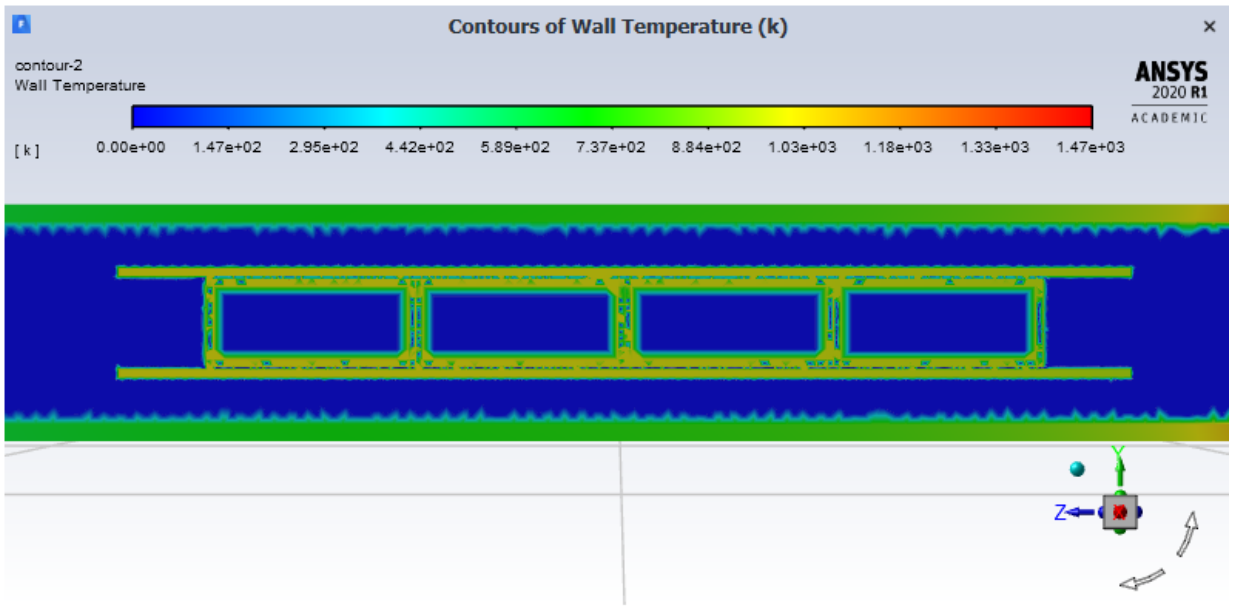

Figure 3.35: Wall temperature of test section, 60 mm ID & 70 mm OD, 1e8 W/m3 load

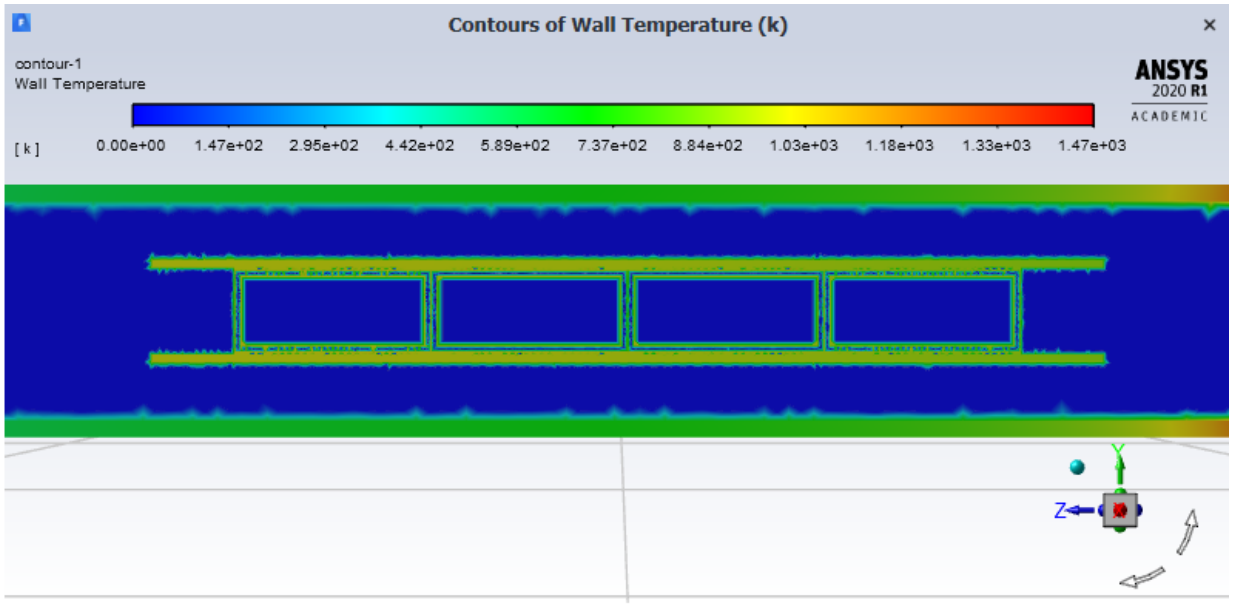

Figure 3.36: Wall temperature of test section, 70 mm ID & 80 mm OD, 1e8 W/m3 load

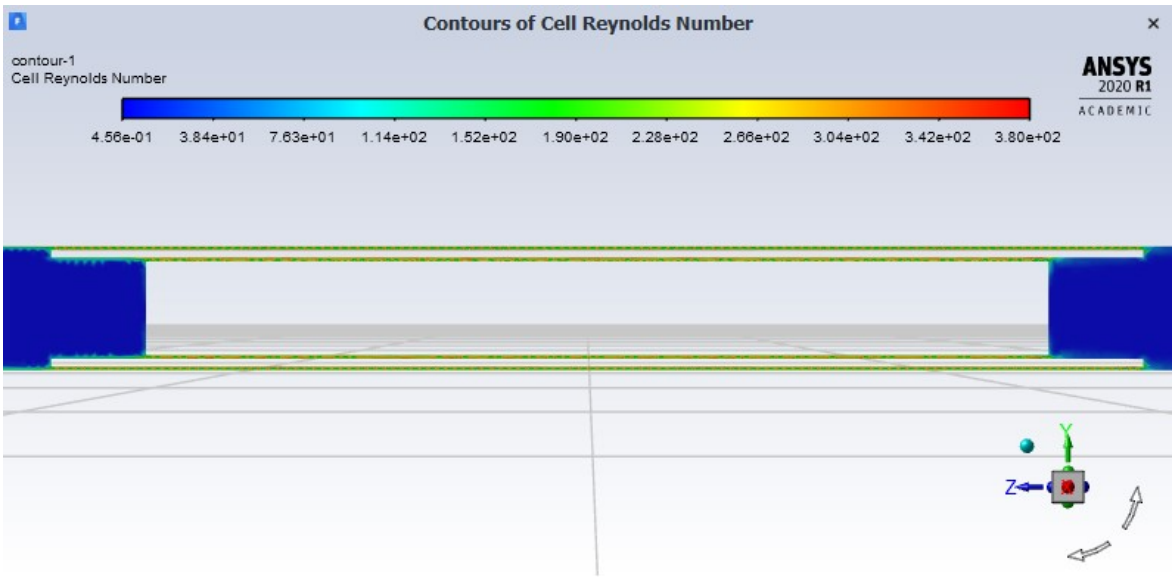

Figure 3.37: Reynolds number profile of test section, 34 mm ID & 44 mm OD, 1e8 W/m3 load

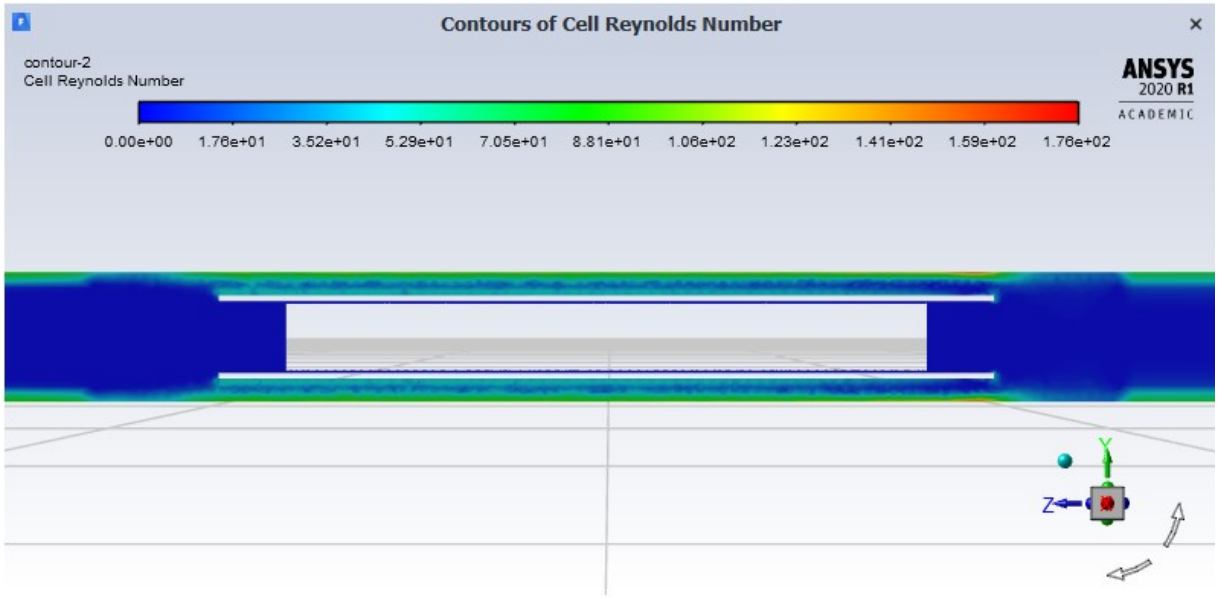

Figure 3.38: Reynolds number profile of test section, 50 mm ID & 60 mm OD, 1e8 W/m3 load

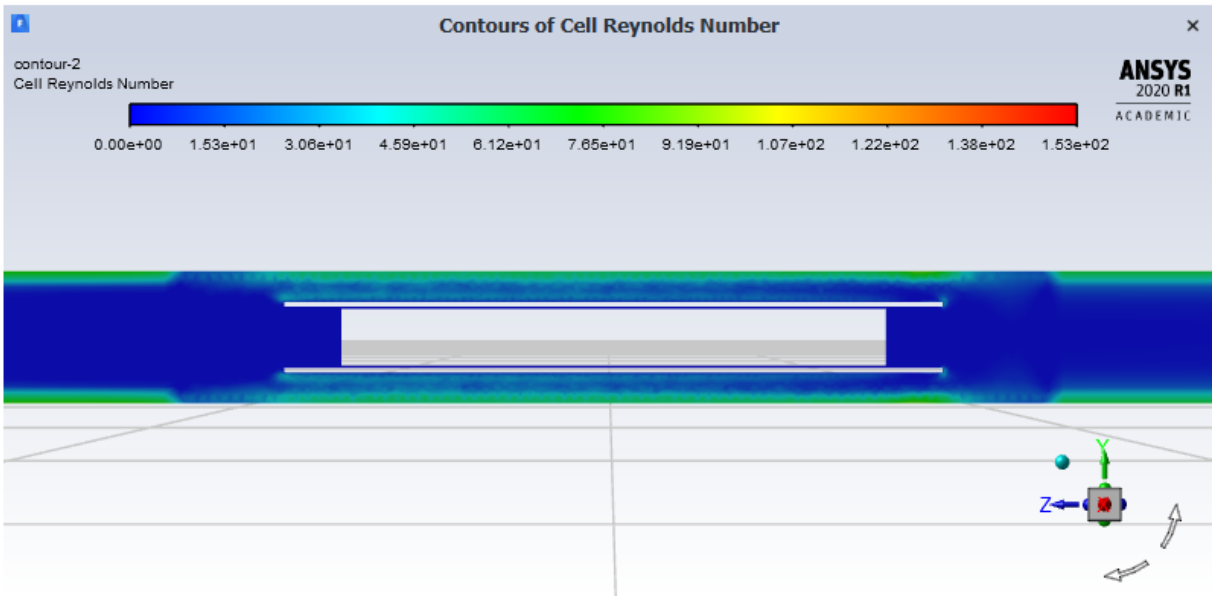

Figure 3.39: Reynolds number profile of test section, 60 mm ID & 70 mm OD, 1e8 W/m3 load

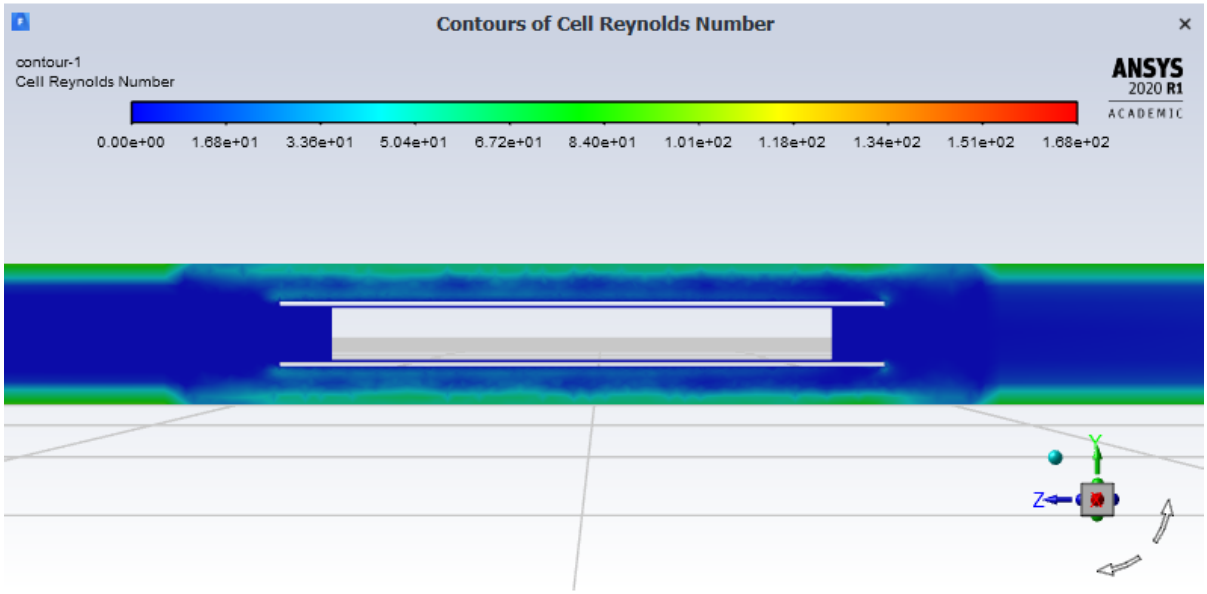

Figure 3.40: Reynolds number profile of test section, 70 mm ID & 80 mm OD, 1e8 W/m3 load

Decreasing FeCrAl thickness in the 40 mm ID case decreased tie tubes temperatures, likely because the volume of loop pipe was decreasing for a fixed 1e8 W/m^3 load, decreasing the energy imparted to the loop. Scaling by the volume of the heating section FeCrAl pipe, the power density required to produce equivalent results to the 40 mm ID, 50 mm OD pipe (~13 kW) is 2e8 W/m^3 in the 40 mm ID, 45 mm OD case and 4e8 W/m^3 in the 40 mm ID, 42.5 mm OD case. Scaling by these input power densities, the wall temperature distributions in the test section look similar for thinner FeCrAl pipes (Figures 3.41 and 3.42), suggesting less material could be used. To verify that mechanical stresses weren't increasing to concerning levels, the wall shear stresses are shown in Figures 3.43, 4.44 and 3.45. Fortunately, even for the thinnest case the max shear stress is orders of magnitude below the ultimate tensile strength for FeCrAl (6 MPa at 1200 °C) [30].

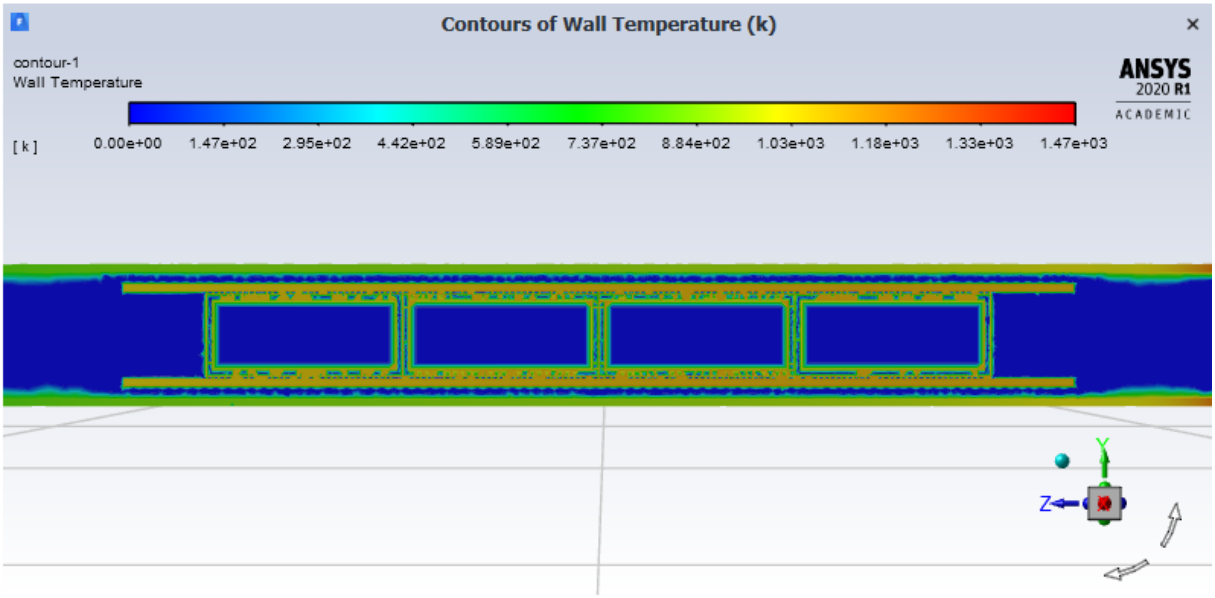

Figure 3.41: Wall temperature of test section, 40 mm ID & 45 mm OD, 2e8 W/m3 load

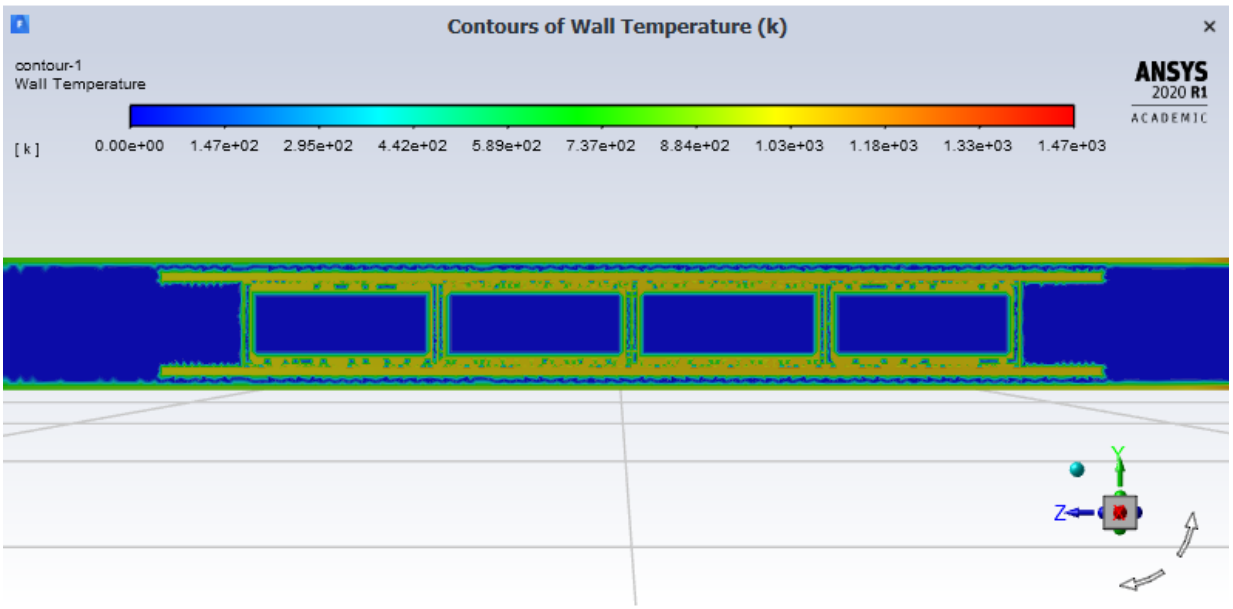

Figure 3.42: Wall temperature of test section, 40 mm ID & 42.5 mm OD, 4e8 W/m3 load

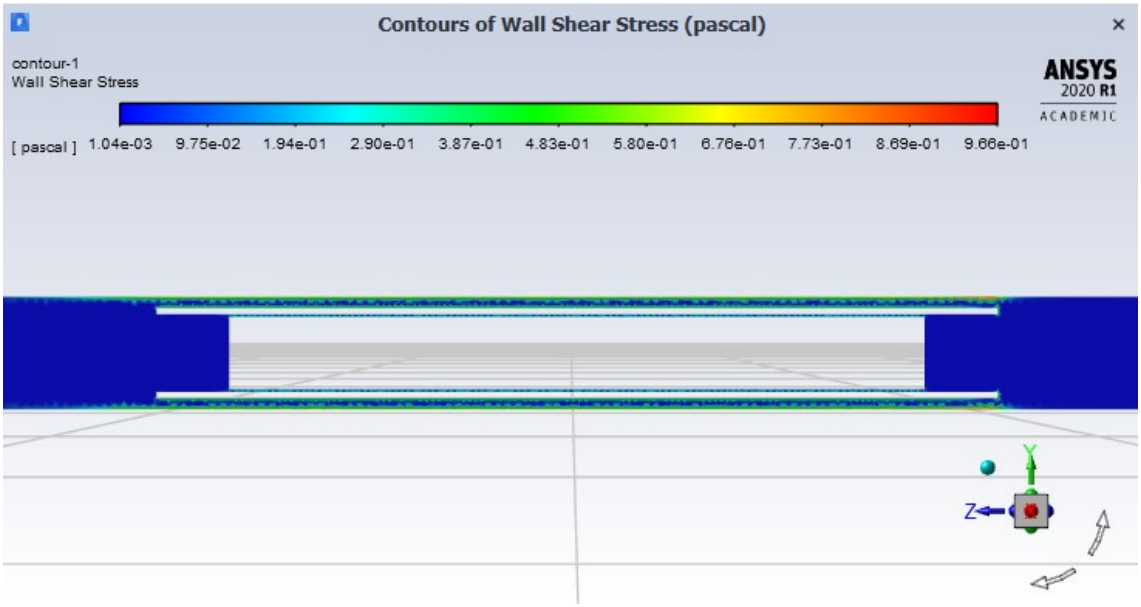

Figure 3.43: Wall shear stress of test section, 40 mm ID & 50 mm OD, 1e8 W/m3 load

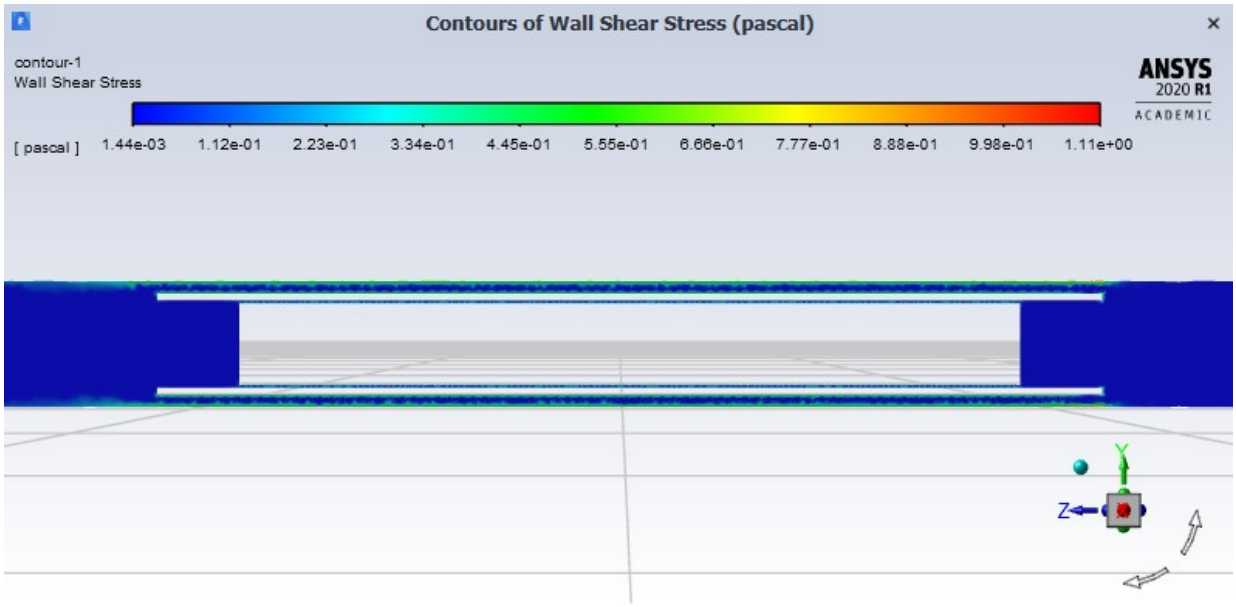

Figure 3.44: Wall shear stress of test section, 40 mm ID & 45 mm OD, 2e8 W/m3 load

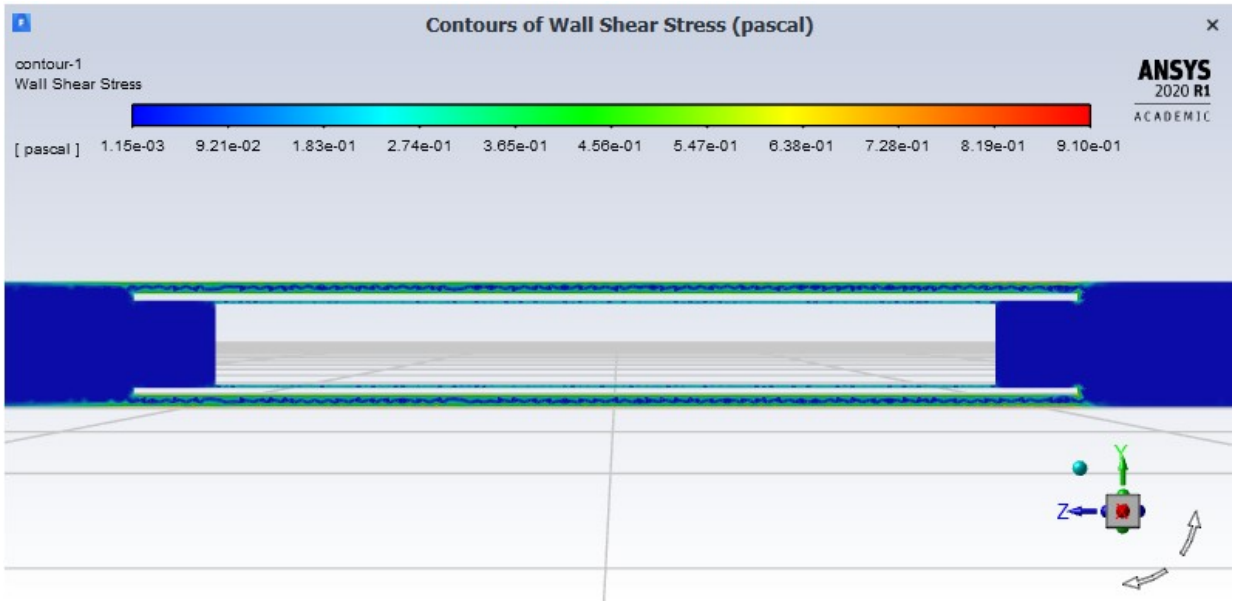

Figure 3.45: Wall shear stress of test section, 40 mm ID & 42.5 mm OD, 4e8 W/m3 load

As an additional measure to simulate the real conditions of the BEARS loop, a Fluent run with a high vacuum environment outside the test loop was conducted on the 40 mm ID, 50 mm OD linear loop design with the SiC/SiC tie tube. To do this, the convection of the outer FeCrAl walls was set to 0 to mimic the minimal heat transfer in a vacuum environment. The resulting temperature, wall temperature, velocity and Reynolds number profiles are shown in Figures 3.46 – 3.49. These profiles are very similar to Figures 3.27 – 3.30 in the atmospheric environment case, which is a promising result for the thermal performance of the test loop.

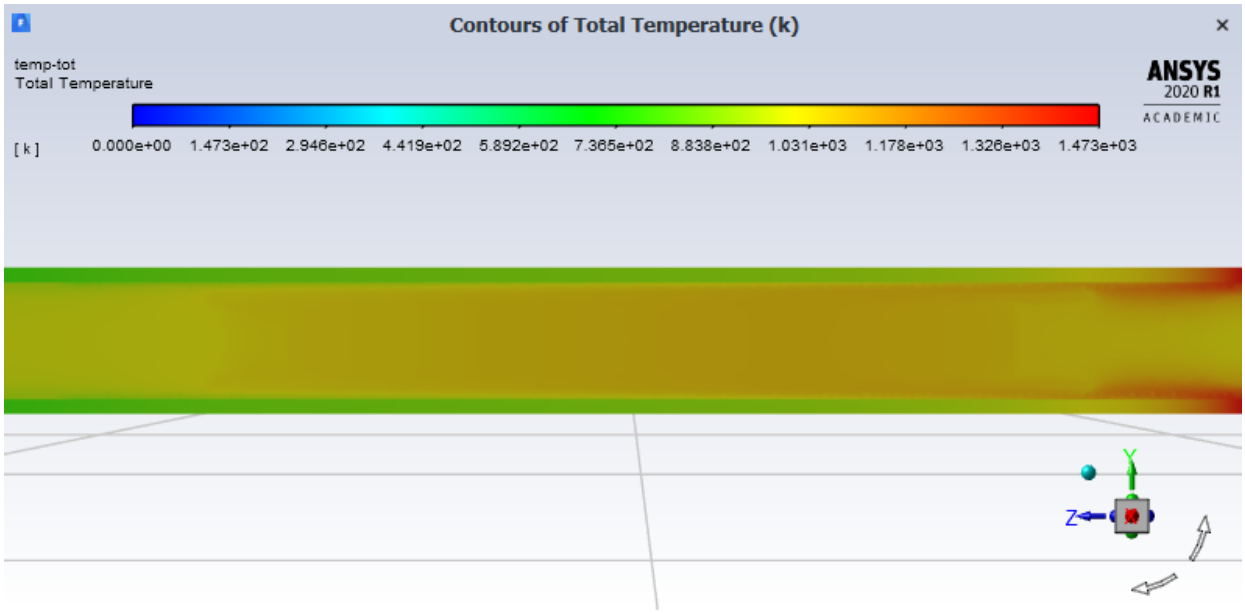

Figure 3.46: High vacuum temperature of test section, 40 mm ID & 50 mm OD

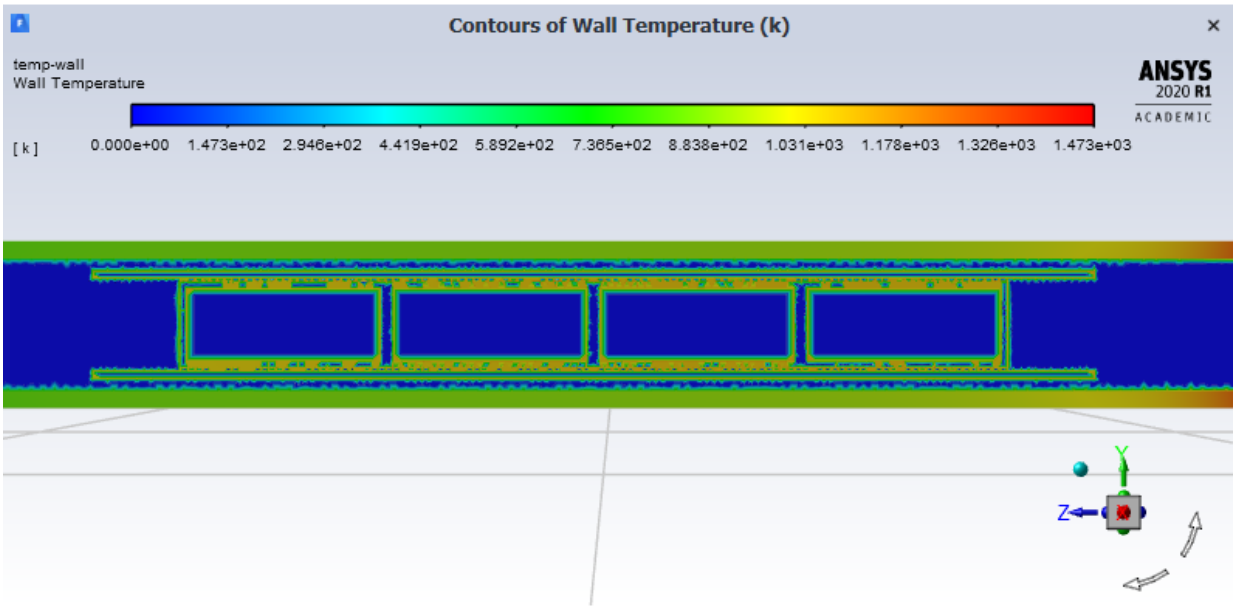

Figure 3.47: High vacuum wall temperature of test section, 40 mm ID & 50 mm OD

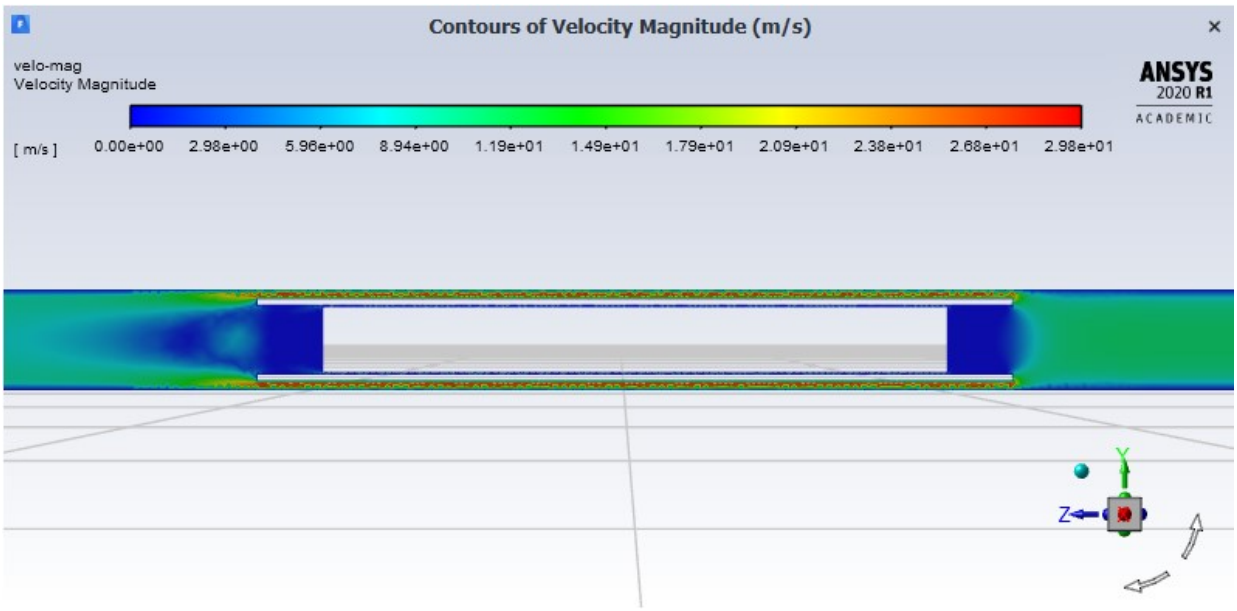

Figure 3.48: High vacuum velocity profile of test section, 40 mm ID & 50 mm OD

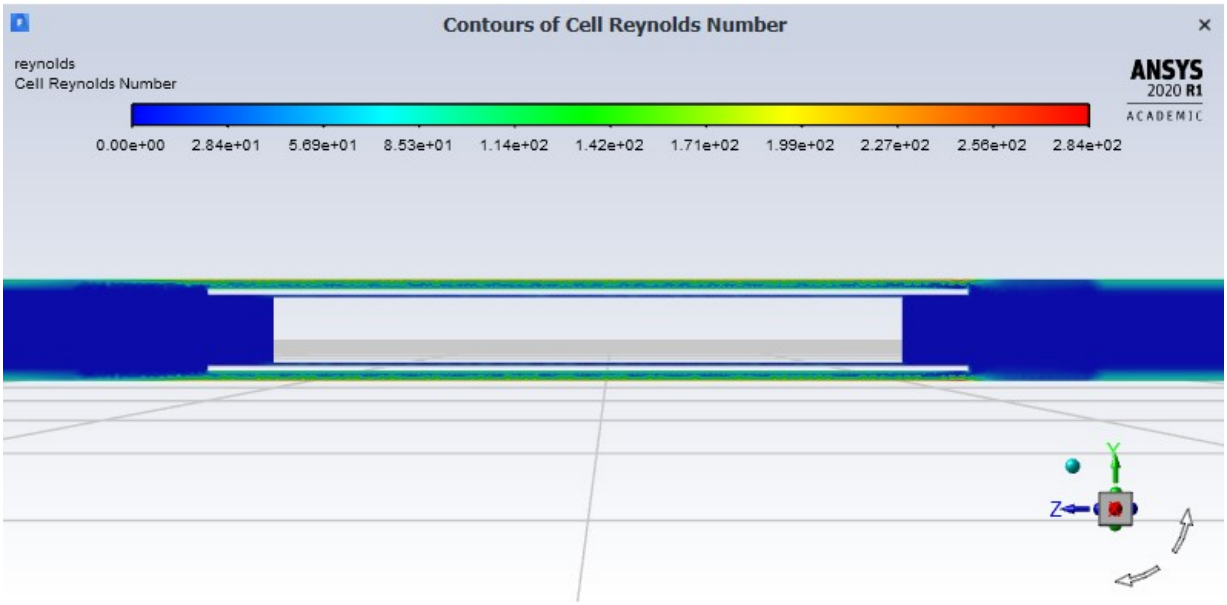

Figure 3.49: High vacuum Reynolds numbers of test section, 40 mm ID & 50 mm OD

As a concluding note, the profiles of additional physical quantities not mentioned here (Density, Effective Viscosity, etc.) can be found in the Appendix for the 40 mm ID, 50 mm OD SiC/SiC tie tube case. This case was run with a 1e8 W/m^3 load on the heating section of FeCrAl pipe, 6 W/(m^2-K) convection on the heating and test sections and 30 W/(m^2-K) convection on the cooling section. The case was initialized with an inlet MFR of 1 g/s and 12 MPa and an outlet of 12 MPa. With the test cases run, the results as a whole will now be discussed.

3.4 Discussion of Results

In both the SST and CFD models, FeCrAl showed itself to be a capable loop pipe material, remaining below its melting temperature for all runs undertaken here. While the utility of the SST simulations in general may have been limited by its lack of flowing hydrogen, it was a useful tool for predicting the locations of thermal gradients in the test section, and in better understanding the limitations of the Student version of ANSYS. While there is no doubt error due to mesh sizing in all of the simulations undertaken, the results are generally useful in predicting the orders of magnitude for the temperature and velocity distributions of the flow and solid elements.

While the TZM tie tube in Figure 3.14 has a small thermal gradient compared to the SiC/SiC tube in Figure 3.13, its lower peak temperature is probably a suggestion that it does not in fact have better heat transfer properties than the SiC/SiC tie tube. It would be worthwhile to do side-by-side comparisons of both tie tube designs in the Fluent simulations to study these differences in greater detail, since this had to be omitted due to time constraints. There are additional factors that would affect the selection of one material over the other, too, including cost and ease of fabrication, and plasma-material interactions. The latter of the three previous factors can and will be examined further in the BEARS loop experiment.

For the most commonly used test loop cross section, 40 mm ID and 50 mm OD, the power density for the heat flux imparted on the heating section pipe to provide a test section hydrogen inlet temperature of ~1200 °C was ~13 kW. This unrealistically assumes the heat load is evenly distributed to the entire surface and 800 mm length. This means the actual power requirements for

the heat source may be higher depending on the geometry of the contact surface area, and the efficacy of conduction heat transfer from the heat source to the FeCrAl.

While not covered due to time constraints, it is also important to consider the effects bends in the test loop will have on the hydrogen plasma. Even if the walls are perfectly smooth, the redirection of fluid may be be important in altering the velocity profile and flow behavior between sections. The BEARS loop should have the advantage of avoiding large eddy's and other dissipative structures however, since for all cases tested the flow remained comfortably within the laminar flow regime. The simulation's ability to accurately output results for pipe flow will be discussed more in Chapter 4.

The relative lack of effect high vacuum conditions had on the test loop's temperature profiles suggests the BEARS loop design may be able to forgo imposing vacuum conditions in the Lexan box surrounding the loop. While the effect should be investigated further in either simulations/experiment, this would save some expense and complexity in the initial BEARS loop experiments. The simulation of high vacuum conditions may also have been inaccurate, since the loop simulated was open on both sides. This may make all pressure conditions imposed on either side nonrepresentative compared to a full sealed loop design. Future Fluent simulation work may be able to predict the effects of high vacuum conditions more accurately for the tie tube and flowing hydrogen.

It may also be practical to use the high temperature fan planned for the test loop to cool the entire loop, rather than just a cooling section of pipe. As the results for forced convection indicated, the thermal gradient in the FeCrAl was larger when the convection was greater on one portion of the loop, so in practice this may lead to premature damage to the test loop. The fan's

cooling ability may also have limitations based on the lack of gas density within the high vacuum environment. A potential solution would be to have the cooling section extend through penetrations in the Lexan to the outside environment, but this would not mitigate the thermal gradient issue. More examination of this issue is needed to produce a solution that effectively cools the test loop without undue thermal stresses on the loop's pipe.

The use of black body emissivity (emissivity of 1) is an idealization, and the true emissivity of a FeCrAl alloy is likely less than this to the point where the FeCrAl temperature profiles would be higher than those found in these simulations. This along with the potential difficulty in convective cooling will require a zoomed-in follow-up of simulations to ensure the FeCrAl remains under its melting temperature for all heat loadings.

As a final note, the simulations of different sizes and thicknesses of FeCrAl pipe showed a preliminary preference for small cross-sectional areas and smaller thicknesses, with minimal wall shear stresses and comparable temperature and velocity profiles. There may be additional factors that would require larger pipe thicknesses and sizes however: cost, ease of manufacture, lead time, and the ability to test larger tie tube designs to name a few. At present, cost and ease of manufacture are anticipated to have the greatest effect on the final pipe design chosen for the BEARS loop.

Chapter 4: SIMULATION VALIDATION

The Fluent CFD model developed for analysis of the BEARS hydrogen test loop design is essentially a pipe flow problem, which has an extensive bulk of work in the literature of CFD simulation. The specific problems most applicable to the test loop problem is a steady laminar pipe flow problem with heat transfer. In order to compare against test problems most effectively, the Fluent test loop model with a 50 mm ID and 60 mm OD pipe was modified to remove the tie tube from the test section, making a problem with only FeCrAl and hydrogen. In order to minimize errors due to mesh size and element skewness, the mesh order was changed from linear to quadratic and the element size was reduced to 5e-03 m. Also, the edges of the FeCrAl pipe were sized using 40 hard divisions. The resulting mesh is shown in Figure 4.1 for the test section, where the highest skew elements appear.

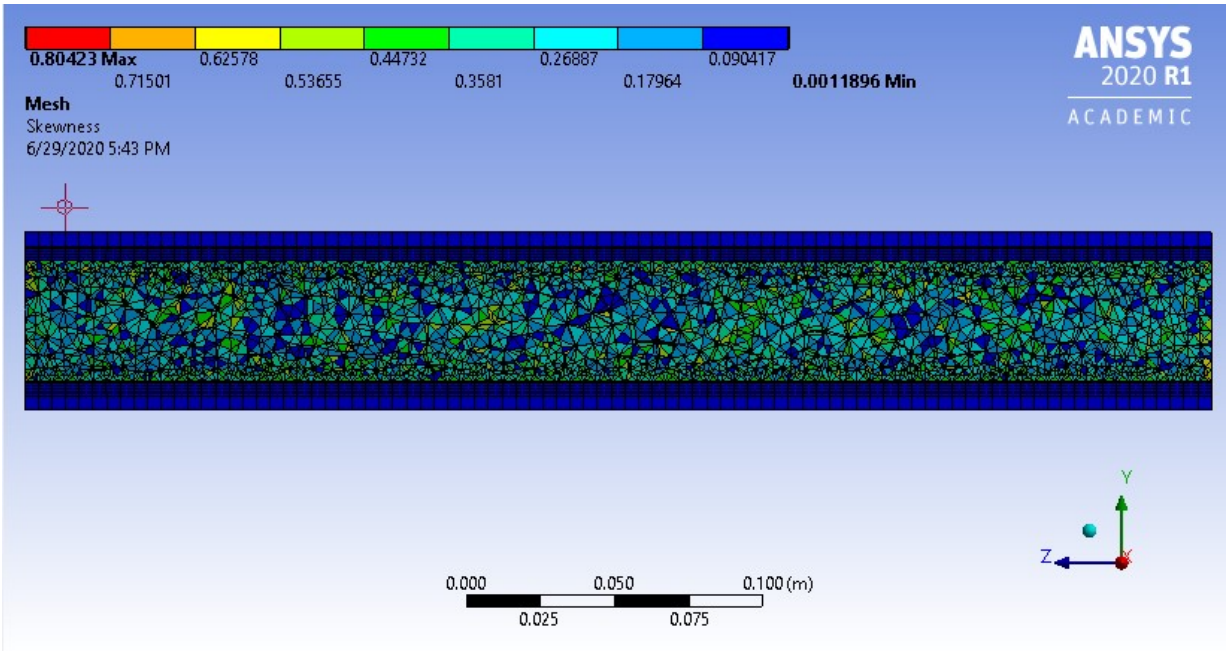

Figure 4.1: Test problem mesh skewness of test section, 50 mm ID & 60 mm OD

The test problem was initialized in a similar fashion to the previously done Fluent CFD runs, with a 1e8 W/m^3 heat flux applied to the heating section, 6 W/(m^2-K) convection coefficients applied to the heating and test sections and 30 W/(m^2-K) applied to the cooling section. The inlet was set to 1 g/s MFR and 12 MPa gauge pressure, and the outlet to 12 MPa gauge pressure. The problem was hybrid initialized and run for 200 iterations, converging to 1e-04 in all residuals after 93 iterations.

The YZ-planar results from this simulation were then exported to Excel for post-processing in order to compare with the literature, where fluid dynamic variables are often made dimensionless in order to make them easier to compare across a wide variety of problem sizes and flow behaviors. Of the papers reviewed for comparison, Patel & Mead [40] seemed the most appropriate for a velocity profile comparison. Their figure comparing dimensionless distance from the centerline to the pipe wall versus the dimensionless flow velocity is shown as Figure 4.2. Their pipe is ½ inch in diameter, which is smaller (12.7 mm) than the test problem generated but still within an order of magnitude. Importantly, it illustrates a Parabolic Law that describes the relationship between velocity and radial position in the pipe for fully laminar flow. The data exported from the test problem run earlier is plotted using Excel in Figure 4.3 and compares favorably to Figure 4.2. For the “U” velocity, the velocity in the pipe axial (Z) direction was used, and for “Y” the Y position data was used. In order to visualize the data more clearly, only the first 5000 data points were used in the plot in Figure 4.3. The test problem data is centered about 0 rather than 1 in Patel & Mead, but the shape indicates similar flow behavior to their gathered data.

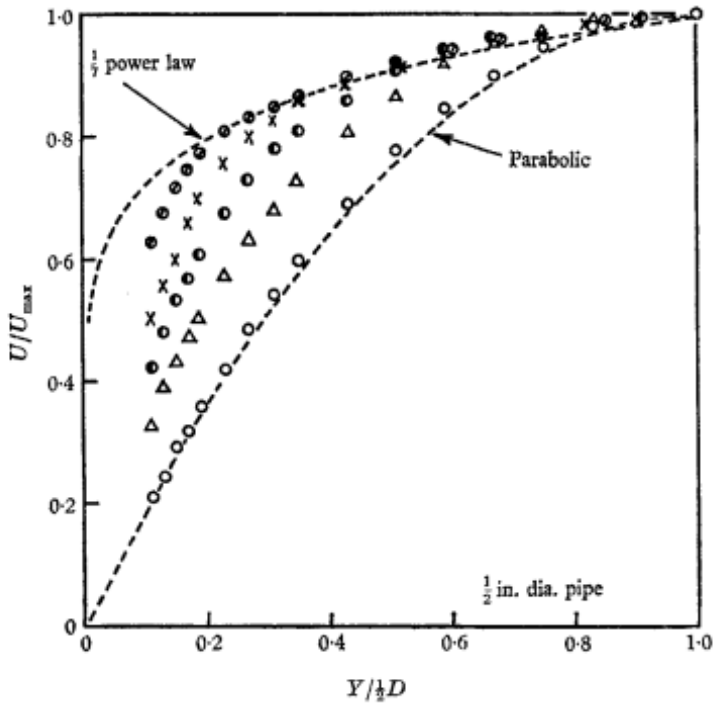

FIGURE 3. Velocity profiles in pipes. Values of Re in the $\frac{1}{4}$ in. pipe: ○, 1400; △, 2015; ◐, 2440; ×, 2680; ⊘, 3070; +, 4060. Values of Re in the $\frac{1}{2}$ in. pipe: ○, 1740; △, 2440; ◐, 2615; ×, 2975; ⊘, 4430.

Figure 4.2: Velocity profile data from Patel & Mead [40]

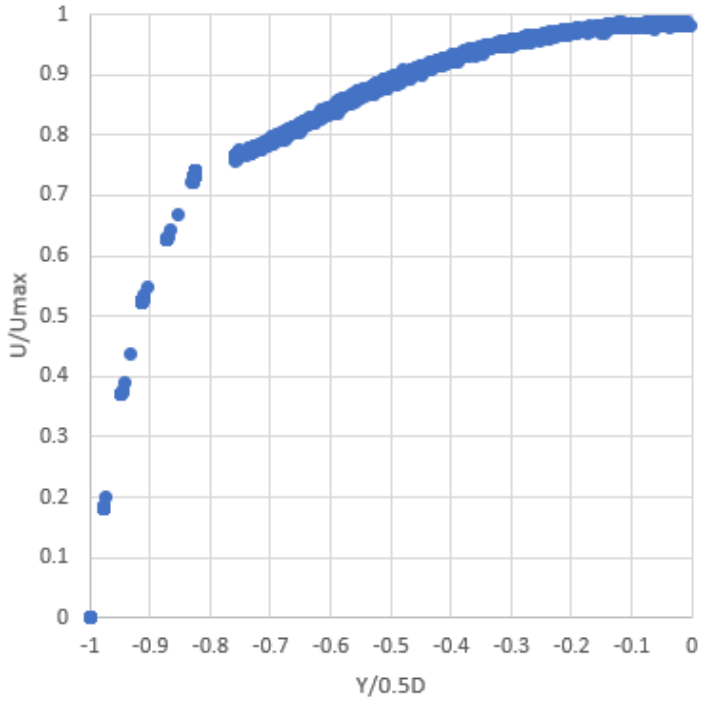

Figure 4.3: Velocity profile of test problem

While more difficult to find a point of comparison, the heating profile was also compared to the literature, using the Nusselt number. The Nusselt number is a ratio of convective versus conductive heat transfer, and it is plotted versus the normalized axial (Z) direction for the test problem in Figure 4.4. While not directly comparable, Jiang et al. present results with similar increasing and decreasing behavior for heated CO_2 rising through a pipe at 8.6 MPa, 0.12 kg/h and a Reynolds number of 2900 [41]. Their figure is shown for comparison in Figure 4.5.

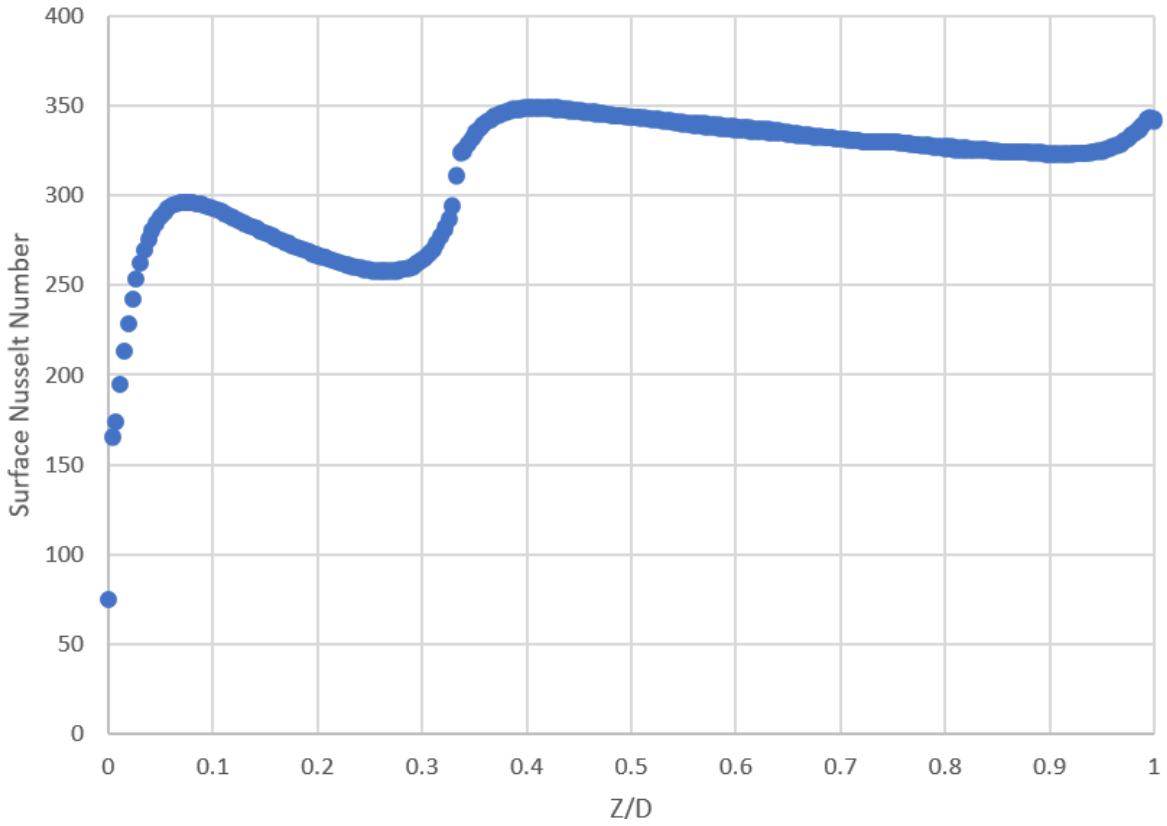

Figure 4.4: Nusselt number profile of test problem

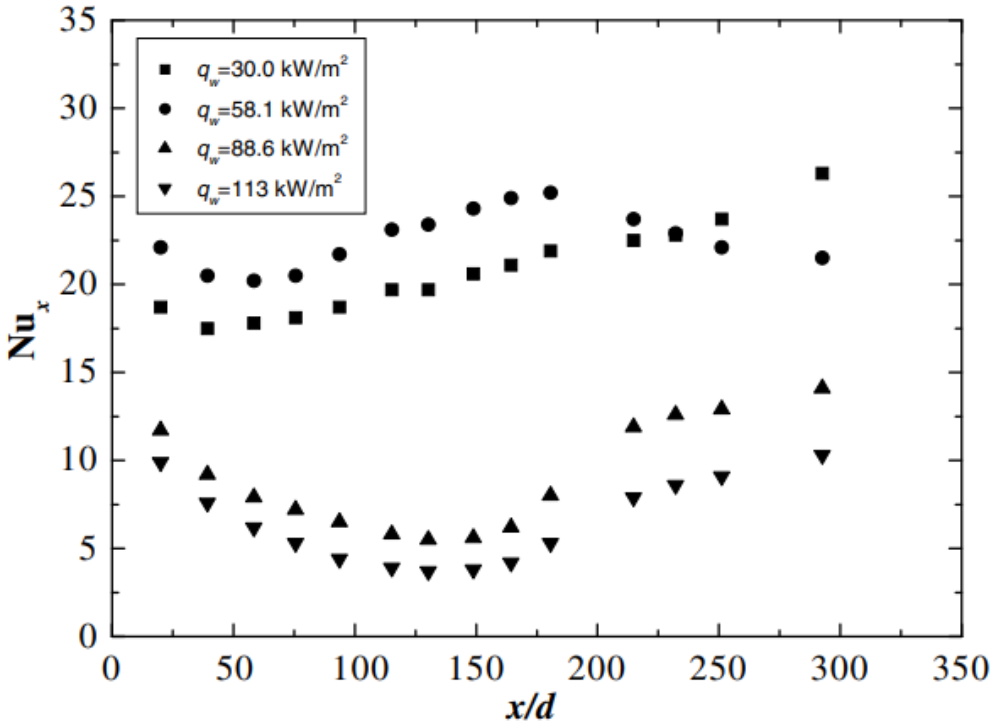

Figure 4.5: Nusselt number profile from Jiang et al. [41]

The exact behavior of Figure 4.4 is likely different than Figure 4.5 due to the much higher heat flux imparted to the test problem, and lack of uniform temperatures and convection on the pipe surfaces. Despite the lack of robust comparisons to the literature, the Fluent simulation package is well verified and validated against test flow problems, and any discrepancies that arise in problem comparisons arise only because of the dissimilarities in problem setup and inputs.

Additionally, problem comparison was made difficult by a lack of parameters available in the fluid, such as heat flux and heat transfer coefficient. Because of this, only surface values from the pipes could be used for thermal comparisons and deriving relevant thermal parameters from given fluid data proved difficult. In future studies, more research will be needed in order to more accurately obtain similarity parameters from the fluid variables available in Fluent Post-Processing, and facilitate better matching with test problems from the literature.

Despite the difficulties with thermal variable processing, the velocity profile is nicely correlated to laminar profiles described in theory and in experiment, and the model developed for these test loop simulations can be relied upon for preliminary temperature and velocity distributions that will inform the construction of the final test apparatus.

Chapter 5: CONCLUSIONS & FUTURE WORK

The Nuclear Thermal Rocket provides a lot of promise for making manned missions to Mars less costly and time-consuming, saving the astronauts and payload from greater exposures to space radiation. In order to aid NASA and Ultra Safe Nuclear Corporation in their development of an NTR engine, the BEARS lab at Penn State is developing a hot hydrogen test loop to expose tie tube elements to hydrogen at 1200 °C in the initial design, and eventually 2700 °C with a second test loop design, in order to obtain materials data and characterize hydrogen embrittlement and attack on the tie tubes, informing the design of a better tie tube and NTR design. To produce comparable hydrogen conditions to reference NTR designs, the BEARS loop will impose 12 MPa of pressure and a mass flow rate of 1 g/s on the hydrogen. The loop's design will need to incorporate heating elements that can produce the equivalent of 13 kW over the entire heating section pipe's surface, and the cooling fan will need to supply forced convection to prevent large thermal gradients.

The Steady-State Thermal and ANSYS Fluent simulations modeling the hydrogen, FeCrAl pipe and tie tube designs confirmed the FeCrAl pipe's ability to withstand the heat loads imposed by the test loop, and the flow's largely laminar behavior at operating conditions. The FeCrAl pipe was also able to withstand loop operating conditions with smaller pipe thicknesses and cross sections, allowing potential cost and manufacturing savings. The test loop's flow characteristics showed little change upon vacuum conditions being imposed outside, but this could adversely affect the fan's ability to produce forced convection. Future work will focus on the implementation of feasible heating and cooling systems, and the effects of recirculating pumps on hydrogen flow behavior, in order to bring the BEARS loop closer to construction.

REFERENCES

[1] Drake, Bret G. et al., "Human Exploration of Mars: Design Reference Architecture 5.0", *National Aeronautics and Space Administration*, NASA/SP-2009-566, **2009**. https://www.nasa.gov/exploration/library/esmd_documents.html

[2] Nam, Seung H. et al., "Innovative concept for an ultra-small nuclear thermal rocket utilizing a new moderated reactor." *Nucl. Eng. Technol.*, Vol. 47, **2015**, pp. 678-699. https://doi.org/10.1016/j.net.2015.06.003

[3] Joyner II, C. Russell et al., "LEU NTP Engine System Trades and Mission Options", *Nuclear Technology*, **2020**. https://doi.org/10.1080/00295450.2019.1706982

[4] Sutton, George P. & Biblarz, Oscar, "Rocket Propulsion Elements: An Introduction to the Engineering of Rockets", *John Wiley & Sons*, New York, NY, 7th ed., **2001**.

[5] Casani, John R. et al., "Enabling a New Generation of Outer Solar System Missions: Engineering Design Studies for Nuclear Electric Propulsion", *A White Paper in Response to the Planetary Science and Astrobiology Decadal Survey 2023-2032 Call*, **2020**. http://hdl.handle.net/2014/47277

[6] Hrbud, Ivana et al., "End-to-End Demonstrator of the Safe Affordable Fission Engine (SAFE) 30: Power Conversion and Ion Engine Operation", *AIP Conference Proceedings*, Vol. 608, **2002**. https://doi.org/10.1063/1.1449818

[7] Oleson, Steven et al., "A Kuiper Belt Object Orbiter Enabled By 10kW Kilopower Electric Propulsion", *AIAA Propulsion and Energy Forum*, **2019**. https://doi.org/10.2514/6.2019-3963

[8] Rice, C. M. & Esselman, W. H., "NERVA Development Status" *The 4th Space Congress® Proceedings*, 3, **1967**. https://commons.erau.edu/space-congress-proceedings/proceedings-1967-4th/session-18/3/

[9] Emrich, William, Jr., "Principles of Nuclear Rocket Propulsion", *Butterworth-Heinemann*, Amsterdam, The Netherlands, **2016**.

[10] Corrington, L. C., "The Nuclear Rocket Program – Its status and plans", *AIAA 4th Propulsion Joint Specialist Conference*, **1968**. https://doi.org/10.2514/6.1968-610

[11] Robbins, W. H. & Finger, H. B. "An Historical Perspective of the NERVA Nuclear Rocket Engine Technology Program", *Conference on Advanced SEI Technologies*, **1991**. https://doi.org/10.2514/6.1991-3451

[12] Nam, Seung H. et al., "Preliminary conceptual design of a new moderated reactor utilizing an LEU fuel for space nuclear thermal propulsion." *Progress in Nuclear Energy*, Vol. 91, **2016**, pp. 183-207. https://dx.doi.org/10.1016/j.pnucene.2016.02.008

[13] Howe, Steven D. et al., "Safe Testing of Nuclear Rockets", *Journal of Propulsion and Power*, Vol. 17, No. 3, **2001**. https://doi.org/10.2514/2.5808

[14] Schmidt, George R. et al., "Radioisotope Power: A Key Technology for Deep Space Exploration", *AIAA 6th International Energy Conversion Engineering Conference*, **2008**. https://doi.org/10.2514/6.2008-5640

[15] Morris, Robert N. et al., "Post-Irradiation Examination of 237-Np Targets for 238-Pu Production", *Nuclear and Emerging Technologies for Space Conference*, **2015**. https://www.osti.gov/biblio/1185863

[16] Holman, R. R. & Pierce, B. L., "Development of NERVA reactor for Space Nuclear Propulsion", *AIAA 22nd Joint Propulsion Conference*, **1986**. https://doi.org/10.2514/6.1986-1582

[17] Demyanenko, Yuri et al., "Ground Test Demonstrator Engine Boost Turbopumps Design and Development", *AIAA 41st Joint Propulsion Conference*, Session LP-9, **2005**. https://doi.org/10.2514/6.2005-3945

[18] Gibson, Marc A. et al., "NASA's Kilopower Reactor Development and the Path to Higher Power Missions", *IEEE Aerospace Conference*, **2017**. https://ntrs.nasa.gov/search.jsp?R=20170002010

[19] Venneri, Paolo & Kim, Yonghee, "Feasibility of Low Enriched Uranium Fuel for Space Nuclear Propulsion", *Transactions of the Korean Nuclear Society Spring Meeting*, **2013**. https://www.kns.org/presentation/lists/sc_year_season/2013-Spring/sc_field/pp_author/sc_word/venneri

[20] Patel, Vishal et at., "Comparing Low Enriched Fuel to Highly Enriched Fuel for use in Nuclear Thermal Propulsion Systems", *AIAA 52nd Joint Propulsion Conference*, 4887, **2016**. https://doi.org/10.2514/6.2016-4887

[21] Gray, Leven B. et al., "Perspectives of The Interagency Nuclear Safety Review Panel (INSRP) on future nuclear powered space missions", *AIP Conference Proceedings*, Vol. 271, pp. 429-433, **1993**. https://doi.org/10.1063/1.43183

[22] Houts, M. G. et al., "Nuclear Thermal Propulsion for Advanced Space Exploration", *Space Propulsion*, M12-1753, **2012**. https://ntrs.nasa.gov/search.jsp?R=20120014974

[23] Schoenfeld, Michael, "Nuclear Thermal Rocket Element Environmental Simulator (NTREES)", *Space Nuclear System Forum*, M09-0463, **2009**. https://ntrs.nasa.gov/archive/nasa/casi.ntrs.nasa.gov/20090025984.pdf

[24] Bradley, David E. et al., "Low Cost Nuclear Thermal Rocket Cermet Fuel Element Environment Testing (CFEET)", *JANNAF 5th Spacecraft Propulsion Subcommittee Meeting*, **2011**. https://ntrs.nasa.gov/search.jsp?R=20120002970

[25] Benensky, Kelsa M. et al., "Operational Characterization and Testing of NASA MSFC's Compact Fuel Element Environmental Test (CFEET)", *ANS Nuclear & Emerging Technologies for Space (NETS) conference*, **2018**. https://www.researchgate.net/publication/324164525_Operational_Characterization_and_Testing_of_NASA_MSFC'S_Compact_Fuel_Element_Environmental_Test_CFEET

[26] Li, Y. et al., "Fracture behavior of tungsten-based composites exposed to steady-state/transient hydrogen plasma", *Nucl. Fusion*, Vol. 60, **2020**. https://doi.org/10.1088/1741-4326/ab77e7

[27] Rivkin, C. et al., "Hydrogen Technologies Safety Guide" *National Renewable Energy Laboratory*, TP-5400-60948, **2015**. https://www.nrel.gov/docs/fy15osti/60948.pdf

[28] SABIC Innovative Plastics™, "Lexan™ sheet Technical Manual", *SABIC Innovative Plastics IP BV*, **2009**. https://web.archive.org/web/20150316235516/http://sfs.sabic.eu/wp-content/uploads/resource_pdf/1345453948-48623687-Technical-Manual-Coated-Uncoated-Sheet.pdf

[29] Special Metals Corporation, “INCONEL® alloy 690”, *Special Metals Corporation*, SMC-079, **2009.** https://www.specialmetals.com/assets/smc/documents/alloys/inconel/inconel-alloy-690.pdf

[30] Kanthal®, “Kanthal® A-1 Datasheet”, *Sandvik Group,* **2018**. https://www.kanthal.com/en/products/material-datasheets/strip/kanthal-a-1/

[31] Yamanaka, Shinsuke et al., “Thermal Properties of zirconium hydride”, *Journal of Nuclear Materials*, Vol. 294, pp. 94-98, **2001**. https://doi.org/10.1016/S0022-3115(01)00457-3

[32] DiCarlo, James A., “Advances in SiC/SiC Composites for Aero-Propulsion”, *NASA Technical Reports Server*, NASA/TM-2013-217889, **2013**. https://ntrs.nasa.gov/search.jsp?R=20140000988

[33] Zinkle, S. J. et al., “Thermophysical and mechanical properties of SiC/SiC composites” *Fusion Materials Semiannual Progress Report*, DOE/ER-0313/24, **1998**. https://doi.org/10.2172/330618

[34] Munro, Ronald G., “Evaluated Material Properties for a sintered α-Alumina”, *Journal of the American Ceramic Society*, Vol. 80, pp.1919-1928, **1997**. https://doi.org/10.1111/j.1151-2916.1997.tb03074.x

[35] WHS Sondermetalle, “Molybdenum (Mo, TZM, ML) Data Sheet”, *WHS Sondermetalle GmbH & Co. KG*, **2020**. https://www.whs-sondermetalle.de/en/materials/refractory-metals/mo-molybdenum.html

[36] Taylor, R. E. & Finch, R. A., "The specific heats and resistivities of molybdenum, tantalum, and rhenium", *Journal of the Less Common Metals*, Vol. 6, pp. 283-294, **1964**. https://doi.org/10.1016/0022-5088(64)90124-9

[37] Kreith, Frank et al., "Principles of Heat Transfer", *Cengage Learning*, Stamford, CT, 7th ed., **2011**.

[38] Lemmon, Eric W. et al., "Thermophysical Properties of Fluid Systems", *NIST Chemistry WebBook*, Standard Reference Database 69, **2020** (accessed). https://doi.org/10.18434/T4D303

[39] Jones, W. P. & Launder, B. E. "The calculation of low-Reynolds-number phenomena with a two-equation model of turbulence", *International Journal of Heat and Mass Transfer*, Vol. 6, pp. 1119-1130, **1973**. https://doi.org/10.1016/0017-9310(73)90125-7

[40] Patel, V. C. & Head, M. R., "Some observations on skin friction and velocity profiles in fully developed pipe and channel flows", *Journal of Fluid Mechanics*, Vol. 38, pp. 181-201, **1969**. https://doi.org/10.1017/S0022112069000115

[41] Jiang, Pei-Xue et al., "Convection heat transfer of CO_2 at supercritical pressures in a vertical mini tube at relatively low Reynolds numbers", *Experimental Thermal and Fluid Science*, Vol. 32, pp.1628-1637, **2008**. https://doi.org/10.1016/j.expthermflusci.2008.05.006

APPENDIX: Flow Characteristics of 40 mm ID, 50 mm OD loop

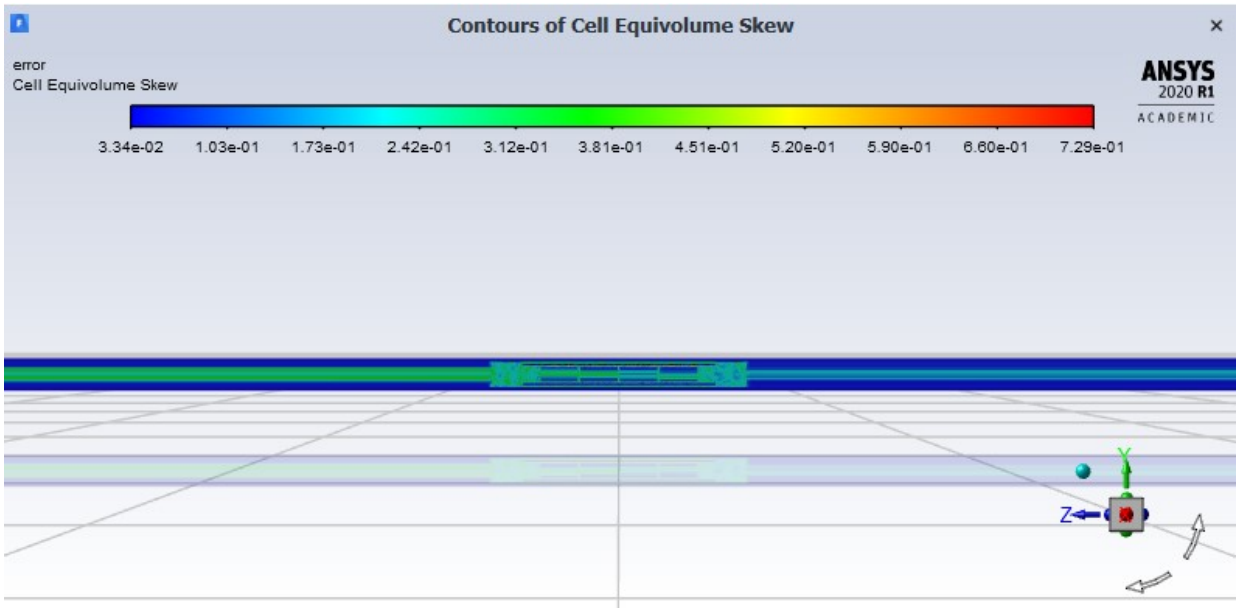

Figure A.1: Cell Equivolume Skew, linear test loop

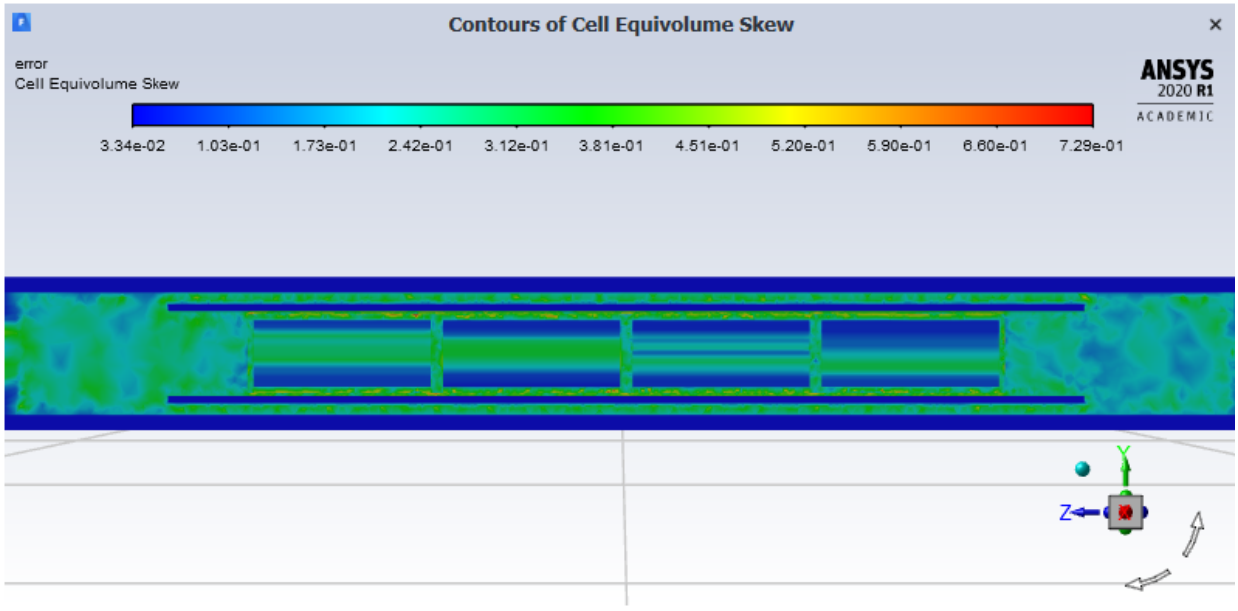

Figure A.2: Cell Equivolume Skew, linear test loop test section

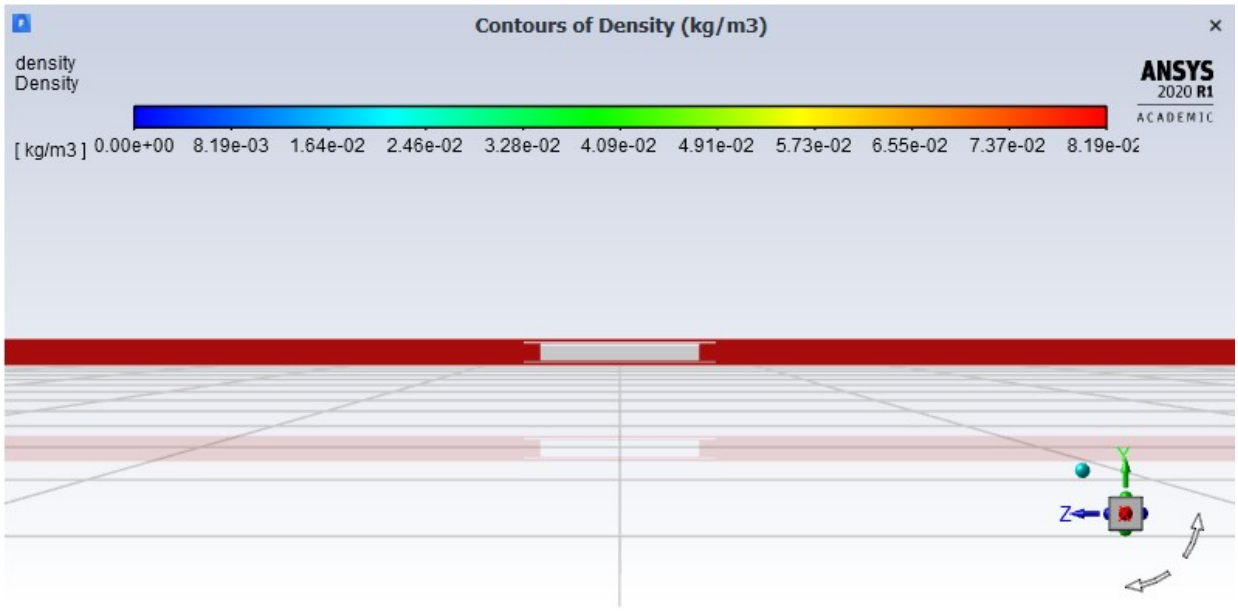

Figure A.3: Density, linear test loop

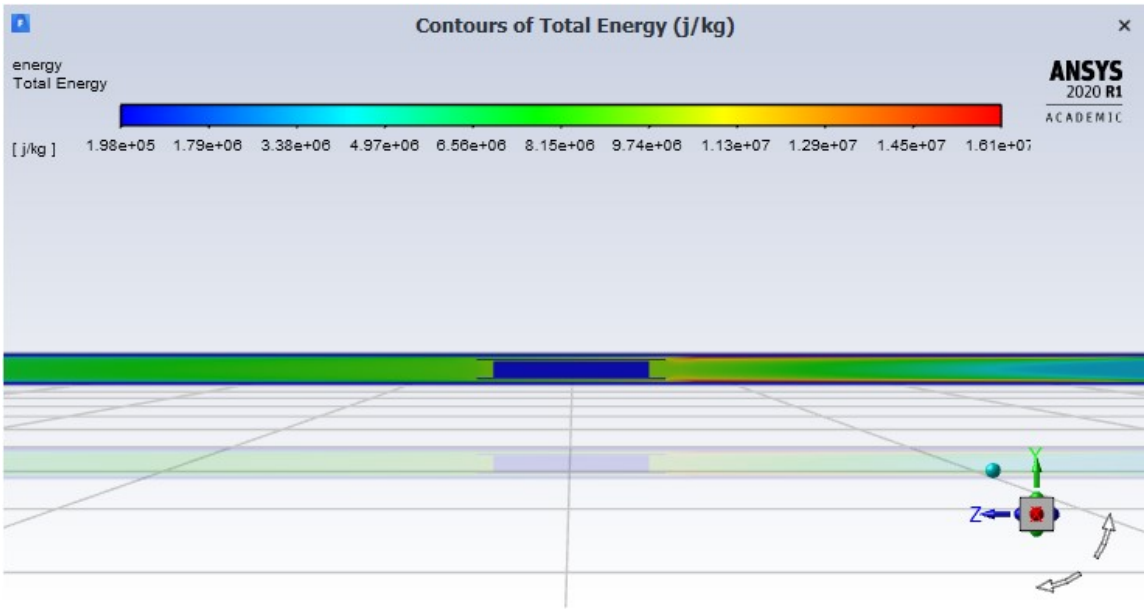

Figure A.4: Total Energy, linear test loop

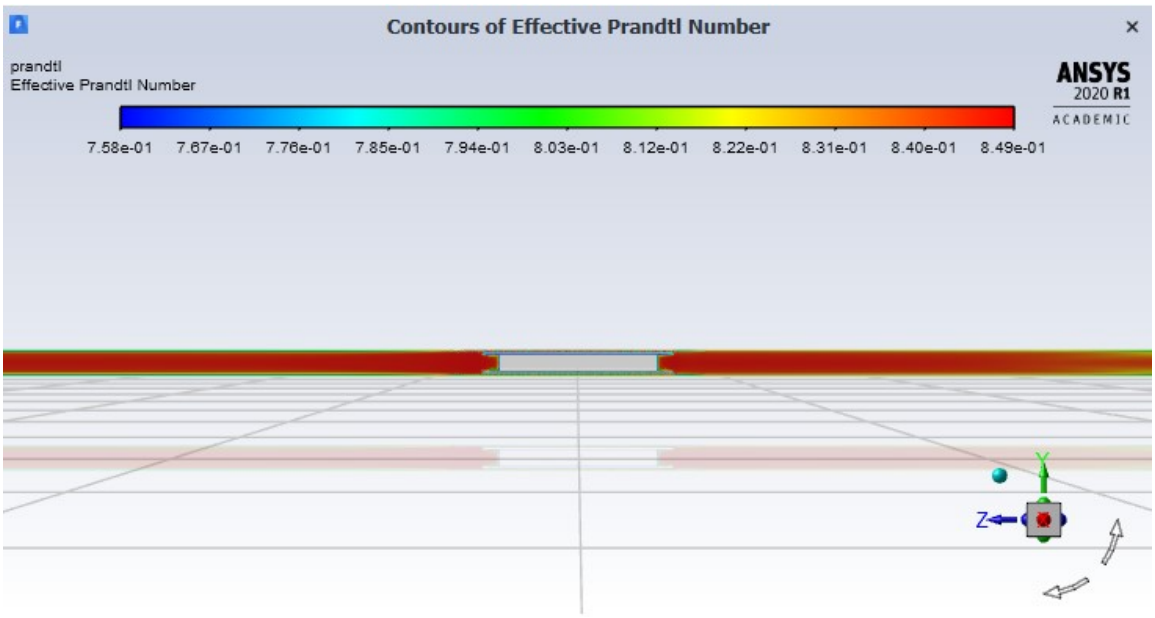

Figure A.5: Effective Prandtl Number, linear test loop

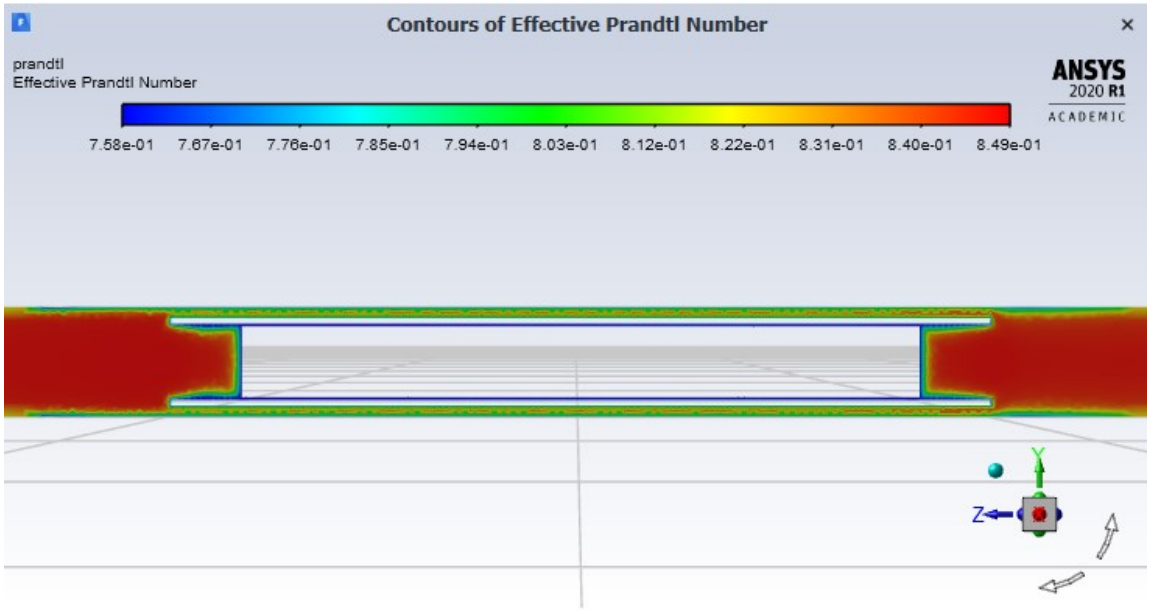

Figure A.6: Effective Prandtl Number, linear test loop test section

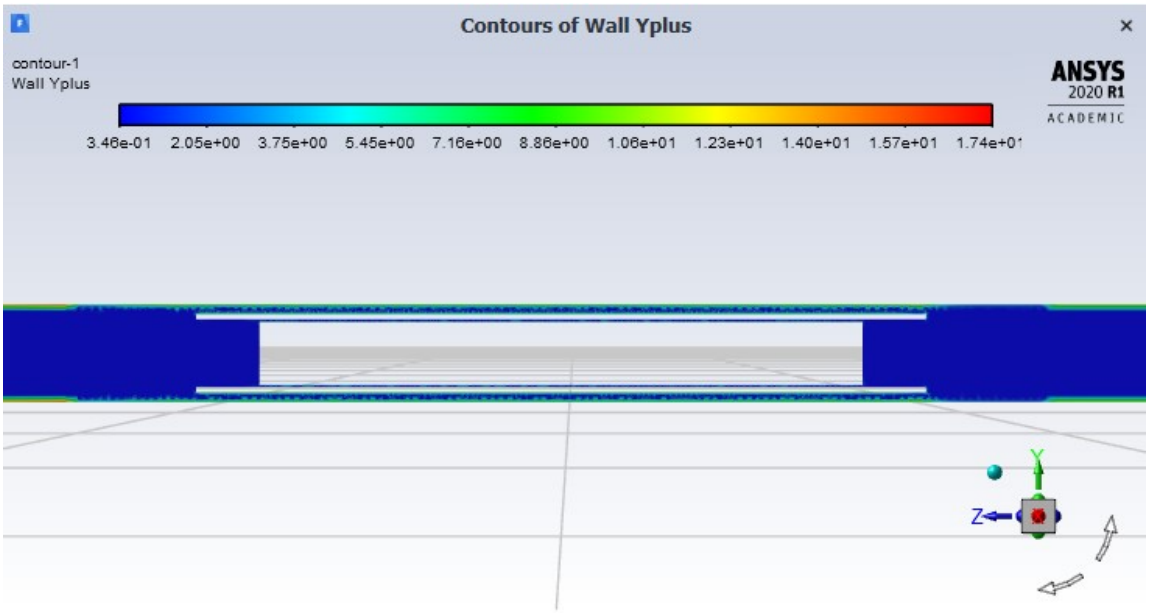

Figure A.7: Wall Y_plus, linear test loop test section

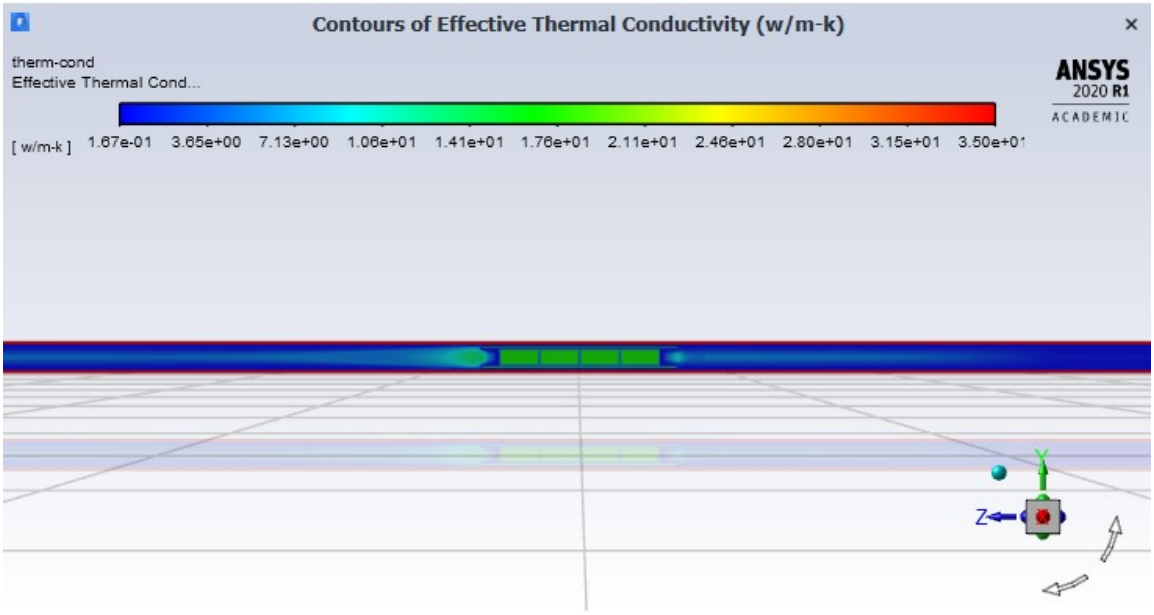

Figure A.8: Effective Thermal Conductivity, linear test loop

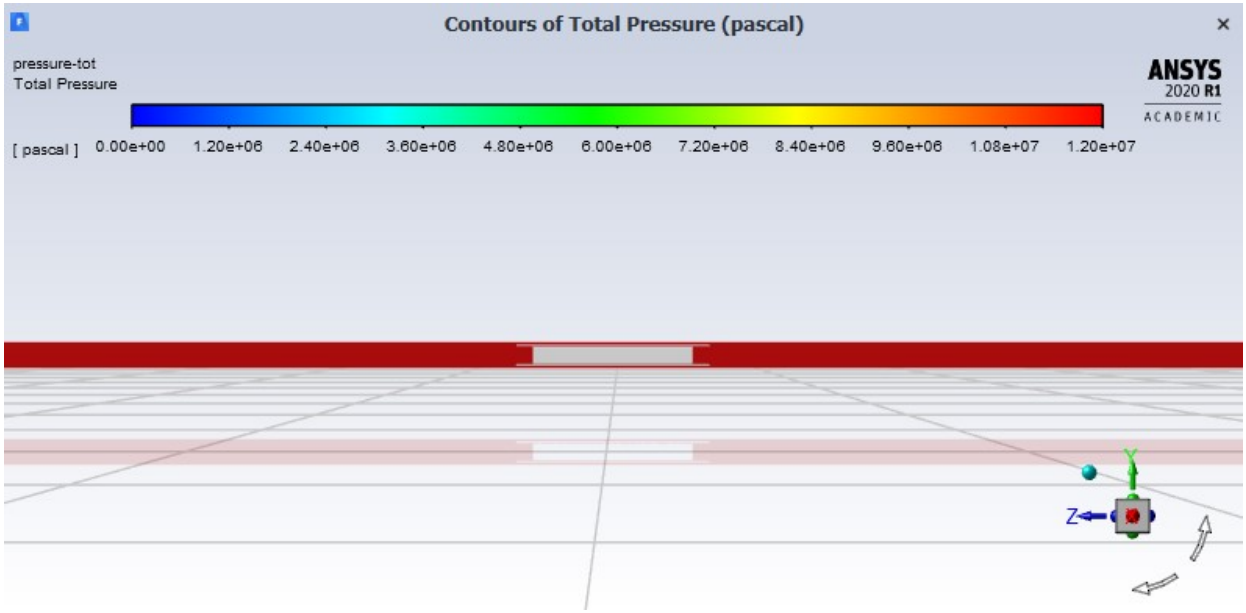

Figure A.9: Total Pressure, linear test loop

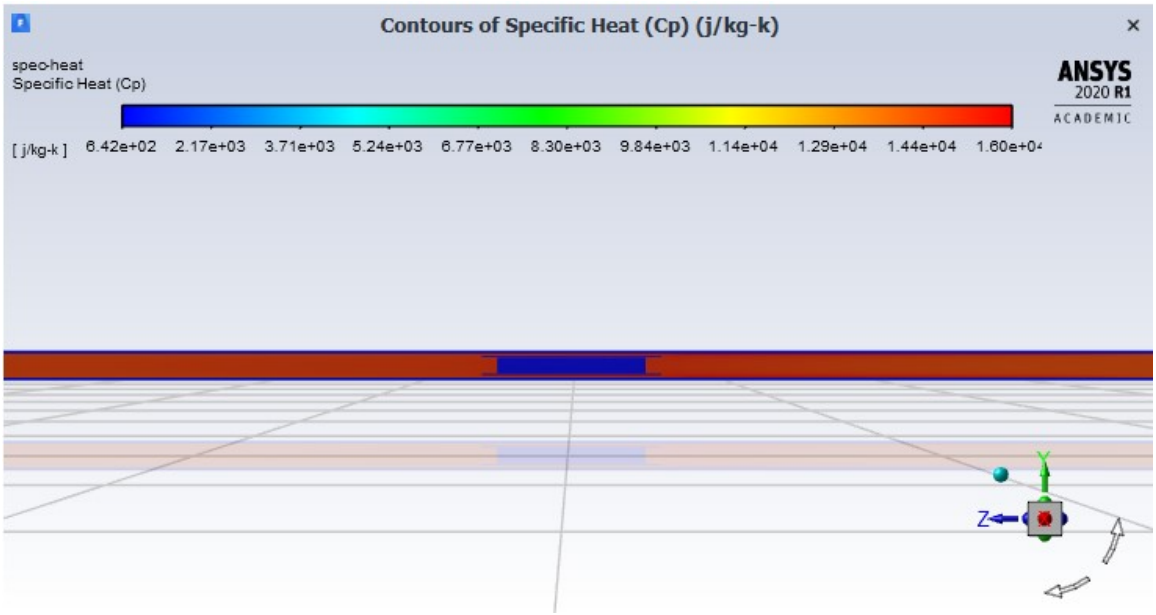

Figure A.10: Specific Heat, linear test loop

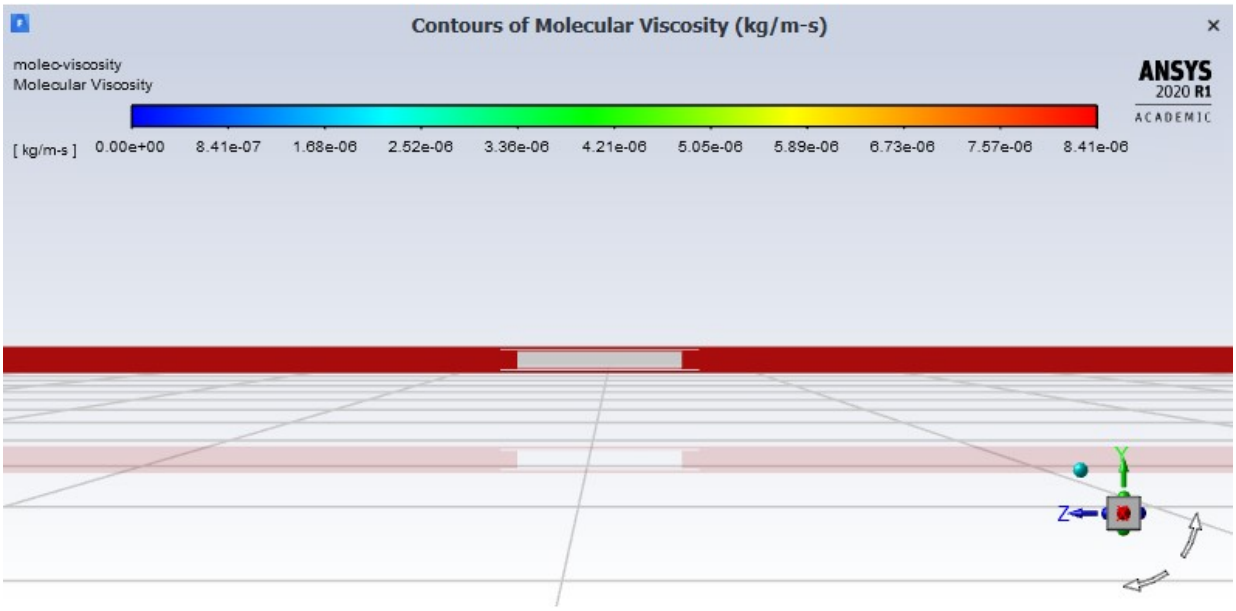

Figure A.11: Molecular Viscosity, linear test loop

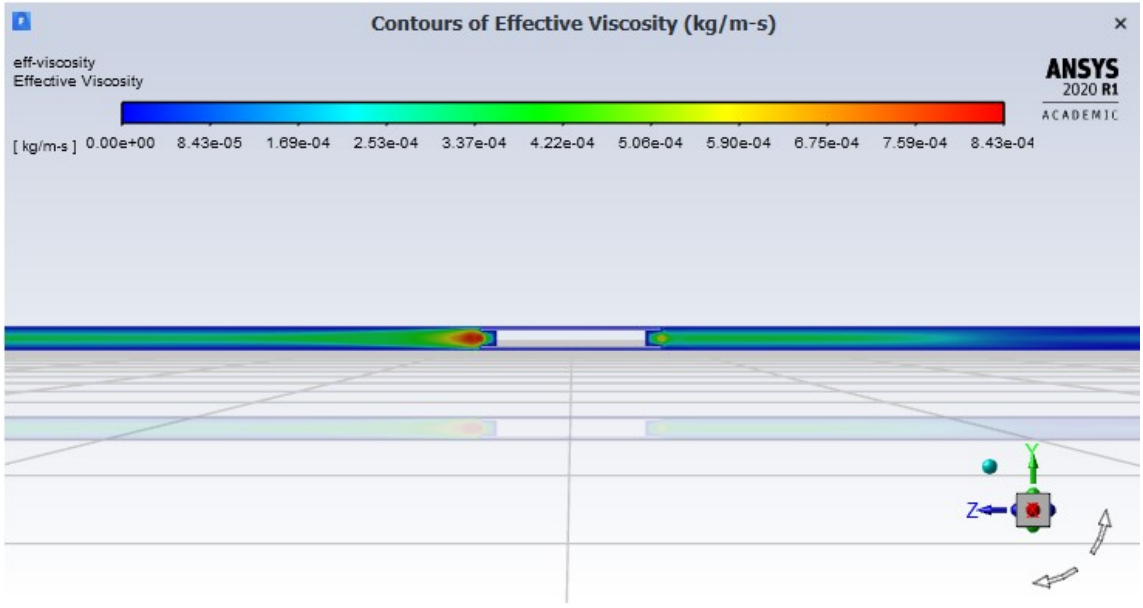

Figure A.12: Effective Viscosity, linear test loop

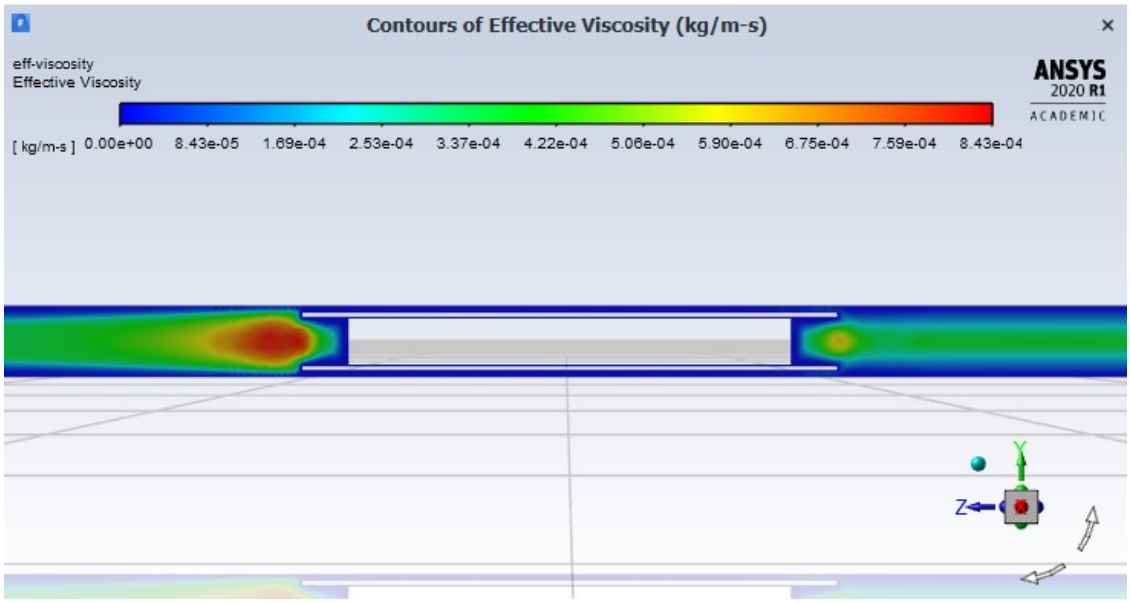

Figure A.13: Effective Viscosity, linear test loop test section